Chapter 1
Classical Device Modeling

Thomas Windbacher, Viktor Sverdlov, and Siegfried Selberherr

Abstract In this chapter an overview of classical device modeling will be given. The first section is dedicated to the derivation of the Drift–Diffusion Transport model guided by physical reasoning. How to incorporate Fourier's law to add a dependence on temperature gradients into the description, is presented. Quantum mechanical effects relevant for small devices are approximately covered by quantum correction models. After a discussion of the Boltzmann Transport equation and the systematic derivation of the Drift–Diffusion Transport model, the Hydrodynamic Transport model, the Energy Transport model, and the Six-Moments Transport model via a moments based method out of the Boltzmann Transport Equation, which is the essential topic of classical transport modeling, are highlighted. The parameters required for the different transport models are addressed by an own section in conjunction with a comparison between the Six-Moments Transport model and the more rigorous Spherical Harmonics Expansion model, benchmarking the accuracy of the moments based approach. Some applications of classical transport models are presented, namely, analyses of solar cells, biologically sensitive field-effect transistors, and thermovoltaic elements. Each example is addressed with an introduction to the application and a description of its peculiarities.

Keywords Classical device modeling · Drift–Diffusion · Six moments · Hydrodynamic transport · Energy transport · Solar cells · BioFET · Biologically sensitive field-effect transistor · Boltzmann transport · Thermoelectric · Figure of merit · Electrothermal transport · Spherical harmonics expansion

1 Heuristic Derivation of the Drift–Diffusion Transport Model

Even though the method of moments, which will be presented in Sect. 5, is quite sophisticated and offers the possibility to extend a transport model to an arbitrary large and accurate set of equations, physically understanding of the model is not

T. Windbacher (✉)
Institute for Microelectronics, Gußhausstraße 27–29/E360, 1040 Vienna, Austria
e-mail: Windbacher@iue.tuwien.ac.at

D. Vasileska and S.M. Goodnick (eds.), *Nano-Electronic Devices: Semiclassical and Quantum Transport Modeling*, DOI 10.1007/978-1-4419-8840-9_1,
© Springer Science+Business Media, LLC 2011

as instructive as a derivation via a heuristic approach. Therefore, in this section a derivation of the Drift–Diffusion Transport model with the aid of physical reasoning will be given.

One of the most general ways to treat electromagnetic phenomena is via the Maxwell equations. So we will start with a few simplifying assumptions and reduce the required equation set to the absolute minimum necessary to describe microelectronic devices. Then we will introduce a few additional equations covering the physical behavior of semiconducting materials.

1.1 Poisson Equation

The first simplifying assumption is the quasi-static approximation. This assumption restricts one to devices exhibiting a characteristic length which is noticeably smaller than the shortest electromagnetic wavelength existent in the considered system. For instance, assuming an upper limit of 100 GHz for the frequency of the electromagnetic field yields a wavelength of $\lambda = \mathrm{c}/f = 877\,\mu\mathrm{m}$. Thus characteristic device dimensions in the micrometer regime and below are quite reasonable. Due to the quasi-static approximation the displacement current $\partial_t \mathbf{D}$ and the induction $\partial_t \mathbf{B}$ can be neglected. This leads to a decoupling of the former coupled system of partial differential equations for the electric field and the magnetic field. The only remaining connection between the electric field $\mathbf{E}$ and the magnetic field $\mathbf{H}$ is given by the relation between the electric field $\mathbf{E}$ and the current density $\mathbf{j}$ which raises a magnetic field $\mathbf{H}$. In order to further simplify the equation system the magnetic part is completely neglected. Due to the now vanishing right hand side of $\mathrm{curl}\,\mathbf{E} = -\partial_t \mathbf{B}$ it is possible to define a scalar potential $\mathbf{E} = -\nabla \varphi$. The relation between the electric displacement field and the electric field is assumed to be linear and anisotropic for an inhomogeneous material $\mathbf{D} = \varepsilon \mathbf{E}$ dependent on the spatial coordinates. Embracing all assumptions with Gauß's law yields:

$$\nabla \cdot (\varepsilon \nabla \varphi) = -\rho. \tag{1.1}$$

The space charge density ρ has to reflect the charge contributions in the semiconductor. This is accomplished by three components: the electron concentration n, the hole concentration p and the concentration of fixed ionized charges C:

$$\rho = q\,(p - n + C). \tag{1.2}$$

Assembling all derived terms and further restricting to a scalar and spatial independent permittivity we obtain the well known Poisson equation:

$$\varepsilon \Delta \varphi = q\,(n - p - C). \tag{1.3}$$

1.2 Continuity Equation

The second ingredient for the Drift–Diffusion Transport model is derived from the continuity equation which takes care of mass conservation:

$$q\frac{\partial \rho}{\partial t} + \nabla \cdot \mathbf{j} = 0. \tag{1.4}$$

Like before we decompose the contributions of the current $\mathbf{j} = \mathbf{j}_n + \mathbf{j}_p$ and the space charge density $\partial\rho/\partial t = q\partial/\partial t\,(p-n)$ (assuming all immobile charges as fixed $\partial C/\partial t = 0$) into an electron and a hole related part:

$$\nabla \cdot (\mathbf{j}_n + \mathbf{j}_p) + q\frac{\partial}{\partial t}(p-n) = 0. \tag{1.5}$$

This steps enables to separate the electron and hole related contributions into two independent equations:

$$\nabla \cdot \mathbf{j}_n - q\frac{\partial}{\partial t}n = \ \ qR, \tag{1.6}$$

$$\nabla \cdot \mathbf{j}_p + q\frac{\partial}{\partial t}p = -qR. \tag{1.7}$$

The new term on the right hand side of (1.6) and (1.7) denotes the so-called net generation-recombination rate R. Since electrons and holes can not just vanish or appear, every additional electron generates an additional hole and vice versa. Due to their opposing charges the quantity R enters with opposite signs into the equations for electrons and holes. The net generation-recombination rate is usually modeled by the net generation rate of electron–hole pairs minus the net recombination rate of electron–hole pairs. In equilibrium R is equal zero but also out of equilibrium R is often neglected.

1.3 Charge Transport: Drift–Diffusion Assumption

Summarizing our equations, we have the Poisson equation and two continuity equations involve five unknown quantities (φ, n, p, $\mathbf{j}_n$ and $\mathbf{j}_p$). Therefore, we need two more conditions to make the equation system complete. These material equations can be deduced by examination of the forces acting upon the charged carriers (n, p) on a microscopic level. The simplest model at hand is based on the so-called Drift–Diffusion assumption. The model distincts between two charge carrier transport mechanisms: the *drift* of charge carriers due to an external electric field caused by a gradient in the electric potential and the *diffusion* of the charge carriers due to a spatial gradient in the charge carrier concentration.

The drift contribution is caused by the force of an externally applied electric field $\mathbf{E}$ on the charge carriers. Since the movement of charge carriers due to the electric field $\mathbf{E}$ constitutes an electric current, the drift current density is related to the applied electric field by the charge carrier concentration times mobility times electric field strength:

$$\mathbf{j}_n^{\text{Drift}} = qn\mu_n\mathbf{E} \quad \text{and} \tag{1.8}$$

$$\mathbf{j}_p^{\text{Drift}} = qp\mu_p\mathbf{E}. \tag{1.9}$$

The carrier mobility $\mu_{n,p}$ is a material dependent parameter and relates the electric field $\mathbf{E}$ to the drift current density $\mathbf{j}_{n,p}^{\text{Drift}}$. Equations (1.8) and (1.9) are related to Ohm's law by the conductivities $\sigma_n = qn\mu_n$ for electrons and $\sigma_p = qp\mu_p$ for holes:

$$\mathbf{j}_n^{\text{Drift}} = \sigma_n\mathbf{E} \quad \text{and} \quad \mathbf{j}_p^{\text{Drift}} = \sigma_p\mathbf{E}. \tag{1.10}$$

The second transport phenomenon is given by the particle flux density $\mathbf{F}$ and due to the gradient of the particle concentration. The proportionality factor is called diffusion coefficient $D_{n,p}$ and, further distinguishing between electron and hole diffusion, one obtains:

$$\mathbf{F}_n = -D_n\nabla n, \quad \mathbf{F}_p = -D_p\nabla p. \tag{1.11}$$

The diffusion related current densities are defined by their flux density multiplied with the individual charge of the charge carrier:

$$\mathbf{j}_n^{\text{Diffusion}} = -q\mathbf{F}_n = qD_n\nabla n, \quad \mathbf{j}_p^{\text{Diffusion}} = q\mathbf{F}_p = -qD_p\nabla p. \tag{1.12}$$

Close to the equilibrium the diffusion coefficient can be related to the carrier mobility via the Einstein relation:

$$D_{n,p} = \frac{k_\text{B}T}{q}\mu_{n,p} = V_\text{T}\,\mu_{n,p}. \tag{1.13}$$

k_B denotes the Boltzmann constant and T the temperature in K. The quantity V_T denotes the thermal voltage and is around $\approx 26\,\text{mV}$ at room temperature. The Einstein relation is only approximately valid for the non-equilibrium case and often used as a good starting guess for a numerical iterative solving algorithm.

Once more assembling all derived expressions yields a set of equations which is identical to the Drift–Diffusion Transport model derived by the method of moments:

$$\varepsilon\Delta\varphi = q(n - p - C), \tag{1.14}$$

$$qR = \nabla\cdot\mathbf{j}_n - q\frac{\partial n}{\partial t}, \tag{1.15}$$

$$-qR = \nabla\cdot\mathbf{j}_p + q\frac{\partial p}{\partial t}, \tag{1.16}$$

$$\mathbf{j}_n = -q\mu_n (n\nabla\varphi - V_\mathrm{T}\nabla n), \tag{1.17}$$

$$\mathbf{j}_p = -q\mu_p (p\nabla\varphi + V_\mathrm{T}\nabla p). \tag{1.18}$$

Even though the set of equations is now complete, it can not be solved without further description of the material parameters for the mobilities $\mu_{n,p}$ and the generation-recombination rate R. This will be taken care of in Sect. 7.

1.4 Quasi-Fermi Levels

The thermal equilibrium does not demand a position independent potential. For instance:

$$\mathscr{E}_c = \mathscr{E}_{c,0}(\mathbf{r}) - q\,\varphi(\mathbf{r}), \tag{1.19}$$

$$\mathscr{E}_v = \mathscr{E}_{v,0}(\mathbf{r}) - q\,\varphi(\mathbf{r}), \tag{1.20}$$

$$\mathscr{E}_i = \mathscr{E}_{i,0}(\mathbf{r}) - q\,\varphi(\mathbf{r}), \tag{1.21}$$

denoting the conduction band edge $\mathscr{E}_c$, the valence band edge $\mathscr{E}_v$ and the intrinsic Fermi level $\mathscr{E}_i$, respectively.

Treating the situation away from thermal equilibrium complicates the matter. Taking (1.17) and reformulating it:

$$\begin{aligned}
\mathbf{j}_n &= q\mu_n V_\mathrm{T}\nabla n - q\mu_n n\nabla\varphi \\
&= q\mu_n n\left(V_\mathrm{T}\frac{1}{n}\nabla n - \nabla\varphi\right) \\
&= q\mu_n n\left(V_\mathrm{T}\frac{n_i}{n}\nabla\frac{n}{n_i} - \nabla\varphi\right) \\
&= q\mu_n n\left(V_\mathrm{T}\nabla\ln\left(\frac{n}{n_i}\right) - \nabla\varphi\right) \\
&= q\mu_n n\nabla\underbrace{\left(V_\mathrm{T}\ln\left(\frac{n}{n_i}\right) - \varphi\right)}_{=-\phi_n},
\end{aligned}$$

with n_i as intrinsic concentration, shows that the drift and the diffusive contribution can be merged into one quantity. This quantity can be related to the quasi-Fermi level as follows [184]:

$$-q\,\phi_n = \mathscr{E}_{Fn} - \mathscr{E}_{i,0}. \tag{1.22}$$

Therefore, in the most general case, the current depends on the gradient of the quasi-Fermi levels and not solely on the gradient of the potential[1]:

$$\mathbf{j}_n = n\mu_n \nabla \mathscr{E}_{Fn}, \tag{1.23}$$

$$\mathbf{j}_p = p\mu_p \nabla \mathscr{E}_{Fp}. \tag{1.24}$$

The quasi-Fermi levels $\mathscr{E}_{Fn}$ and $\mathscr{E}_{Fp}$ introduced in (1.22)–(1.24) can be gained from (1.17) and (1.22) for electrons and in an analog way from (1.18) for holes, under the assumption that the solution of the equation system (1.14)–(1.18) is available:

$$\mathscr{E}_{Fn} = \mathscr{E}_{i,0} - q\varphi + qV_{\mathrm{T}} \ln\left(\frac{n}{n_i}\right), \tag{1.25}$$

$$\mathscr{E}_{Fp} = \mathscr{E}_{i,0} - q\varphi - qV_{\mathrm{T}} \ln\left(\frac{p}{n_i}\right). \tag{1.26}$$

2 Heuristic Inclusion of Heat Transport in the Drift–Diffusion Transport Model

The Drift–Diffusion Transport model assumes equality between the lattice temperature T_{L} and the charge carriers' temperature T_{n}. Furthermore, it states negligible temperature gradients in the device. However, there is an intrinsic temperature dependence in basically all microscopic phenomena in solids, which is mirrored in the basic semiconductor equations directly by the thermal voltage V_{T} and indirectly via the temperature dependence of the mobilities μ_n and μ_p and the recombination rate R. Generalizing the Drift–Diffusion Transport model by introducing a local temperature, in order to cover a more detailed view of temperature dependent phenomena, one has to employ an extra equation. Heat energy is also a conserved quantity, where the heat flux is governed by an expression similar to the continuity equation for charge:

$$\rho\, c\, \frac{\partial T_{\mathrm{L}}}{\partial t} - \nabla \cdot (\kappa \nabla T_{\mathrm{L}}) = H. \tag{1.27}$$

ρ denotes the mass density of the material and c describes the specific heat of the material, while κ expresses the thermal conductivity. Due to the phonon dominated heat transport in semiconductors the lattice temperature T_{L} is the quantity of interest. The first term on the left hand side of (1.27) characterizes the initial transient time dependent behavior of changes due to the heat sources H, while the second term takes care of the stationary temperature distribution. The heat generation term H

[1] The intrinsic energy $\mathscr{E}_{i,0}$ is globally constant.

establishes the link between the heat-flow and the current and can be approximated by a first-order Joule-term $\mathbf{j} \cdot \mathbf{E}$ and an expression for the carrier recombination. Every generation or recombination of an electron–hole pair withdraws or releases an energy amount of at least the band gap energy $\mathscr{E}_g$ from the crystal lattice. Therefore, the heat source term can be formulated as [3]:

$$H = \nabla \cdot \left(\frac{\mathscr{E}_c}{q} \mathbf{j}_n + \frac{\mathscr{E}_v}{q} \mathbf{j}_p \right), \tag{1.28}$$

with $\mathscr{E}_c$ and $\mathscr{E}_v$ denoting the conduction and valence band edge energy, respectively. Considering non-degenerate materials only [184], one can further simplify (1.28) to:

$$H = (\mathbf{j}_n + \mathbf{j}_p) \cdot \mathbf{E} + R \mathscr{E}_g. \tag{1.29}$$

Accompanying with spatial gradients in the local temperature a new driving force occurs. This additional driving force causes an extra current flow, which has to be incorporated by supplementary terms in the current density relations in (1.17) and (1.18):

$$\mathbf{j}_{n,\mathrm{th}} = q D_{n,\mathrm{th}} \nabla T_\mathrm{L} \quad \text{and} \quad \mathbf{j}_{p,\mathrm{th}} = -q D_{p,\mathrm{th}} \nabla T_\mathrm{L}, \tag{1.30}$$

with thermal diffusion coefficients $D_{n,\mathrm{th}}$ and $D_{p,\mathrm{th}}$ approximately related to the diffusion coefficients D_n and D_p by [209]:

$$D_{n,p.\mathrm{th}} \backsimeq \frac{D_{n,p}}{2T}. \tag{1.31}$$

These current density contributions are essential for the description of thermoelectric effects, like the Seebeck effect or the Peltier effect.

During the derivation of the model above it was demonstrated that one can deduce a higher order transport model via physically sound reasoning and not only by the mathematically sophisticated method of moments. Van Roosbroeck [173] was the first to present a model pretty close to the description given here already in 1950.

One has to note that for higher order transport models the description of the heat source term H becomes much more challenging (see Sect. 2.4 in [124]).

3 Incorporating Quantum Mechanical Effects via Quantum Correction Models

The density of states (DOS) of a system is given by the number of states at each energy level, which are available for occupation (q.v. [14, 122]). Since quantum mechanical effects affects the DOS by causing a two-dimensional electron gas, the carrier concentration near the gate oxide decreases. This influences several device characteristics like the current–voltage or the capacitance–voltage characteristics and therefore has to be taken into account either by a rigorous self-consistent solution of the Schrödinger equation and the Poisson equation, which is computationally expensive, or via a supplemental quantum correction model in classical

device simulations. Various quantum correction models stemming from different approaches have been proposed [47, 82, 112, 117, 148, 156, 225], some of them are based on empirical fits via many parameters [112, 148], some models exhibit a degraded convergence depending on the electric field [47] or demand a recalibration for each particular device [82].

The modified local density approximation (MLDA) by Paasch [156] proposes a local correction of the effective DOS N_c near the gate oxide defined by:

$$N_c = N_{c,0}\left(1 - \exp\left[-\frac{(z+z_0)^2}{\chi^2\,\lambda_{\text{thermal}}^2}\right]\right) \quad \text{with} \quad \lambda_{\text{thermal}} = \frac{\hbar}{\sqrt{2mk_{\text{B}}T}}. \tag{1.32}$$

$N_{c,0}$ denotes the classical effective DOS modified by the fitting parameter χ. z describes the distance from the interface, z_0 is the tunneling distance, and λ_{thermal} constitutes the thermal wavelength. Equation (1.32) can be gained from the quantum mechanical expression governing the particle density [82]. The benefit of the MLDA procedure lies in the fact that no solution variable is needed in the correction term. Hence, this model can be employed as a preprocessing step with only minimal significance for the overall CPU time required for the solution of the entire set of the transport equations [225]. On the other hand, the drawback of the MLDA is its founding on the field-free Schrödinger equation and in conjunction the loss of validity for high fields.

An improved MLDA (IMLDA) technique has been suggested by [112, 148], introducing a heuristic wavelength parameter:

$$\lambda'_{\text{thermal}}(z, N_{\text{eff}}, T) = \chi(z, N_{\text{eff}}, T)\,\lambda_{\text{thermal}}(T), \tag{1.33}$$

where N_{eff} denotes the net doping with $\chi(z, N_{\text{eff}}, T)$ as a fit factor. Due to this adaption, the IMLDA is able to cover the important case of high-fields perpendicular to the interface [112]. The fit parameters have been extracted from results gained by a self-consistent Schrödinger Poisson solver and are calibrated for bulk MOSFET structures. However, the MLDA method is only valid for devices with one gate oxide and thus a description of double-gate SOI MOSFETs (DG SOI MOSFETs) is not possible.

A quantum correction technique capable of treating DG SOI MOSFETs is shown in [117]. The basic concept of this approach is that due to the strong quantization perpendicular to the interface, the potential in the SOI is well approximated by an infinite square well potential. The eigenstates in the quantization region can be calculated with an analytic approach and related to a quantum correction potential which adjusts the band edge in such a way that the quantum mechanical carrier concentration is reproduced.

Van Dorts approach [47] improves the modeling of the conduction band edge:

$$\mathscr{E}_c = \mathscr{E}_{\text{class}} + \frac{13}{9}\mathrm{F}(z)\,\Delta\mathscr{E}_{\text{g}} \quad \text{with} \quad \Delta\mathscr{E}_{\text{g}} \approx \beta\left(\frac{\kappa_{\text{Si}}}{4qk_{\text{B}}T}\right)^{1/3}|\mathbf{E}_\perp|^{2/3}. \tag{1.34}$$

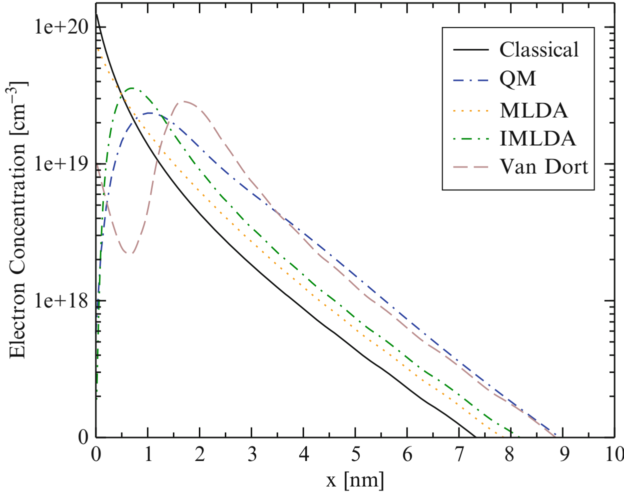

Fig. 1.1 Electron concentration of a single-gate SOI MOSFET for different modeling approaches. Illustrating the classically, quantum-mechanically, in conjunction with the quantum correction models MLDA, IMLDA, and Van Dort calculated electron concentration as a function of the distance to the interface [220]

$\mathscr{E}_{\text{class}}$ denotes the classical band energy and the correction function F depends on the distance z to the interface, while $\mathbf{E}_{\perp}$ stands for the electric field perpendicular to the interface. The proportionality factor β is gained from the shift of the long-channel threshold voltage as explained in [47].

Figure 1.1 compares the different quantum correction models against the classical model and the quantum mechanical model [116] for a single-gate SOI MOSFET. It shows the electron concentration as a function of the distance to the interface for the classical, the exact quantum mechanical, the quantum correction model MLDA, the IMLDA [112], and the model after Van Dort [47] for a gate voltage of 1 V. As can be seen the IMLDA model reproduces quite well the quantum mechanical concentration and hence is sufficient to cover quantum mechanical effects in classical device simulations [220].

4 Boltzmann Transport Equation

There are two fundamental equations for semi-classical device simulation, the Poisson equation and the Boltzmann equation. While the Poisson equation takes care of the electrostatical description of the system, the Boltzmann equation describes the propagation of the distribution function in the device. The distribution function $f(\mathbf{r},\mathbf{k},t)$ is a function describing the number of particles contained in a unit volume in phase space and depends on three values for the position $\mathbf{r} = x\mathbf{x} + y\mathbf{y} + z\mathbf{z}$, three values of the wave vector $\mathbf{k} = k_x\mathbf{k}_x + k_y\mathbf{k}_y + k_z\mathbf{k}_z$, and time t.

These two equations in conjunction have to be solved in a self-consistent manner and can be exploited as a reference for any higher-order models (see Sect. 5).

The Boltzmann Transport equation is gained from the Liouville theorem [110, 140], a fundamental principle of classical statistical mechanics. It states that the distribution function $f(\mathbf{r},\mathbf{k})$ is constant for all times t along phase-space trajectories Γ_i ((1.35), [151]):

$$f(\mathbf{r}+\mathrm{d}\mathbf{r},\mathbf{k}+\mathrm{d}\mathbf{k},t+\mathrm{d}t) = f(\mathbf{r},\mathbf{k},t), \tag{1.35}$$

which leads to the Boltzmann Transport equation without scattering, after taking the total derivative of (1.35):

$$\partial_t f(\mathbf{r},\mathbf{k},t) + \frac{\mathrm{d}\mathbf{r}}{\mathrm{d}t}\cdot\partial_{\mathbf{r}} f(\mathbf{r},\mathbf{k},t) + \frac{\mathrm{d}\mathbf{k}}{\mathrm{d}t}\cdot\partial_{\mathbf{k}} f(\mathbf{r},\mathbf{k},t) = 0. \tag{1.36}$$

Furthermore, we introduce the Hamiltonian equations:

$$\frac{\mathrm{d}\mathbf{r}}{\mathrm{d}t} = \nabla_{\mathbf{p}}\mathscr{H} \quad \text{and} \quad \frac{\mathrm{d}\mathbf{p}}{\mathrm{d}t} = -\nabla_{\mathbf{r}}\mathscr{H}, \tag{1.37}$$

with $\mathbf{p} = \hbar\mathbf{k}$ denoting the momentum, and $\mathbf{r}$ the position of a particle in phase-space, while $\mathscr{H}$ describes the Hamiltonian of the system, which will be incorporated later.

Inaugurating the scattering operator Q_{coll}, the balance equation for the distribution function must obey the conservation equation:

$$\frac{\mathrm{d}f(\mathbf{r},\mathbf{k},t)}{\mathrm{d}t} = Q_{\mathrm{coll}}\left(f(\mathbf{r},\mathbf{k},t)\right). \tag{1.38}$$

Hence, the scattering operator opens up the possibility for particles to jump from one phase-space trajectory to another. Joining the full derivative of the distribution function and (1.37), the commonly used expression for the Boltzmann Transport equation can be written as:

$$\partial_t f + \nabla_{\mathbf{p}}\mathscr{H}\nabla_{\mathbf{r}} f - \nabla_{\mathbf{r}}\mathscr{H}\nabla_{\mathbf{p}} f = Q_{\mathrm{coll}}\left(f\right). \tag{1.39}$$

Neglecting inter-band processes and by this the generation and recombination of free carriers in the semiconductor, the collision operator $Q_{\mathrm{coll}}(f)$ can be written as [138]:

$$Q_{\mathrm{eff}}(f) = \sum_{\mathbf{p}'} f(\mathbf{p}')\,(1-f(\mathbf{p}))\,S(\mathbf{p}',\mathbf{p}) - \sum_{\mathbf{p}'} f(\mathbf{p})\,\left(1-f(\mathbf{p}')\right)\,S(\mathbf{p},\mathbf{p}'). \tag{1.40}$$

The collision term accounts for in-scattering from $\mathbf{p}'$ to $\mathbf{p}$ as well as out-scattering from $\mathbf{p}$ to $\mathbf{p}'$. $f(\mathbf{p}')$ represents the probability for the state $\mathbf{p}'$ to be occupied and $1-f(\mathbf{p})$ the probability for the state $\mathbf{p}$ to be accessible for in-scattering. $S(\mathbf{p}',\mathbf{p})$ describes the transition rate from $\mathbf{p}'$ to $\mathbf{p}$. The sum governs all states accessible for scattering from and to $\mathbf{p}$. From a physical point of view, the collision term covers

the interaction of the carriers with the lattice (e.g. phonon scattering), the influence of ionized impurities, as well as additional scattering due to inhomogeneities in the grid in material alloys: it can be modeled as outlined in [106, 190].

Equation (1.40) represents a seven-dimensional integro-differential semi-classical equation. While the left hand side of the equation represents Newton mechanics, the right side denotes a quantum mechanical scattering operator. In order to develop solution strategies for this equation one has to understand the incorporated assumptions and limitations:

- The initial Liouville formulation stated a many particle problem. Introducing the Hartree–Fock approximation [137] allows to reduce the problem to a particle system with a proper potential. The contribution of the surrounding electrons is approximated by a charge density. Therefore, the short-range electron–electron interaction is excluded. Nevertheless, the potential of the surrounding carriers is treated self-consistently.
- The use of a distribution function $f(\mathbf{r},\mathbf{k},t)$ is a classical concept. Therefore, the Heisenberg uncertainty principle is not considered, and position and momentum are always treated at the same time.
- Because of Heisenberg's principle, the Boltzmann Transport equation is only valid, if the mean free path of particles is longer than the De Broglie wavelength.
- Particles abide Newton's law, due to the semi-classical treatment of particles.
- It is assumed that collisions between particles are binary and instantaneous in time and local in space. This approximation holds true for long free flight times compared to the collision times

During the derivation of the transport models from the Boltzmann Transport equation it is important to take these limitations and implications into account. However, models based on the Boltzmann Transport equation give good results in the scattering dominated regime [19, 97, 105, 159].

5 Derivation of Transport Models from the Boltzmann Transport Equation via a Moments Based Method

Solving the Boltzmann Transport equation yields excellent results [19, 97, 105, 159], but is much more demanding than other transport models (e.g. Drift–Diffusion Transport model or Energy Transport model) due to its high dimensionality. For instance, assuming a discrete mesh with 100 ticks in each spatial coordinate and time, will result in 10^{14} points. If we assert further 7×8 bytes (8 bytes for each coordinate), the memory consumption will be already 5.600 Terrabytes for just storing the points. Therefore, one is interested in numerically cheaper, but at the same time valid transport models, for the regime of interest.

From an engineering viewpoint, the method of moments is a very efficient way to derive transport models with a reduced complexity compared to the Boltzmann

Transport equation. By multiplying the Boltzmann Transport equation with a set of weight functions and integrating over **k**-space one can deduce a set of balance and flux equations coupled with the Poisson equation.

Via this formalism an arbitrary number of equations can be generated. Each equation contains information from the next higher moment, thus exhibiting more moments than equations. Therefore, one has to truncate the equation system at a certain point and complete the system by an additional condition. This condition, relating the highest moment with the lower moments, is called closure relation. The closure relation appraises the information of the higher moments and in conjunction with it determines the error introduced in the system. For example, the Drift–Diffusion Transport model can be gained by assuming thermal equilibrium between the charge carriers and the lattice ($T_n = T_\mathrm{L}$) [138]. There are various theoretical approaches to tackle the closure problem [133] for an arbitrary moment (e.g. maximum entropy principle [11, 12, 146]).

The basic concept of the maximum entropy principle is that a large set of collisions is needed to relax the carrier energies to their equilibrium, while at the same time momentum, heat flow, and anisotropic stress relax within shorter time. Hence, the charge carriers are in an intermediate state. This state can be noted as partial thermal equilibrium. Only the carrier temperature T_n is non-zero, while all other parameters vanish. Furthermore it is assumed that the entropy density and the entropy flux are independent on the relative electron gas velocity. The Hydrodynamic Transport model is obtained by assuming a heated Maxwellian distribution for closure, while the introduction of the kurtosis leads to the Six-Moments Transport model. A more detailed explanation will be given later.

In order to obtain physically reasonable equations, it is beneficial to choose weight functions as the power of increasing orders of momentum. The moments in one, two, and three dimensions can be defined as:

$$x_{\mathrm{j,d}}(\mathbf{r}_\mathrm{d}) = \frac{2}{(2\pi)^\mathrm{d}} \int_{-\infty}^{\infty} \mathbf{X}_{\mathrm{j,d}}(\mathbf{r}_\mathrm{d}, \mathbf{k}_\mathrm{d}) f_\mathrm{d}(\mathbf{r}_\mathrm{d}, \mathbf{k}_\mathrm{d}, t) \mathrm{d}^\mathrm{d} k = n \langle \mathbf{X}_{\mathrm{j,d}}(\mathbf{k}_\mathrm{d}) \rangle = \langle\langle \mathbf{X}_{\mathrm{j,d}}(\mathbf{k}_\mathrm{d}) \rangle\rangle . \tag{1.41}$$

$x_\mathrm{j}(\mathbf{r})$ are the macroscopic values with their microscopic counterpart $X_\mathrm{j}(\mathbf{k})$, and $f_\mathrm{d}(\mathbf{r}_d, \mathbf{k}_d, t)$ denotes the time dependent distribution function spanning over the six-dimensional phase space. The letter $\mathrm{d} = 1, 2, 3$ symbolizes the one-, two-, and three-dimensional system, respectively, while n describes the carrier concentration. The notations $\langle\ \rangle$ and $\langle\langle\ \rangle\rangle$ denote the normalized statistic average and the statistic average, respectively.

During the derivation of the macroscopic transport models, the dimension indices are skipped to ease readability. Multiplying the Boltzmann transport equation with the even scalar-valued weights $X = X(\mathbf{r}, \mathbf{k})$ and integrating over **k**-space:

$$\int X\, \partial_t f\, \mathrm{d}^3\mathbf{k} + \int X\, \mathbf{v} \nabla_\mathbf{r} f\, \mathrm{d}^3\mathbf{k} + \int X\, \mathbf{F} \nabla_\mathbf{p} f\, \mathrm{d}^3\mathbf{k} = \langle\langle \partial_t X \rangle\rangle_\mathrm{coll} , \tag{1.42}$$

results in the general conservation laws. Furthermore, in the following derivation, the distribution function $f(\mathbf{r},\mathbf{k},t)$, the group velocity $\mathbf{v}(\mathbf{r},\mathbf{k})$, and the generalized force $\mathbf{F}(\mathbf{r},\mathbf{k})$ are written as f, $\mathbf{v}$, and $\mathbf{F}$, respectively. The first term on the left side of (1.42) can be simplified to:

$$\int X\,\partial_t f\,\mathrm{d}^3\mathbf{k} \;=\; \partial_t \int X\,f\,\mathrm{d}^3\mathbf{k} \;=\; \partial_t \,\langle\!\langle X\rangle\!\rangle\,, \tag{1.43}$$

while the second term can be reformulated to:

$$\int X\,\mathbf{v}\nabla_{\mathbf{r}} f\,\mathrm{d}^3\mathbf{k} \;=\; \int \nabla_{\mathbf{r}}\,(X\,\mathbf{v}\,f)\,\mathrm{d}^3\mathbf{k} - \int X\,f\,\nabla_{\mathbf{r}}\,\mathbf{v}\,\mathrm{d}^3\mathbf{k} - \int \mathbf{v}\,f\,\nabla_{\mathbf{r}} X\,\mathrm{d}^3\mathbf{k}, \tag{1.44}$$

and the third term can be written as:

$$\int X\,\mathbf{F}\nabla_{\mathbf{p}} f\,\mathrm{d}^3\mathbf{k} \;=\; \int \nabla_{\mathbf{p}}\,(X\,\mathbf{F}\,f)\,\mathrm{d}^3\mathbf{k} - \int X\nabla_{\mathbf{p}}\mathbf{F}\,f\,\mathrm{d}^3\mathbf{k} - \int \mathbf{F}\,\nabla_{\mathbf{p}} X\,f\,\mathrm{d}^3\mathbf{k}, \tag{1.45}$$

Exploiting Gauß's law in conjunction with the assumption that all surface integrals over the first Brioullin-zone vanish [147], the first term on the right side of (1.45) becomes zero. Substituting $\mathbf{F} = -\nabla_{\mathbf{r}}\mathscr{H}$ and $\mathbf{v} = \nabla_{\mathbf{p}}\mathscr{H}$ in combination with the Hamiltonian function $\mathscr{H}$ defined as:

$$\mathscr{H} = \pm\mathscr{E}_{\mathrm{c,v}}(\mathbf{r}) + \mathrm{s}_\alpha\,q\,\varphi + \mathscr{E}(\mathbf{r},\mathbf{k}) \;=\; \mathscr{E}(\mathbf{r},\mathbf{k}) + \mathrm{s}_\alpha\,q\,\tilde{\varphi}, \tag{1.46}$$

with $\mathrm{s}_\alpha = \mp 1$ for electrons and holes, respectively, into (1.44) and (1.45) results into the Boltzmann Transport equation expressed via its averages of the even scalar-valued moment:

$$\partial_t \,\langle\!\langle X\rangle\!\rangle + \nabla_{\mathbf{r}}\,\langle\!\langle \mathbf{v}X\rangle\!\rangle - \langle\!\langle \mathbf{v}\,\nabla_{\mathbf{r}}X\rangle\!\rangle - \langle\!\langle \mathbf{F}\,\nabla_{\mathbf{p}}X\rangle\!\rangle \;=\; \langle\!\langle \partial_t X\rangle\!\rangle_{\mathrm{coll}}\,, \tag{1.47}$$

or, after some additional calculation steps:

$$\partial_t \,\langle\!\langle X\rangle\!\rangle + \nabla_{\mathbf{r}}\,\langle\!\langle \mathbf{v}X\rangle\!\rangle - \langle\!\langle \mathbf{v}\,\nabla_{\mathbf{r}}X\rangle\!\rangle + \langle\!\langle \nabla_{\mathbf{r}}\mathscr{E}\nabla_{\mathbf{p}}X\rangle\!\rangle + \mathrm{s}_\alpha q\,\langle\!\langle \nabla_{\mathbf{p}}X\rangle\!\rangle\,\nabla_{\mathbf{r}}\tilde{\varphi} = \langle\!\langle \partial_t X\rangle\!\rangle_{\mathrm{coll}}\,. \tag{1.48}$$

Analog to the derivation for the even scalar-valued moments, the odd vector-valued moment's equations can be deduced:

$$\begin{aligned}\partial_t \,\langle\!\langle \mathbf{X}\rangle\!\rangle + \nabla_{\mathbf{r}}\,\langle\!\langle \mathbf{v}\otimes\mathbf{X}\rangle\!\rangle - \langle\!\langle \mathbf{v}\,\nabla_{\mathbf{r}}\otimes\mathbf{X}\rangle\!\rangle + \langle\!\langle \nabla_{\mathbf{r}}\mathscr{E}\nabla_{\mathbf{p}}\otimes\mathbf{X}\rangle\!\rangle + \mathrm{s}_\alpha q\,\langle\!\langle \nabla_{\mathbf{p}}\otimes\mathbf{X}\rangle\!\rangle\,\nabla_{\mathbf{r}}\tilde{\varphi}\\ = \langle\!\langle \partial_t \mathbf{X}\rangle\!\rangle_{\mathrm{coll}}\,.\end{aligned} \tag{1.49}$$

From (1.48) and (1.49) the conservation equations and fluxes of the different macroscopic transport models will be derived in the sequel.

5.1 Modeling of the Scattering Operator

Several approaches to describe the scattering operator analytically have been proposed [31,208]. Here, the emphasis will be put on the relaxation time approximation of Bløtekjær [28]:

$$\langle\!\langle \partial_t X \rangle\!\rangle_{\text{coll}} = -\frac{\langle\!\langle X \rangle\!\rangle - \langle\!\langle X_0 \rangle\!\rangle}{\tau_X(f)}. \tag{1.50}$$

Here, $\tau_X(f)$ denotes the macroscopic relaxation time concerning the weight function X. $\langle\!\langle X_0 \rangle\!\rangle$ describes the average weight function in equilibrium. Due to the dependence of the relaxation time $\tau_X(f)$ on the distribution function, (1.50) is no approximation [67]. Setting:

$$\tau_X \neq \tau_X(f) \tag{1.51}$$

Equation (1.51) assumes a solely dependence of the relaxation time τ on the moments of the distribution function and is also known as the macroscopic relaxation time approximation. This way, the relaxation times depend only on the moments of the distribution function. Therefore, the odd moments can be formulated as:

$$\langle\!\langle \partial_t \mathbf{X} \rangle\!\rangle_{\text{coll}} \approx -\frac{\langle\!\langle \mathbf{X} \rangle\!\rangle - \langle\!\langle \mathbf{X}_0 \rangle\!\rangle}{\tau_{\text{odd}}} = -\frac{\mathbf{x}}{\tau_{\text{odd}}}, \tag{1.52}$$

and the even moments can be written as:

$$\langle\!\langle \partial_t X \rangle\!\rangle_{\text{coll}} \approx -\frac{\langle\!\langle X \rangle\!\rangle - \langle\!\langle X_0 \rangle\!\rangle}{\tau_{\text{even}}} = -\frac{x - x_0}{\tau_{\text{even}}}. \tag{1.53}$$

The subscript *even* and *odd* is connected to the corresponding even and odd moments.

5.2 Macroscopic Transport Models

From (1.48) and (1.49) the hierarchy of macroscopic transport models can be deduced by means of the moments based method described before [76]. The first three even scalar valued moments are given by powers of the energy $\mathscr{E}(\mathbf{r},\mathbf{k})$:

$$X^{\text{even}} = \left(\mathscr{E}^0, \mathscr{E}^1, \mathscr{E}^2\right), \tag{1.54}$$

while the first three odd vector valued moments are formulated as:

$$X^{\text{odd}} = \left(\mathbf{p}\mathscr{E}^0, \mathbf{p}\mathscr{E}^1, \mathbf{p}\mathscr{E}^2\right). \tag{1.55}$$

Inserting the zeroth moment $\mathscr{E}^0$ and the first moment $\mathbf{p}\mathscr{E}^0$ into (1.48) and (1.49) delivers the particle balance equation and the current equation, respectively. While

in the particle balance equation the particle current constitutes an unknown variable, the particle current equation contains the average kinetic energy. Postulating the diffusion approximation (neglecting the kinetic energy of the particles) and assuming the shape of a heated Maxwell distribution[2] the powers of the average energy can be expressed by the carrier temperature T_{n}, under the constraint of a parabolic band structure[3], as:

$$\left\langle\!\left\langle \mathscr{E}^i \right\rangle\!\right\rangle^{1\mathrm{D}} = \frac{(2i-1)!!}{2^i}\left(k_{\mathrm{B}}T_{\mathrm{n}}\right)^i,\ \left\langle\!\left\langle \mathscr{E}^i \right\rangle\!\right\rangle^{2\mathrm{D}} = i!\left(k_{\mathrm{B}}T_{\mathrm{n}}\right)^i, \quad \text{and}$$

$$\left\langle\!\left\langle \mathscr{E}^i \right\rangle\!\right\rangle^{3\mathrm{D}} = \frac{(2i+1)!!}{2^i}\left(k_{\mathrm{B}}T_{\mathrm{n}}\right)^i \quad \text{for } i \geq 1, \tag{1.56}$$

for a one-, two- and three-dimensional electron gas. For example, the average energy $(i=1)$ for the three-dimensional case is given by:

$$\left\langle\!\left\langle \mathscr{E} \right\rangle\!\right\rangle = \frac{3}{2}k_{\mathrm{B}}T_{\mathrm{n}}. \tag{1.57}$$

5.3 Drift–Diffusion Transport Model

The Drift–Diffusion Transport model can be derived, by closing the equation system with the assumption of a local thermal equilibrium. This is realized by setting the carrier temperature T_{n} equal to the lattice temperature T_{L}. Starting with the substitution of the zeroth moment in (1.48), the particle balance equation is obtained:

$$\underbrace{\partial_t \left\langle\!\left\langle \mathscr{E}^0 \right\rangle\!\right\rangle}_{(1)} + \underbrace{\nabla_{\mathbf{r}} \left\langle\!\left\langle \mathbf{v}\mathscr{E}^0 \right\rangle\!\right\rangle}_{(2)} - \underbrace{\left\langle\!\left\langle \mathbf{v}\nabla_{\mathbf{r}}\mathscr{E}^0 \right\rangle\!\right\rangle}_{(3)} + \underbrace{\left\langle\!\left\langle \nabla_{\mathbf{r}}\mathscr{E}\nabla_{\mathbf{p}}\mathscr{E}^0 \right\rangle\!\right\rangle}_{(4)} + \underbrace{\mathrm{s}_\alpha q \left\langle\!\left\langle \nabla_{\mathbf{p}}\mathscr{E}^0 \right\rangle\!\right\rangle \nabla_{\mathbf{p}}\tilde{\varphi}}_{(5)} = -R. \tag{1.58}$$

Due to the lacking dependence of $\mathscr{E}^0$ on $\mathbf{r}$ and $\mathbf{k}$, the third, fourth and fifth term of the left side of (1.58) vanish and one obtains:

$$\partial_t \left(n w_0\right) + \nabla_{\mathbf{r}}\left(n\mathbf{V}_0\right) = -R. \tag{1.59}$$

In order to simplify the mathematical expressions, the averages of the microscopic quantities defined as $w_i = \left\langle \mathscr{E}^i \right\rangle$ and $\mathbf{V}_i = \left\langle \mathbf{v}\mathscr{E}^i \right\rangle$ will be successively inserted.

By inserting the first moment $\mathbf{p}\mathscr{E}^0$ into (1.49) the particle flux is deduced. Since the relaxation time is in the order of picoseconds, the terms containing the time

[2] For non-degenerate semiconductors the Fermi–Dirac distribution can be approximated by the Maxwell-Boltzmann distribution ($\mathscr{E}_c - \mathscr{E}_F \gg k_{\mathrm{B}}T_{\mathrm{L}}$).

[3] Close to the band edges, the relation between the wave vector $\mathbf{k}$ and the energy, also known as dispersion relation, can be approximated by an isotropic and parabolic relation $\mathscr{E}(\mathbf{k}) = \frac{\hbar^2 k^2}{2m^*}$, which corresponds to a free electron without any potential.

derivative can be omitted and still quasi-stationary behavior even for today's fastest devices is ensured [71, 224]:

$$\underbrace{\nabla_{\mathbf{r}} \left\langle\!\left\langle \mathbf{v} \otimes \mathbf{p}\mathscr{E}^0 \right\rangle\!\right\rangle}_{(1)} - \underbrace{\left\langle\!\left\langle \mathbf{v}\nabla_{\mathbf{r}} \otimes \mathbf{p}\mathscr{E}^0 \right\rangle\!\right\rangle}_{(2)} + \underbrace{\left\langle\!\left\langle \nabla_{\mathbf{r}}\mathscr{E}\nabla_{\mathbf{p}} \otimes \mathbf{p}\mathscr{E}^0 \right\rangle\!\right\rangle}_{(3)} + \underbrace{\mathrm{s}_\alpha q \left\langle\!\left\langle \nabla_{\mathbf{p}} \otimes \mathbf{p}\mathscr{E}^0 \right\rangle\!\right\rangle \nabla_{\mathbf{r}}\tilde{\varphi}}_{(4)}$$

$$= -\frac{\left\langle\!\left\langle \mathbf{p}\mathscr{E}^0 \right\rangle\!\right\rangle}{\tau_0}, \tag{1.60}$$

where τ_0 denotes the momentum relaxation time. Assuming an isotropic band structure and the diffusive limit, the non-diagonal elements of the tensors in (1.60) are zero. Therefore, the tensor of the first part of (1.60) can be approximated by its trace appropriately divided by the dimensionality of the system. Now multiplying the first term with the non-parabolicity factor H_i leads to:

$$\nabla_{\mathbf{r}} \left\langle\!\left\langle \mathbf{v} \otimes \mathbf{p}\mathscr{E}^0 \right\rangle\!\right\rangle \approx \frac{1}{\mathrm{d}} \nabla_{\mathbf{r}} \left\langle\!\left\langle \mathrm{Tr}\left(\mathbf{v} \otimes \mathbf{p}\right) \mathbb{1} \right\rangle\!\right\rangle = A\mathsf{H}_1 \nabla_{\mathbf{r}} \left(n w_1\right), \tag{1.61}$$

with A representing a dimension factor. A can be determined by taking the dimension of the system, the prefactors of the average energy for a parabolic bandstructure, and a Maxwell distribution into account. For example, considering a three-dimensional electron gas the value of A will take the form:

$$\left\langle\!\left\langle \mathbf{v} \otimes \mathbf{p}\mathscr{E}^0 \right\rangle\!\right\rangle \approx \frac{1}{3} \nabla_{\mathbf{r}} \left\langle\!\left\langle \mathrm{Tr}\left(\mathbf{v} \otimes \mathbf{p}\right) \mathbb{1} \right\rangle\!\right\rangle = \frac{2}{3} \mathsf{H}_1 \frac{3}{2} n k_{\mathrm{B}} T_{\mathrm{n}}. \tag{1.62}$$

Here, A exhibits the value $2/3$, while the average energy has been chosen according to (1.57). In the case of a one- and two-dimensional electron gas, A is equal to 2 and 1, respectively. Founding on the validity of the premise, that the kinetic energy can be described by a product ansatz:

$$\mathscr{E} = \nu \kappa(\mathbf{k}), \tag{1.63}$$

the second and third term on the left side of (1.60) vanish. The remaining fourth term can be approximated via:

$$\mathrm{s}_\alpha q \left\langle\!\left\langle \nabla_{\mathbf{p}} \otimes \mathbf{p} \right\rangle\!\right\rangle \nabla_{\mathbf{r}}\tilde{\varphi} \approx \mathrm{s}_\alpha q n w_0 \nabla_{\mathbf{r}}\tilde{\varphi}. \tag{1.64}$$

Now, assembling all derived expressions, the particle flux equation takes the following form:

$$n\mathbf{V}_0 = -\frac{\mu_0}{q} \mathsf{H}_1 A \nabla_{\mathbf{r}} \left(n w_1\right) - \mathrm{s}_\alpha n \mu_0 w_0 \nabla_{\mathbf{r}}\tilde{\varphi}. \tag{1.65}$$

The carrier mobility is given by $\mu_0 = q\tau_0/m^*_{n,p}$, where $m^*_{n,p}$ denote the effective masses for electrons and holes respectively. In combination with the Poisson equation the Drift–Diffusion Transport model can now be expressed as:

$$\partial_t \left(n w_0\right) + \nabla_{\mathbf{r}} \left(n\mathbf{V}_0\right) = -R \;\text{ with:} \tag{1.66}$$

$$n\mathbf{V}_0 = -\frac{\mu_0}{q} \mathsf{H}_1 A \nabla_{\mathbf{r}} \left(n w_1\right) - \mathrm{s}_\alpha n \mu_0 w_0 \nabla_{\mathbf{r}}\tilde{\varphi}. \tag{1.67}$$

If one additionally assumes a cold Maxwell distribution function, the highest moment w_1 can be written as:

$$w_1^{1D} = \frac{1}{2} k_B T_L, \; w_1^{2D} = k_B T_L \,, \quad \text{and} \; w_1^{3D} = \frac{3}{2} k_B T_L \tag{1.68}$$

The average carrier energy of the drift term is neglected, which is also known as the diffusion approximation. Equations (1.66)–(1.67) and the Drift–Diffusion Transport model equations (1.15)–(1.18) from Sect. 1.3 are identical under the assumption of parabolic bands, $\mathsf{H}_1 = 1$, and for a three-dimensional electron gas.

The Drift–Diffusion Transport model is the simplest widely employed macroscopic transport model in industrial Technology Computer Aided Design (TCAD) solutions. It allows to discretize its partial differential equations on an unstructured mesh and offers a stable and robust iterative solution. There is also the possibility to generalize its mobility description in order to account for an anisotropic mobility. Furthermore, due to its relative simplicity it can be applied to two and three-dimensional device structures. This especially becomes handy, when one has to account for complex geometrical device structures, material compositions, and doping profiles. However, due to the related computational high costs, three-dimensional simulations are only utilized in rare occasions, when the device structure can not be reduced to a set of simpler two-dimensional cuts.

Due to its closure relation $T_n = T_L$, the Drift–Diffusion Transport model neglects non-local effects and is, therefore, not able to accurately describe transport in short channel devices. This causes an accuracy decrease of the Drift–Diffusion Transport model for device feature lengths shorter than 100 nm [68], where one has to relax the restrictions of a constant carrier temperature in order to improve the description. Additionally, in the case of relevant temperature gradients the applied model has to cover heat flow and thermal diffusion as effects. In such situations, one has to add the energy flow to the Drift–Diffusion Transport model by taking the next higher moment equation into account.

5.4 Energy Transport Model

The Energy Transport model can be deduced by inserting the first three moments (q.v. (1.54) and (1.55)) into (1.48) and (1.49) [72]. In this way, an additional equation, the so-called energy balance equation, is gained. This extra equation incorporates the second even moment $\mathscr{E}$, while at the same time the energy flux abides as an unknown:

$$\partial_t \langle\!\langle \mathscr{E} \rangle\!\rangle + \nabla_{\mathbf{r}} \langle\!\langle \mathbf{v}\mathscr{E} \rangle\!\rangle - \langle\!\langle \mathbf{v}\nabla_{\mathbf{r}}\mathscr{E} \rangle\!\rangle + \langle\!\langle \nabla_{\mathbf{r}}\mathscr{E}\nabla_{\mathbf{p}}\mathscr{E} \rangle\!\rangle + \mathrm{s}_\alpha q \, \langle\!\langle \nabla_{\mathbf{p}}\mathscr{E} \rangle\!\rangle \nabla_{\mathbf{p}}\tilde{\varphi} = -n \frac{\langle\!\langle \mathscr{E} \rangle\!\rangle - \langle\!\langle \mathscr{E}_0 \rangle\!\rangle}{\tau_1}. \tag{1.69}$$

After similar considerations as for the Drift–Diffusion Transport model, (1.69) can be simplified to:

$$\partial_t(nw_1) + \nabla_{\mathbf{r}}(n\mathbf{V}_1) + \mathrm{s}_\alpha q n \mathbf{V}_0 \nabla_{\mathbf{r}}\tilde{\varphi} + n\frac{w_1 - w_{1,0}}{\tau_1} = 0. \tag{1.70}$$

$\mathbf{V}_1$ denotes the energy flux and w_{10} the equilibrium case of w_1. τ_1 represents the energy relaxation time. The Hydrodynamic Transport model is gained by incorporating the third moment $\mathbf{p}\mathscr{E}$ via (1.49) [72]. This yields an expression for the energy flux, which has been introduced in (1.70) and is up to now not defined in the Energy Transport model:

$$\underbrace{\nabla_{\mathbf{r}}\langle\langle \mathbf{v}\otimes\mathbf{p}\mathscr{E}\rangle\rangle}_{(1)} - \underbrace{\langle\langle \mathbf{v}\nabla_{\mathbf{r}}\otimes\mathbf{p}\mathscr{E}\rangle\rangle}_{(2)} + \underbrace{\langle\langle \nabla_{\mathbf{r}}\mathscr{E}\nabla_{\mathbf{p}}\otimes\mathbf{p}\mathscr{E}\rangle\rangle}_{(3)} + \underbrace{\mathrm{s}_\alpha q\,\langle\langle \nabla_{\mathbf{p}}\otimes\mathbf{p}\mathscr{E}\rangle\rangle\nabla_{\mathbf{r}}\tilde{\varphi}}_{(4)} = -\frac{\langle\langle \mathbf{p}\mathscr{E}\rangle\rangle}{\tau_3}. \tag{1.71}$$

The first term on the left side of (1.71) can be approximated by:

$$\nabla_{\mathbf{r}}\langle\langle \mathbf{v}\otimes\mathbf{p}\mathscr{E}\rangle\rangle \approx \frac{1}{\mathrm{d}}\nabla_{\mathbf{r}}\langle\langle \mathrm{Tr}(\mathbf{v}\otimes\mathbf{v}\mathscr{E})\,\mathbb{1}\rangle\rangle = A\mathsf{H}_2\nabla_{\mathbf{r}}(nw_2). \tag{1.72}$$

The second term of (1.71) can be reformulated, via the tensorial identity $\nabla_{\mathbf{x}}\otimes\mathbf{x}h(\mathbf{x}) = h(\mathbf{x})\nabla_{\mathbf{x}}\otimes\mathbf{x} + \mathbf{x}\otimes\nabla_{\mathbf{x}}h(\mathbf{x})$, to:

$$\langle\langle \mathbf{v}\nabla_{\mathbf{r}}\otimes\mathbf{p}\mathscr{E}\rangle\rangle = \langle\langle \mathbf{v}(\mathscr{E}\nabla_{\mathbf{r}}\otimes\mathbf{p} + \mathbf{p}\otimes\nabla_{\mathbf{r}}\mathscr{E})\rangle\rangle, \tag{1.73}$$

and the third term to:

$$\langle\langle \nabla_{\mathbf{r}}\mathscr{E}\nabla_{\mathbf{p}}\otimes\mathbf{p}\mathscr{E}\rangle\rangle = \langle\langle \nabla_{\mathbf{r}}\mathscr{E}(\mathscr{E}\nabla_{\mathbf{p}}\otimes\mathbf{p} + \mathbf{p}\otimes\nabla_{\mathbf{p}}\mathscr{E})\rangle\rangle \approx \langle\langle \mathscr{E}\nabla_{\mathbf{r}}\mathscr{E} + \nabla_{\mathbf{r}}\mathscr{E}(\mathbf{p}\otimes\mathbf{v})\rangle\rangle. \tag{1.74}$$

Taking a look at (1.73) and (1.74) reveals that they cancel each other. The fourth term on the left side of (1.71) is approximated with the same identity as in (1.72), which results in:

$$\mathrm{s}_\alpha q\,\langle\nabla_{\mathbf{p}}\otimes\mathbf{p}\mathscr{E}\rangle\nabla_{\mathbf{r}}\tilde{\varphi} = \mathrm{s}_\alpha q\,\langle\langle \mathscr{E}\nabla_{\mathbf{p}}\otimes\mathbf{p} + \mathbf{p}\otimes\nabla_{\mathbf{p}}\mathscr{E}\rangle\rangle\nabla_{\mathbf{r}}\tilde{\varphi} \tag{1.75}$$

$$= \mathrm{s}_\alpha q\,nw_1(1 + A\mathsf{H}_1)\nabla_{\mathbf{r}}\tilde{\varphi}.d \tag{1.76}$$

Merging all derived expressions gives the energy flux:

$$n\mathbf{V}_1 = -\frac{\mu_1}{q}\mathsf{H}_2 A\nabla_{\mathbf{r}}(nw_2) - \mathrm{s}_\alpha n\mu_1(1 + A\mathsf{H}_1)w_1\nabla_{\mathbf{r}}\tilde{\varphi}. \tag{1.77}$$

The quantity μ_1 denotes the energy flux mobility defined as $\mu_1 = q\tau_3/m^*_{n,p}$. Now the set of equations for the Hydrodynamic Transport models is complete and given by:

$$\partial_t(nw_0) + \nabla_{\mathbf{r}}(n\mathbf{V}_0) = -R, \tag{1.78}$$

$$n\mathbf{V}_0 = -\frac{\mu_0}{q}\mathsf{H}_1 A \nabla_{\mathbf{r}}(nw_1) - \mathrm{s}_\alpha n \mu_0 w_0 \nabla_{\mathbf{r}}\tilde{\varphi}, \tag{1.79}$$

$$\partial_t(nw_1) + \nabla_{\mathbf{r}}(n\mathbf{V}_1) + \mathrm{s}_\alpha q n \mathbf{V}_0 \nabla_{\mathbf{r}}\tilde{\varphi} + n\frac{w_1 - w_{10}}{\tau_1} = 0, \tag{1.80}$$

$$n\mathbf{V}_1 = -\frac{\mu_1}{q}\mathsf{H}_2 A \nabla_{\mathbf{r}}(nw_2) - \mathrm{s}_\alpha n \mu_1 (1 + A\mathsf{H}_1) w_1 \nabla_{\mathbf{r}}\tilde{\varphi}. \tag{1.81}$$

This set of equations is closed by assuming a heated Maxwellian distribution for the distribution function of the carriers. The concerning highest moment w_2 is then defined for the one-, two-, and three-dimensional electron gas by:

$$w_2^{1\mathrm{D}} = \frac{3}{4}(k_\mathrm{B}T_\mathrm{n})^2, \quad w_2^{2\mathrm{D}} = 2(k_\mathrm{B}T_\mathrm{n})^2, \quad \text{and} \quad w_2^{3\mathrm{D}} = \frac{15}{4}(k_\mathrm{B}T_\mathrm{n})^2. \tag{1.82}$$

Comparing (1.80) and (1.81) with Fourier's law (1.27) and the other additional thermal contributions (1.28)/(1.29) and (1.30) is not as straight forward as for the Drift–Diffusion Transport model, but can be carried out with some reasoning. Equation (1.80) is the so-called *energy flux conservation equation*. It contains a divergence term for the energy flux through the surface, which is analogous to the divergence term in Fourier's law. The time derivative of nw_1 is equivalent to the time derivative of the temperature T in Fourier's law and the remaining term with $n\mathbf{V}_0\nabla\tilde{\varphi}$ represents the source term H, which represents in the simplest case Joule heat.

One has to note, that during the derivation the diffusion approximation has been utilized and thus the so-called *convective* terms $\langle\mathbf{k}\rangle \otimes \langle\mathbf{k}\rangle$ and $\langle\mathbf{k}\rangle \cdot \langle\mathbf{k}\rangle$ were neglected against terms of the form $\langle\mathbf{k}\otimes\mathbf{k}\rangle$ and $\langle\mathbf{k}\cdot\mathbf{k}\rangle$. This causes the sole consideration of the thermal energy $k_\mathrm{B}T_\mathrm{n}$, ignoring the drift energy component of the carriers.

The limitation of this approach is that only the average energy is available to characterize the distribution function. This assumption is significantly violated in devices exhibiting lengths shorter than $\approx$50 nm [68].

Furthermore there is an arbitrary/synonymous use of the terms Hydrodynamic Transport model and Energy Transport model. The full transport model includes convective terms analog to the differential equations in fluid dynamics. These convective terms state a hyperbolic differential equation type which is hard to solve via numerical methods. Therefore, the diffusion approximation is introduced in order to get rid of these inconvenient terms. The resulting differential equations are of parabolic type and differ from the initial *hydrodynamic* problem. Hence all commonly employed four-moment models incorporating the diffusion approximation should be addressed as Energy Transport model.

A great variety of Hydrodynamic Transport and Energy Transport models have been developed [72]. They are deduced either by Bløtekjær's [28] or Stratton's [208] approach and yield with various assumptions a set of balance and flux equations.

These models are widely used in state of the art TCAD simulators. However, there are several crucial points due to the imposed assumptions during their derivation [72]:

- Band structure: Many employed models are based on the single effective parabolic band model. Due to its simplicity a closed-form solution for single effective parabolic band models exists, while even for the relatively simple non-parabolicity correction model by Kane [115] it is not possible to gain a closed-form solution.
- Non-homogeneous effects: The transport parameters (e.g. mobilities) are commonly gained by measurements or bulk simulations and described as function of the average carrier energy. This works fine for Bløtekjær's approach within, e.g., the channel region, where the absolute value of the electric field increases, while at the end of the channel, where the electric field decreases, these models can exhibit wrong results. A mixture of a cold and a hot-carrier population in this region leads to an inadequate description via the average carrier energy. This region is much smaller than the channel region for long-channel devices, and thus the incorporated error will be small. On the other hand, for devices with a channel length smaller $\approx$100 nm, the length of this region is in the order of the channel length, implying that the hot-carriers injected into the drain need a distance of about the channel length to relax. Therefore, the influence of this region is much more pronounced for future technologies.
- Closure: In order to obtain an amendable equation set, one has to transform the Boltzmann transport equation with the method of moments into an equivalent infinite set of equations and cut it at a certain moment. This set of equation has to be closed at its highest moment with a so-called *closure* relation, which is normally chosen by a heated Maxwellian distribution function. Concerning modern devices, this presents a rather crude approximation for the distribution function. One has to note, that this assumption leaves the lower order equations untouched, while the complete information of the higher order equations has to be bundled into the closure relation.
- Anisotropy: Equipartition of the energy is assumed for modeling of the temperature tensor. It has been demonstrated that such an approximation is invalid for $n^+ - n - n^+$ structures and MOS transistors. Due to the only indirect influence on the drain current in MOS transistors and a missing influence on the current in $n^+ - n - n^+$ structures, anisotropy has been addressed as an issue with negligible importance. However, the carriers penetrate much deeper into the bulk than predicted by Monte Carlo simulations, thus effecting the modeling of the energy-dependent parameters such as the mobility and impact ionization [76]. E.g., for partially depleted SOI transistors, this assumption does not hold and the Energy Transport models can not reproduce the transfer characteristics accurately. Despite the difficulty to treat the temperature tensor rigorously with additional equations for each temperature tensor component, empirical corrections offer promising results [76, 161].

- Drift energy: Due to the diffusion approximation, most Energy Transport models neglect the drift energy. Examination reveals that the drift energy can contribute up to 30% of the total energy inside the channel region [16, 204].
- Velocity overshoot: As a consequence of the afore mentioned approximations, like the truncation of the equations system, the applied closure relation, and the modeling of the transport parameters, the Energy Transport models tend to overestimate the velocity overshoot and expose a spurious velocity overshoot (SVO) at the end of the channel region of $n^+ - n - n^+$ structures. Contrary, for MOS transistors the SVO coincides with the velocity overshoot at the end of the channel and is therefore not explicitly visible.
- Hot carrier effects: Since the Hydrodynamic Transport and Energy Transport models utilize only the first two moments of the energy distribution function it is hard to model hot-carrier effects. It can be demonstrated that the energy distribution function is not uniquely defined by the concentration and the average energy. Due to the dependence on the shape of the distribution function, hot-carrier effects like impact ionization, are destined to fail, if the employed model relies exclusively on the average energy. In such cases the extension of the Energy Transport model to a Six-Moments Transport model elevates the accuracy significantly.

5.5 Six-Moments Transport Model

In order to overcome the limitations of the Hydrodynamic Transport model, two further moments can be included in the equation system. The resulting model contains six moments and is therefore called Six-Moments Transport model. Substituting the fourth moment $\mathscr{E}^2$ into (1.48) delivers the second-order energy balance equation:

$$\partial_t \left\langle\!\left\langle \mathscr{E}^2 \right\rangle\!\right\rangle + \nabla_{\mathbf{r}} \left\langle\!\left\langle \mathbf{v}\mathscr{E}^2 \right\rangle\!\right\rangle - \left\langle\!\left\langle \mathbf{v}\nabla_{\mathbf{r}}\mathscr{E}^2 \right\rangle\!\right\rangle + \left\langle\!\left\langle \nabla_{\mathbf{r}}\mathscr{E}\nabla_{\mathbf{p}}\mathscr{E}^2 \right\rangle\!\right\rangle + \mathrm{s}_\alpha q \left\langle\!\left\langle \nabla_{\mathbf{p}}\mathscr{E}^2 \right\rangle\!\right\rangle \nabla_{\mathbf{p}}\tilde{\varphi}$$
$$= -n \frac{\left\langle\!\left\langle \mathscr{E}^2 \right\rangle\!\right\rangle - \left\langle\!\left\langle \mathscr{E}_0^2 \right\rangle\!\right\rangle}{\tau_2}. \tag{1.83}$$

Reexpressing $\nabla_{\mathbf{r}}\mathscr{E}^2 = 2\mathscr{E}\nabla_{\mathbf{r}}\mathscr{E}$, the second-order energy balance equation takes the following form:

$$\partial_t (n w_2) + \nabla_{\mathbf{r}} (n\mathbf{V}_2) + \mathrm{s}_\alpha q n \mathbf{V}_1 \nabla_{\mathbf{r}}\tilde{\varphi} + n\frac{w_2 - w_{2,0}}{\tau_2} = 0. \tag{1.84}$$

The second-energy flux equation can be deduced by inserting the fifth moment $\mathbf{p}\mathscr{E}^2$ into (1.49):

$$\underbrace{\nabla_{\mathbf{r}} \left\langle\!\left\langle \mathbf{v}\otimes\mathbf{p}\mathscr{E}^2 \right\rangle\!\right\rangle}_{(1)} - \underbrace{\left\langle\!\left\langle \mathbf{v}\nabla_{\mathbf{r}}\otimes\mathbf{p}\mathscr{E}^2 \right\rangle\!\right\rangle}_{(2)} + \underbrace{\left\langle\!\left\langle \nabla_{\mathbf{r}}\mathscr{E}^2\nabla_{\mathbf{p}}\otimes\mathbf{p}\mathscr{E}^3 \right\rangle\!\right\rangle}_{(3)} + \underbrace{\mathrm{s}_\alpha q \left\langle\!\left\langle \nabla_{\mathbf{p}}\otimes\mathbf{p}\mathscr{E}^2 \right\rangle\!\right\rangle \nabla_{\mathbf{r}}\tilde{\varphi}}_{(4)}$$
$$= -\frac{\left\langle\!\left\langle \mathbf{p}\mathscr{E}^2 \right\rangle\!\right\rangle}{\tau_4}, \tag{1.85}$$

Each term on the left hand side of (1.85) is gained by the same assumptions as for the energy flux equation. The first term can be approximated by:

$$\nabla_{\mathbf{r}} \left\langle\!\left\langle \mathbf{v} \otimes \mathbf{p}\mathscr{E}^2 \right\rangle\!\right\rangle \approx \frac{1}{d} \nabla_{\mathbf{r}} \left\langle\!\left\langle \mathrm{Tr}\left(\mathbf{v} \otimes \mathbf{p}\mathscr{E}^2\right) \mathbb{1} \right\rangle\!\right\rangle = A\mathsf{H}_3 \nabla_{\mathbf{r}} \left(n w_3\right), \tag{1.86}$$

while the second and third term can be neglected due to their mutual cancellation. The fourth term on the left hand side of (1.85) is substituted via the following expression:

$$\mathrm{s}_\alpha q \left\langle\!\left\langle \nabla_{\mathbf{p}} \otimes \mathbf{p}\mathscr{E}^2 \right\rangle\!\right\rangle \approx (1 + 2A\mathsf{H}_2)\, n w_2 \nabla_{\mathbf{r}} \tilde{\varphi}. \tag{1.87}$$

Embracing now all contributions yields the second-order energy flux equation:

$$n\mathbf{V}_2 = -\frac{\mu_2}{q} \mathsf{H}_3 A \nabla_{\mathbf{r}} \left(n w_3\right) - \mathrm{s}_\alpha n \mu_2 \left(1 + 2A\mathsf{H}_2\right) w_2 \nabla_{\mathbf{r}} \tilde{\varphi}. \tag{1.88}$$

μ_2 denotes the second-order flux mobility and is define via $q\tau_4/m^*_{n,p}$. The Six-Moments Transport model exhibits the following set of equations:

$$\partial_t \left(n w_0\right) + \nabla_{\mathbf{r}} \left(n\mathbf{V}_0\right) = -R, \tag{1.89}$$

$$n\mathbf{V}_0 = -\frac{\mu_0}{q} \mathsf{H}_1 A \nabla_{\mathbf{r}} \left(n w_1\right) - \mathrm{s}_\alpha n \mu_0 w_0 \nabla_{\mathbf{r}} \tilde{\varphi}, \tag{1.90}$$

$$\partial_t \left(n w_1\right) + \nabla_{\mathbf{r}} \left(n\mathbf{V}_1\right) + \mathrm{s}_\alpha q n \mathbf{V}_0 \nabla_{\mathbf{r}} \tilde{\varphi} + n \frac{w_1 - w_{10}}{\tau_1} = 0, \tag{1.91}$$

$$n\mathbf{V}_1 = -\frac{\mu_1}{q} \mathsf{H}_2 A \nabla_{\mathbf{r}} \left(n w_2\right) - \mathrm{s}_\alpha n \mu_1 \left(1 + A\mathsf{H}_1\right) w_1 \nabla_{\mathbf{r}} \tilde{\varphi}, \tag{1.92}$$

$$\partial_t \left(n\mathbf{V}_2\right) + 2\mathrm{s}_\alpha q \mathbf{V}_1 \nabla_{\mathbf{r}} \tilde{\varphi} + n \frac{w_2 - w_{20}}{\tau_2} = 0, \tag{1.93}$$

$$n\mathbf{V}_2 = -\frac{\mu_2}{q} \mathsf{H}_3 A \nabla_{\mathbf{r}} \left(n w_3\right) - \mathrm{s}_\alpha n \mu_2 \left(1 + 2A\mathsf{H}_2\right) w_2 \nabla_{\mathbf{r}} \tilde{\varphi}. \tag{1.94}$$

As before, one has to choose an extra closure relation to define the highest moment in the equation system. This is performed for the Six-Moments Transport model by the deviation of the carrier distribution function from a heated Maxwellian distribution, which is defined by the kurtosis β. The kurtosis β of a one-, two-, and three-dimensional electron gas is defined as:

$$\beta^{1\mathrm{D}} = \frac{1}{3}\frac{w_2}{w_1^2}, \quad \beta^{2\mathrm{D}} = \frac{1}{2}\frac{w_2}{w_1^2}, \quad \text{and} \quad \beta^{3\mathrm{D}} = \frac{3}{5}\frac{w_2}{w_1^2}. \tag{1.95}$$

The prefactors $1/3$, $1/2$, and $3/5$ serve as normalization factors, respectively. Assuming a heated Maxwellian distribution and parabolic bands the kurtosis is equal to unity. For realistic devices the kurtosis range is $[0.75, 3]$, portending strong

deviations from a heated Maxwellian distribution. This leads to the following closure relation for the Six-Moments Transport model:

$$w_3^{1\mathrm{D}} = \frac{15}{8}\left(k_\mathrm{B}T_\mathrm{n}\right)^3 \beta^c, \;\; w_3^{2\mathrm{D}} = 6\left(k_\mathrm{B}T_\mathrm{n}\right)^3 \beta^c, \;\; \text{and} \;\; w_3^{3\mathrm{D}} = \frac{105}{8}\left(k_\mathrm{B}T_\mathrm{n}\right)^3 \beta^c. \quad (1.96)$$

c denotes a fit factor, where it has been found in [70, 125] that a value of $c = 2.7$ yields good results for w_3 in the source and channel regions.

6 The Analogy Between the Drift–Diffusion Transport Model and the Poisson–Nernst–Planck Model

The Poisson–Nernst–Planck [36, 41, 182] model describes the charge distribution and charge transport phenomena in electrolytes. It can be deduced by an averaging procedure from a Langevine model [182]. During the ensemble averaging process the many independent realizations of the stochastic system are bundled and lead to a continuous and steady state description of the system mathematically analog to the Drift–Diffusion Transport model. Instead of the electron and hole assisted charge transport in semiconductors, in electrolytes the ionic components are the charge carriers responsible for the transport and analogously to the Drift–Diffusion Transport model gradients in the electrostatic potential and the spatial concentration of the charged carriers raise forces, trying to extinguish the imbalance. Hence, similar physical conditions lead to a similar mathematical description of the system.

For a binary salt (e.g. *NaCl*) the Poisson–Nernst–Planck equation system may be written as [36]:

$$\mathbf{j}_\pm = -D_\pm\left(\nabla c_\pm + z_\pm c_\pm \nabla\varphi\right), \quad (1.97)$$

$$\nabla\cdot\left(\varepsilon\nabla\varphi\right) = \frac{F^2}{\varepsilon_0 RT}\left(c_- - c_+\right), \quad (1.98)$$

$$\nabla\cdot\mathbf{j}_\pm = 0. \quad (1.99)$$

$\mathbf{j}_\pm$ denotes the ionic flux, $D_\pm$ describe the diffusion coefficients, $c_\pm$ the ionic charge distributions, and $z_\pm$ the valency of the ion types, respectively. F stands for the Farrady constant, R describes the gas constant and T depicts the temperature of the liquid. In the equation system (1.97)–(1.99) has been assumed that the ionic components are fully dissolved and thus there is no generation-recombination term like in (1.15) and (1.16) and all transient effects are subsided.

Although, there is no doping profile like in common semiconductor devices, and, therefore, no C term in (1.97) like in (1.2), the boundaries of typical domains are charged, either due to differences in the work functions of the solute and the domain wall or through open binding sites at the surface of the boundaries (site-binding model by Yates [237]).

One of the application fields of the Poisson–Nernst–Plank model is the description of transport phenomena in natural and artificial nanopores/ion channels [36, 41, 182]. Biological ion channels constitute the key to understand and control the interaction between cells and their environment. They serve as gateways for various stimuli and the exchange of nutrition and secretion. Ion channels can be opened and closed to the flow of ions in a reliable and reversible manner by certain stimuli. In the open state many ion channels are restrictive to the conducted ion type: Some only conduct anions but not cations and vice versa, or are even more distinct and allow only one certain type to permeate. It was shown that artificial nanopores are feasible and exhibit similar behavior to biological ion channels. For instance, artificial ion channels are able to rectify electric current [13,194–197] or pump potassium ions against concentration gradients in response to a harmonically with time oscillating field [198]. Parameters like the amount of pores, their size and shape can be controlled within a few nanometers [198].

The analogy between the Drift–Diffusion Transport model and the Poisson–Nernst–Plank model stands out even more clearly by comparing the scaled equations of both descriptions [20, 184].

7 Modeling of Transport Parameters

The transport models presented in the previous sections exhibit various material parameters like mobilities. In order to obtain a sufficiently accurate and reliable device simulation one has to thoroughly describe these parameters. Most sufficiently accurate analytical models are derived from theoretical considerations and verified against data extracted from measurements.

7.1 Parameters for the Drift–Diffusion Transport Model

The carrier mobilities in semiconducting materials are determined by various physical mechanisms. The charge carriers experience scattering events by thermal lattice vibrations, ionized impurities, neutral impurities, vacancies, interstitials, dislocations, surfaces and with themselves. Furthermore mobility may depend on the driving electric field: There is a mobility reduction due to the saturation of the drift velocity of warm and hot carriers. Even though rigorous first principle models for the carrier mobilities are available, they are complicated and hard to implement and therefore often replaced by less demanding empirical expressions which are fitted to experimental data [185].

7.1.1 Carrier Mobilities

Due to the overwhelming complexity of rigorous models, we will also stick to the more appealing engineering approach handling the mobilities by fitted empirical models. Commonly it is assumed that the effective carrier mobility can be written as:

$$\mu_\nu^{\mathrm{LISF}} = \mu_\nu^{\mathrm{LISF}}\left(\mu_\nu^{\mathrm{LIS}}\left(\mu_\nu^{\mathrm{LI}}\left(\mu_\nu^{\mathrm{L}}\right)\right)\right). \tag{1.100}$$

ν denotes the charge carrier type (electrons or holes), and μ_ν^{LISF} depicts the effective mobility influenced by lattice scattering (L), ionized impurity scattering (I), surface roughness scattering (S) and carrier heating (F). This multi-level approach implies that the different scattering mechanisms can be separated and the effective mobilities can be obtained via consecutive sophistication of the model by including additional scattering mechanisms.

Lattice Scattering

Atoms in the semiconductor lattice vibrate around their equilibrium positions. Due to these oscillations, even in pure and perfectly ordered semiconductors, carriers are scattered by the vibrating lattice and the lattice mobility μ_ν^{L} depends on the lattice temperature. For simulation applications, an empirical power law is convenient [184]:

$$\mu_\nu^{\mathrm{L}} = \mu_\nu^0 \left(\frac{T}{300\,\mathrm{K}}\right)^{-\alpha_\nu}, \quad \nu = n, p. \tag{1.101}$$

The parameters μ_ν^0 and α_ν exhibit a certain spread of values [184]. For instance, the parameters for the electron mobility are frequently in the range $1{,}240\,\mathrm{cm}^2\,(\mathrm{Vs})^{-1} < \mu_n^0 < 1{,}600\,\mathrm{cm}^2\,(\mathrm{Vs})^{-1}$ and $2.2 < \alpha_n < 2.6$ for silicon. A possible explanation lies in the stochastic nature of the device fabrication process and the measurement itself. Corresponding parameters for *III–V* semiconductors can be found in [158].

Ionized Impurity Scattering

The mobility reduction in semiconductor devices due to scattering by charged impurities is a major effect. The influence of lattice and impurity scattering must be combined in an appropriate way in order to gain an effective mobility.

Caughey and Thomas introduced an empirical model which is able to fit the experimental data [34]. The exploited empirical expression is:

$$\mu_\nu^{\mathrm{LI}} = \mu_\nu^{\mathrm{min}} + \frac{\mu_\nu^{\mathrm{L}} - \mu_\nu^{\mathrm{min}}}{1 + \left(\frac{N_\mathrm{I}}{N_\nu^{\mathrm{ref}}}\right)^{\alpha_\nu}}, \tag{1.102}$$

where:

$$N_{\mathrm{I}} = \sum_i |Z_i|\, N_i \tag{1.103}$$

is the sum over all charged impurities and Z_i denotes the charge state of the impurity. For example, single ionized impurities (e.g. boron, phosphorus and aluminum in silicon) $|Z_i| = 1$. The Caughey and Thomas model requires three free parameters in order to fit the experimental data. Typical values for silicon at room temperature are $\mu_n^{\mathrm{min}} = 80\,\mathrm{cm}^2\,(\mathrm{Vs})^{-1}$, $N_n^{\mathrm{ref}} = 1.12\,10^{17}\,\mathrm{cm}^{-3}$ and $\alpha_n = 0.72$ for electrons and $\mu_p^{\mathrm{min}} = 45\,\mathrm{cm}^2\,(\mathrm{Vs})^{-1}$, $N_p^{\mathrm{ref}} = 2.23\,10^{17}\,\mathrm{cm}^{-3}$ and $\alpha_n = 0.72$ for holes.

Lombardi introduced an alternative mobility description for silicon in [136], based on the Matthiessen rule, and optimized for numerical simulations. The mobility model after Masetti [141] extends the description of Caughey and Thomas to high doping concentrations. For *III–V* semiconductors the required parameters can be found in the book by Palankovski and Quay [158].

Surface/Interface Scattering

The finite spatial dimensions of a semiconductor cause the perfect crystal periodicity to break at the crystal surfaces. The interfaces between different materials exhibit different lattice constants and thus lead to ineluctable imperfections. These imperfections have a huge impact, if the current is flowing primarily close to the interface, as commonly in modern MOSFETs. Usually, the mobility along a surface is significantly smaller than in the center of the crystal. The transition from the high mobility region in the bulk to the low mobility region at the surface is smooth.

An empirical model describing such a smooth transition depending on the depth has been proposed by [184]:

$$\mu_{\nu\mathrm{LIS}} = \frac{\mu_\nu^{\mathrm{ref}} + \left(\mu_\nu^{\mathrm{LI}} - \mu_\nu^{\mathrm{ref}}\right)(1 - F(y))}{1 + F(y)\left(\frac{S_\nu}{S_\nu^{\mathrm{ref}}}\right)^{\gamma_\nu}}. \tag{1.104}$$

The depth dependence $F(y)$ is defined by:

$$F(y) = \frac{2\exp\left(-\frac{y^2}{y^{\mathrm{ref}2}}\right)}{1 + \exp\left(-2\frac{y^2}{y^{\mathrm{ref}2}}\right)}, \tag{1.105}$$

where the parameter y^{ref} is in the typical range from 2 to 10 nm. The pressing forces S_n and S_p are equal to the magnitude of the normal field strength at the interface, if the carriers are pulled by it otherwise they are zero. The parameters are fitted to experimental data.

Also the mobility model after Lombardi [136] can be employed due to the inclusion of surface acoustic phonon scattering and surface roughness scattering. An overview about the vast number utilized mobility models is documented in [100].

Field Dependent Mobility

The carrier energy can be split into two basic contributions, the thermal energy, which is related to the random thermal motion of the carriers, and the kinetic energy, describing the kinetic energy of the charge carriers $\frac{mv^2}{2}$. So the average energy per particle is given by:

$$w = \frac{3}{2} k_{\mathrm{B}} T_{\mathrm{n}} + \frac{1}{2} m v^2, \tag{1.106}$$

where T_n denotes the carrier temperature. Exerting the charged particles to an electric field, accelerates them and thus increases the kinetic energy, while scattering events convert kinetic energy to thermal energy and increase the carrier temperature. For weak electric fields the mobility is constant with respect to the field, and therefore the relation between the velocity and the electric field is linear.

Compared to the movement caused by the externally applied electric field the thermal velocity of electrons and holes is large and hence the carrier temperature is equal to the lattice temperature.

For large electric fields the relationship between the electric field and the carrier velocity begins to deviate from linear and saturates for very high fields. Within a simulation framework this effect is normally taken care of by a field dependent mobility.

Also here empirical mobility expressions are employed whose parameters are determined by fitting experimental data. A widely used expression was introduced by Caughey and Thomas [34]:

$$\mu_\nu^{\mathrm{LISF}}(E) = \frac{\mu_\nu^{\mathrm{LIS}}}{\left(1 + \left(\frac{\mu_\nu^{\mathrm{LIS}} E}{v_\nu^{\mathrm{sat}}}\right)^{\beta_\nu}\right)^{1/\beta_\nu}}, \tag{1.107}$$

or an alternative formulation by Jaggi [108, 109]:

$$\mu_\nu^{\mathrm{LISF}}(E) = \frac{2\mu_\nu^{\mathrm{LIS}}}{\left(1 + \left(\frac{2\mu_\nu^{\mathrm{LIS}} E}{v_\nu^{\mathrm{sat}}}\right)^{\beta_\nu}\right)^{1/\beta_\nu}}. \tag{1.108}$$

Both expressions contain the same parameters, the low-field mobility μ_ν^{LIS} and the saturation velocity v_ν^{sat}, respectively. These parameters pose the low-field and high-field limits of the carrier velocity as a function of the electric field:

$$\lim_{E\to 0} \mu_\nu^{\mathrm{LISF}}(E) = \mu_\nu^{\mathrm{LIS}}, \quad \lim_{E\to\infty} v_\nu(E) = \lim_{E\to\infty} \mu_\nu^{\mathrm{LISF}}(E) \times E = v_\nu^{\mathrm{sat}}. \tag{1.109}$$

Silicon at room temperature is characterized by the following parameters: $v_n^{\text{sat}} = 10^7\,\text{cm}\,\text{s}^{-1}$, $\beta_n = 2$, $v_p^{\text{sat}} = 8 \times 10^6\,\text{cm}\,\text{s}^{-1}$ and $\beta_p = 1$. For high electric fields both models (1.108) and (1.109) reach asymptotically $\mu_{\text{LISF}}^{v} \sim 1/E$ as previously asserted.

For higher order transport models, the description of mobility becomes more complex due to the dependence on the carrier temperature [15, 16, 83, 84, 132, 213].

7.1.2 Carrier Generation and Recombination

Generation-recombination phenomena are involved in many fundamental effects like leakage current and device breakdown. In thermal equilibrium there is a dynamic balance between the generation and recombination of electron–hole pairs, which yields into an equilibrium concentration n_0 for electrons and p_0 for holes:

$$n_0 = N_\text{c} \exp\left(\frac{\mathscr{E}_F - \mathscr{E}_c}{k_\text{B} T_\text{n}}\right) = n_i \exp\left(\frac{\mathscr{E}_F - \mathscr{E}_i}{k_\text{B} T_\text{n}}\right), \tag{1.110}$$

$$p_0 = N_\text{v} \exp\left(\frac{\mathscr{E}_v - \mathscr{E}_F}{k_\text{B} T_\text{n}}\right) = p_i \exp\left(\frac{\mathscr{E}_i - \mathscr{E}_F}{k_\text{B} T_\text{n}}\right). \tag{1.111}$$

N_c/N_v, and n_i/p_i denote the effective DOS for the conduction and valence band and the intrinsic concentrations for electrons and holes, respectively, while $\mathscr{E}_i$ describes the intrinsic energy. The product of the equilibrium concentrations for electrons and holes results in

$$n_0\, p_0 = N_\text{c} N_\text{v} \exp\left(\frac{\mathscr{E}_c - \mathscr{E}_v}{k_\text{B} T_\text{n}}\right) = n_i^2, \tag{1.112}$$

with the introduction of the intrinsic concentration:

$$n_i = \sqrt{N_\text{c} N_\text{v}} \exp\left(-\frac{\mathscr{E}_g}{2 k_\text{B} T_\text{n}}\right). \tag{1.113}$$

Equations (1.110) and (1.111) are based on Boltzmann statistics and thus are only valid for non-degenerate semiconductors.

If the electron and hole concentrations differ from their equilibrium concentrations, the balance of generation and recombination rates is disturbed. Regions exhibiting excess carriers ($n\,p > n_i^2$) will experience mainly recombination while regions with a carrier deficiency ($n\,p < n_i^2$) will encounter a domination of the generation process.

Various physical mechanisms can cause the generation/recombination of an electron–hole pair. For instance, the absorption or emission of a photon, the absorption or emission of a phonon, three particle transitions, and transitions assisted by recombination centers. The impact of these mechanisms depends on the operation conditions and the properties of the employed materials.

The transition from the valence band to the conduction band requires energy. The needed amount of energy to lift an electron from the valence band to the conduction

band or a hole from the conduction band to the valence band is at least the band gap energy $\mathscr{E}_g$. This energy can be gained by several means:

- Photons: Each photon carries an energy of $\hbar\omega$. If the energy of the photon is equal or greater than the band gap energy $\mathscr{E}_g$, an electron absorbing photon is able to raise into the conduction band.
- Phonons: Phonons represent the quantization of thermal lattice vibrations and are able to transfer energy to the charge carriers.
- Collisions: An electron in the conduction band with high energy is able to transfer enough energy to an electron in the valence band, so that it is elevated into the conduction band.

Trap Assisted Recombination and Generation

Silicon and Germanium are indirect semiconductors and it was experimentally found that these materials primarily generate and recombinate electron–hole pairs via trap centers. This so-called Shockley–Read–Hall generation-recombination mechanism is called after the authors who constituted the theory [81, 189]. The indirect generation-recombination process is a non-radiative process and can be separated into four independent processes (Fig. 1.2):

(a) Electron Capture: An electron jumps from the conduction band into an unoccupied trap state and fills it.
(b) Electron Emission: An electron occupying a trap site elevates into the conduction band and leaves the trap state empty.
(c) Hole Capture: An electron jumps from a trap site into an unoccupied valence band site, neutralizes a hole and leaves the trap site empty.
(d) Hole Emission: An electron from the valence band is lifted into the trap site occupies it and generates a hole in the valence band.

The reaction rates are given by:

$$\nu_a = k_a n N_t^0 \quad \text{(electron capture)}, \tag{1.114}$$

$$\nu_b = k_b N_t^- \quad \text{(electron emission)}, \tag{1.115}$$

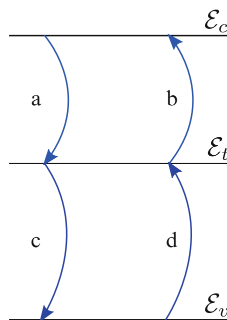

Fig. 1.2 The transition process can be split up into four partial processes

$$v_c = k_c p N_t^- \ \text{(hole capture)}, \tag{1.116}$$
$$v_d = k_d N_t^0 \ \text{(hole emission)}, \tag{1.117}$$

where Nt^0 denotes the concentration of neutral traps and N_t^- describes the concentration of occupied traps. The total trap concentration N_t is calculated by $N_t = N_t^0 + N_t^-$. The fraction of occupied traps is defined as $f_t = N_t^- / N_t$, $1 - f_t = N_t^0 / N_t$. The rate equation v_a describes the electron capture rate and assumes that the transmission rate is proportional to the number of carriers in the conduction band n and the number of neutral (free) traps N_t^0. The electron emission rate v_b is expected to be proportional to the number of electrons N_t^- in the traps exclusively, due to the majority of empty states in the conduction band (i.e. the distribution function f is close to zero, hence $1 - f$ is close to 1). A consideration for holes is similar. The principle of detailed balance is valid for thermal equilibrium and allows the assumption of:

$$v_a^{eq} = v_b^{eq}, \quad v_c^{eq} = v_d^{eq}. \tag{1.118}$$

Thus, we obtain:

$$k_b = k_a \underbrace{n_0 \frac{1 - f_{t,0}}{f_{t,0}}}_{n_1}, \tag{1.119}$$

$$k_d = k_c \underbrace{p_0 \frac{f_{t,0}}{1 - f_{t,0}}}_{p_1}, \tag{1.120}$$

with the auxiliary concentrations n_1 and p_1. $f_{t,0}$ describes the fraction of occupied traps in thermal equilibrium. With the aid of the definitions (1.119) and (1.120) the net recombination rates can be expressed as:

$$R_n^{\text{SRH}} = v_a - v_b = k_a N_t \left(n\,(1 - f_t) - n_1 f_t\right), \tag{1.121}$$
$$R_p^{\text{SRH}} = v_c - v_d = k_c N_t \left(p\, f_t - p_1\,(1 - f_t)\right). \tag{1.122}$$

From a general viewpoint the recombination rates R_n^{SRH} and R_p^{SRH} are not automatically equal. This is taken into account by an additional conservation equation to the semiconductor equations:

$$\frac{\partial N_t^-}{\partial t} = R_n^{\text{SRH}} - R_p^{\text{SRH}}, \tag{1.123}$$

which has to be considered in the whole domain. Provided that the system is in steady state, the time derivative vanishes and the net recombination rate of electrons is equal to the net recombination rate for holes. Under these circumstances one can calculate the trap occupancy function explicitly:

$$f_t = \frac{k_a n + k_c p_1}{k_a\,(n + n_1) + k_c\,(p + p_1)}. \tag{1.124}$$

After introducing the carrier lifetimes $\tau_p^{-1} = k_a N_t$ and $\tau_n^{-1} = k_c N_t$ one is able to write down the recombination rate after Shockley and Read [189], and Hall [81]:

$$R^{\mathrm{SRH}} = \frac{n\,p - n_i^2}{\tau_p\,(n+n_1) + \tau_n\,(p+p_1)}. \tag{1.125}$$

Traps are defined by defects with an energy level $\mathscr{E}_t$ and their concentration N_t. The interaction of carriers and trap centers is described by the capture cross section σ_n for electrons and σ_p for holes and linked to the rate constants and the carrier lifetimes by:

$$k_a = \sigma_n v_{th}^n,\;\; \tau_b^{-1} = \sigma_n v_{th}^n N_t,\;\; k_c = \sigma_p v_{th}^p,\;\; \tau_d^{-1} = \sigma_p v_{th}^p N_t, \tag{1.126}$$

with the thermal velocities v_{th}^n and v_{th}^p for electrons and holes, respectively.

Presuming that $np > n_i^2$ the recombination rate is larger than zero, thus recombination takes place until $np = n_i^2$. On the other hand if $np < n_i^2$ the generation is dominant which means that the carrier concentration increases until $np = n_i^2$ again. The carrier lifetimes τ_n and τ_p determine the transient response of the material in the non-equilibrium case. The smaller the carrier lifetime the bigger the recombination rate becomes and, hence, the faster the material gains equilibrium again.

Photon Transition

Direct generation/recombination can be associated with photon emission or absorption. Direct band to band transitions are only of importance for direct bandgap semiconductors like *GaAs*, due to the relatively small momentum of photons. In silicon and germanium the direct generation-recombination mechanism is therefore negligible. Starting with the electron–hole reaction:

$$e^- + h^+ \rightleftharpoons 0, \tag{1.127}$$

two distinct processes are available:

(a) Electron–Hole Recombination: An electron moves from the conduction band into the valence band and neutralizes a hole.
(b) Electron–Hole Generation: An electron from the valence band absorbs a photon which exhibits an energy larger than the bandgap energy and moves to the conduction band leaving a hole in the valence band.

The rate constants k_a^{opt} and k_b^{opt} allow a description of the rate equations for optical generation/recombination:

$$v_a = k_a^{\mathrm{opt}}(T)\,n\,p, \tag{1.128}$$

$$v_b = k_b^{\mathrm{opt}}(T). \tag{1.129}$$

These two rates have to be equal in thermal equilibrium:

$$v_{a,0} = v_{b,0} \rightarrow k_a^{\mathrm{opt}} n_i^2 = k_b^{\mathrm{opt}}. \tag{1.130}$$

This way the net recombination rate results in:

$$R^{\mathrm{opt}} = v_{a,0} - v_{b,0} = k_a^{\mathrm{opt}} \left(n\,p - n_i^2\right). \tag{1.131}$$

Here, once more the term $\left(n\,p - n_i^2\right)$ appears, which takes care of driving the system back into equilibrium.

Auger Generation-Recombination

The Auger generation-recombination is a three particle process, but only two move from one band to another. The third particle provides or receives the excess energy and moves to another energy level within the same band, where it releases its energy to thermal vibrations in the case of recombination. In the following we describe the direct band to band Auger process which is also known as phonon-assisted Auger process. This process is covered by four partial reactions:

$$2e^- + h^+ \rightleftharpoons e^- \tag{1.132}$$

$$e^- + 2h^+ \rightleftharpoons h^+ \tag{1.133}$$

(a) Electron Capture: An electron from the conduction band jumps into the valence band. The excess energy is transferred to another conduction band electron while the electron in the valence band neutralizes a hole.
(b) Electron Emission: A valence band electron gains energy from a high energetic conduction band electron and is lifted into the conduction band, leaving a hole behind.
(c) Hole Capture: An electron from the conduction band moves to the valence band. The excess energy is transferred to another hole. The new electron in the valence band neutralizes a hole.
(d) Hole Emission: A valence electron is lifted by a high energetic hole into the conduction band. A new hole remains in the valence band.

The reaction rates are written with the rate constants c_n, e_n, c_p and e_p as follows:

$$v_a = c_n\,n^2 p \;\; \text{(electron capture)}, \tag{1.134}$$

$$v_b = e_n\,n \;\; \text{(electron emission)}, \tag{1.135}$$

$$v_c = c_p\,p^2 n \;\; \text{(hole capture)}, \tag{1.136}$$

$$v_d = e_p\,p \;\; \text{(hole emission)}. \tag{1.137}$$

the n^2p term in (1.134) is caused by the need for two electrons from the conduction band and one hole from the valence band. On the other hand, although there are two electrons involved in the electron emission process in (1.135), only one electron from the conduction band participates.

Assuming thermal equilibrium, the principle of detailed balance demands:

$$\nu_{a,0} = \nu_{b,0} \rightarrow c_n n_i^2 = e_n, \tag{1.138}$$

$$\nu_{c,0} = \nu_{d,0} \rightarrow c_p n_i^2 = e_p. \tag{1.139}$$

The constants c_n and c_p denote the Auger coefficients and the net recombination rate for the Auger process is expressed as:

$$R^{\mathrm{Au}} = \nu_a - \nu_b + \nu_c - \nu_d = (c_n n + c_p p)\left(np - n_i^2\right). \tag{1.140}$$

Once more the $\left(np - n_i^2\right)$ term emerges and models the tendency of the system to reach an equilibrium. Commonly employed values for silicon at room temperature are $c_n = 2.9 \times 10^{-31}\,\mathrm{cm}^6\,\mathrm{s}^{-1}$ and $c_p = 9.9 \times 10^{-32}\,\mathrm{cm}^6\,\mathrm{s}^{-1}$.

Impact Ionization

Impact ionization is a process only generating electron–hole pairs via high energetic carriers. In the microscopic picture there is no difference between Auger generation and impact ionization. The difference is related to the energy sources. The Auger generation process was deduced with the aid of the principle of detailed balance, which is only valid in thermal equilibrium, while impact ionization is a typically non-equilibrium process requiring large fields.

For impact ionization two partial processes have to be taken into account:

$$e^- \rightharpoonup 2e^- + h^+, \tag{1.141}$$

$$h^+ \rightharpoonup 2h^+ + e^-. \tag{1.142}$$

(a) Electron Emission: A valence electron consumes energy from a high energetic electron in the conduction band and jumps into the conduction band, leaving a hole behind.
(b) Hole Emission: A valence electron moves to the conduction band by the energy from an high energetic hole in the valence band. A hole is generated in the valence band.

Even though these two partial processes are equivalent to the Auger processes (b) and (d), for modeling impact ionization, the reaction rates are differently expressed in the framework of the Drift–Diffusion Transport model:

$$\nu_a = \alpha_n \frac{\mathbf{j}_n}{q}, \tag{1.143}$$

$$\nu_b = \alpha_p \frac{\mathbf{j}_p}{q}. \tag{1.144}$$

α_n and α_p depict the ionization coefficients for electrons and holes. They are given by the reciprocal of the average distance carriers travel between successive ionization events. An electron generates on average one electron–hole pair, when it travels of $1/\alpha_n$. The total generation rate is determined by:

$$G^{\mathrm{II}} = v_a + v_b = \frac{\alpha_n}{q}\,|\mathbf{j}_n| + \frac{\alpha_p}{q}\,|\mathbf{j}_p|\,. \tag{1.145}$$

Thus the impact ionization rate is proportional to the current densities, while the Auger generation is proportional to the carrier concentrations (1.135) and (1.137). Therefore, Auger generation takes place in regions with high mobile carrier concentrations and not necessarily high current densities, while impact ionization requires a significant current flow. Theoretical and experimental surveys indicate an exponential dependence of the ionization coefficients on the electric field:

$$\alpha_n = A_n \exp\left(-(B_n/E)^{\beta_n}\right),\ \ \alpha_p \exp\left(-(B_p/E)^{\beta_p}\right). \tag{1.146}$$

$E = \mathbf{E}\cdot\mathbf{j}/|\mathbf{j}|$ denotes the field component along the direction of the current flow. Chynoweth [40] found the exponents β_n and β_p to be unity on the basis of large experimental data sets. Shockley supports these findings by theoretical considerations [187], while Wolff predicts them to be two via a different approach [230].

Practically, β_n and β_p are adjusted between one and two in order to get a good matching to experimental data. Typical values for silicon at room temperature are $A_n = 7.03\times10^5\,\mathrm{cm}^{-1}$, $B_n = 1.231\times10^6\,\mathrm{V\,cm}^{-1}$, $\beta_n = 1$, $A_p = 6.71\times10^5\,\mathrm{cm}^{-1}$, $B_p = 1.693\times10^6\,\mathrm{V\,cm}^{-1}$ and $\beta_p = 1$.

In the case of *III–V* semiconductors the work from Palankovski and Quay [158] provides the necessary data. Due to the non-trivial dependence on several quantities, modeling of the parameters is much harder for higher order transport models [67, 69, 72].

7.1.3 Modeling Biologically Sensitive Field-Effect Transistors

There are two common approaches for simulating biochemical systems. In the first, microscopic approach, every molecule is characterized by its electrostatic properties and free to move within the solute, trying to minimize the acting forces between them and, thus, minimizing the energy of the system. This is typically accomplished by a stochastic Monte Carlo process [134]. In the second macroscopic approach the system is characterized by a set of partial differential equations with well chosen boundary conditions. While the description of the system via its fundamental electrostatic interaction between single molecules is beneficial, the required amount of memory and the rather poor convergence rate in comparison to other methods ($\propto \frac{1}{\sqrt{N}}$, N is the sample size) pose computational problems. The vast amount of molecules/atoms in the solute is the reason for the high memory consumption. 1 ml of water contains about $\approx 3.35\,10^{22}$ of water molecules. Therefore,

many simulations restrict to the molecules of interest and describe the surrounding water molecules by an average relative permittivity of $\sim$80, but the overall memory consumption is still quite high due to the fact that macromolecules regularly contain several thousand atoms. There are further ways to reduce the memory consumption, however, it remains an issue, so one is restricted to small volumes and/or short time scales ($\sim 10^{-15}$ s, [77, 241]).

On the contrary, the approach based on differential equations is less time and memory consuming, but neglects the quantized structure of the system and treats quantities as continuous. This complicates the description of the interaction between the molecules and also can lead to problems at low buffer concentrations [228]. We will follow the second approach below.

At first one has to identify the different parts of the simulation domain and classify them. There are: the zone where the macromolecules are contained, the region comprising the buffer, the dielectric and the semiconducting region (shown in Fig. 1.3). The devices are in the micrometer regime, even biologically sensitive field-effect transistors (BioFETs) utilizing nanowires commonly exhibit a length in the micrometer regime [56, 80, 203, 238] and therefore it is valid to model the semiconducting part via the Poisson equation, describing the charge distribution within the semiconductor, and the Drift–Diffusion Transport model taking care of the charge transport at least along the carrier transport direction [184, 214]. The dielectric is assumed to be a perfect isolator without charges modeled with the Laplace equation. The Stern layer[4] is covered by the Laplace equation and a relative permittivity of $\varepsilon_{\mathrm{Ana}} \approx 80$ in order to guarantee a minimal distance of the charged zone holding the macromolecules to the oxide interface. Depending on the preparation of the device there can be charges at the oxide interface (q.v. site-binding model). Frequently the surface sites are passivated before the macromolecules are attached

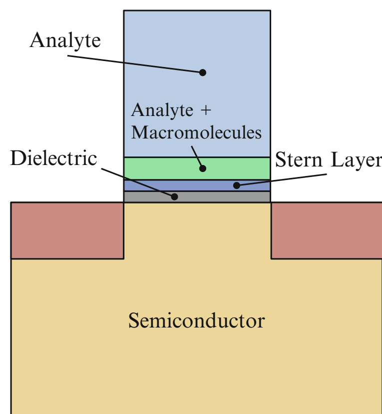

Fig. 1.3 Illustrating the different simulation zones

[4] Stern was the first to recognize, that the finite dimensions of dissolved ions cause a layer depleted from charges at interfaces (q.v. Sect. 8.2).

to avoid perturbing charge accumulation at the open oxide sites and to prepare the surface with certain functional groups allowing to attach (link) the macromolecules to the surface. The dimensions of the zone holding the charged macromolecules and their charge density can either be obtained by measurements or has to be estimated from the partial charge of a single macromolecule, derived from a protein data bank [167], and extrapolated. This zone and the rest of the electrolyte region are covered by several modeling approaches and will be explained in the sequel.

Poisson–Boltzmann Model

The Poisson–Boltzmann model is probably the most prominent one. For several mMol salt concentrations upwards it yields good results based on the assumption that the dissolved buffer ions are in thermodynamical equilibrium with their environment and only depend on the local potential. This premise allows to describe the buffer as sum over all ionic species weighted with Boltzmann type terms $e^{\frac{q\Psi}{k_{\mathrm{B}}T}}$ and their valences:

$$\varepsilon_0 \nabla \cdot (\varepsilon_{\mathrm{Ana}} \nabla \Psi(x,y)) = -\sum_{\xi \in S} \xi \; q \; c_{\xi}^{\infty} \; e^{-\xi \frac{q}{k_{\mathrm{B}}T}(\Psi(x,y)-\Psi_{\mu})} + \rho_{\mathrm{Space}}(x,y). \tag{1.147}$$

ξ is the valence of the ions in the electrolyte, Ψ_{μ} is the chemical potential, c_{σ}^{∞} is the ion concentration in equilibrium, while $\varepsilon_{Ana} \approx 80$ is the relative permittivity of water. ρ_{Space} represents the average space charge density in the simulation zone, where the charged macromolecules are contained.

Poisson–Boltzmann Model with Sheet Charge

If the charged macromolecules are directly linked to the surface and not dispensed in a gel, the zone height is typically in the deca- nanometer regime. Therefore, it will be extremely small compared to the rest of the device dimensions and it is justified to save mesh points by substituting this region by an equivalent sheet charge $\sigma_{\mathrm{Sheet}}(x)$ at the surface y_0:

$$\varepsilon_0 \nabla \cdot (\varepsilon_{\mathrm{Ana}} \nabla \Psi(x,y)) = -\sum_{\xi \in S} \xi \; q \; c_{\xi}^{\infty} \; e^{-\xi \frac{q}{k_B T}(\Psi(x,y)-\Psi_{\mu})} + \sigma_{\mathrm{Sheet}}(x)\, \delta(y-y_0). \tag{1.148}$$

Poisson–Boltzmann Model with Homogenized Interface Conditions

A similar but somewhat refined model is derived in [88, 89, 172]. The authors handled the multi-scale problem by exchanging the fast varying charge distribution at the surface (e.g. Proteins or DNA fragments scattered over the functionalized

surface) by two interface conditions. These interface conditions describe the effects of the charge and the dipole moment of the biofunctionalized layer containing the charged macromolecules:

$$\varepsilon_{\text{Oxid}}\, \partial_y \Psi(0-,x) - \varepsilon_{\text{Ana}} \partial_y \Psi(0+,x) = -\frac{C(x)}{\varepsilon_0}, \tag{1.149}$$

$$\Psi(0-,x) - \Psi(0+,x) = -\frac{D_y(x)}{\varepsilon_{\text{Ana}}\varepsilon_0}. \tag{1.150}$$

Here, $\Psi(0-)$ denotes the potential in the oxide, while $\Psi(0+)$ relates to the potential in the solute. The first equation describes the jump in the field, while the second introduces a dipole moment causing a shift of the potential (which can be accounted for by adjusting the potential in the analyte). $C(x)$ is the averaged (homogenized) charge density at the dielectric–electrolyte interface and can either be determined by experimental data or derived from first principle calculations via a data set from a protein data bank [167]. $D_y(x)$ expresses the averaged perpendicular dipole moment density and has to be gained from first principle calculations. For instance, the adaptive Poisson–Boltzmann Solver (APBS) [18,94,95] allows to assign partial charges to every atom for the desired macromolecule, and thus the calculation of the overall charge and in conjunction with the relative distances between the atoms also the dipole moment of the molecule. This charge and dipole moment can be extrapolated to the mean charge and mean dipole moment assuming an average distance between the macromolecules.

Extended Poisson–Boltzmann Model

The extended Poisson–Boltzmann model [228] is able to include the average closest possible approach of two ions in the liquid. This allows to include the Stern layer within this formulation without the need to add an ion free zone between the dielectric and the region where the Poisson–Boltzmann model is calculated. Furthermore, the minimal possible distance between two ions a is in this model a fit parameter and can therefore account for the varying screening behavior at different ionic concentrations:

$$\varepsilon_0 \nabla \cdot (\varepsilon_{\text{ana}} \nabla \Psi) = 2\,q\,c_0^\infty \frac{\left(a - (a-1)\cosh\left(\frac{q\Psi}{2k_{\text{B}}T}\right)\right)\sinh\left(\frac{q\Psi}{2k_{\text{B}}T}\right)}{\left((1-a) + a\cosh\left(\frac{q\Psi}{2k_{\text{B}}T}\right)\right)^3}. \tag{1.151}$$

c_0^∞ denotes the bulk ion concentration for a 1 : 1 salt, while a describes the closest possible approach between two ions. In the limit $\lim_{a\to 0}$ the Poisson–Boltzmann expression is recovered. One has to mention that this formulation is limited to 1 : 1 electrolytes and therefore can not be applied to arbitrary buffers.

Debye–Hückel Model

The Poisson–Boltzmann equation represents a nonlinear differential equation for the electrostatic potential. Often there is a wish for a formulation which is numerically less demanding or offers quickly an analytical solution. This has been already achieved by Debye and Hückel [43] in 1923, deriving a linearized version of the Poisson–Boltzmann equation. Starting with the corresponding thermodynamical potential, they rigorously deduced the Poisson–Boltzmann model and their equation by Taylor expansion of the exponential terms, neglecting contributions higher than first order. This model is valid only for small potentials and relatively dilute electrolytes:

$$\varepsilon_0 \nabla \cdot (\varepsilon_{Ana} \nabla \Psi(x,y)) = \frac{q^2}{k_B T} (\Psi(x,y) - \Psi_\mu) \sum_{\xi \in S} \xi^2 c_\xi^\infty + \rho_{Space}(x,y). \tag{1.152}$$

From (1.152) two important properties can be gained. Firstly, the Debye length λ_D:

$$\lambda_\mathrm{D} = \sqrt{\frac{k_\mathrm{B} T \varepsilon_0 \varepsilon_\mathrm{Ana}}{q^2 \sum_{\xi \in S} \xi^2 c_\xi^\infty}} \quad \text{or in terms of ionic strength (see (1.155))} \tag{1.153}$$

$$= \sqrt{\frac{k_\mathrm{B} T \varepsilon_0 \varepsilon_\mathrm{Ana}}{2 q^2 I}}. \tag{1.154}$$

The Debye length λ_D states a characteristic length for the electrolytic system. It is the length at which the charge density and also the electric potential of an ion atmosphere reduces to $1/e$.

This approach offers the possibility to estimate the maximal distance of a charged macromolecule to the dielectric-electrolyte interface before its charge is entirely screened by counter ions, or in the case of very large macromolecules (e.g. DNA) to estimate the amount of charge coupled into the semiconductor. The Debye length λ_D influences the double layer thickness and increases the concentration of the counter ions[5] comprising the double layer.

The second parameter has already been introduced in (1.154) and describes the ionic strength of the electrolyte. The ionic strength of an electrolyte is defined as:

$$I(\mathbf{x}) = \frac{1}{2} \sum_{\xi \in S} \xi^2 c_\xi^\infty(\mathbf{x}). \tag{1.155}$$

The ionic strength describes the strength of a solution as a function of ion concentration and ion valence. It is one of the main characteristics of a solution

[5] A counter ion is the ion that accompanies an ionic species in order to gain charge neutrality. For instance, in sodium chloride, the sodium cation is the counter ion of the chlorine anion and vice versa.

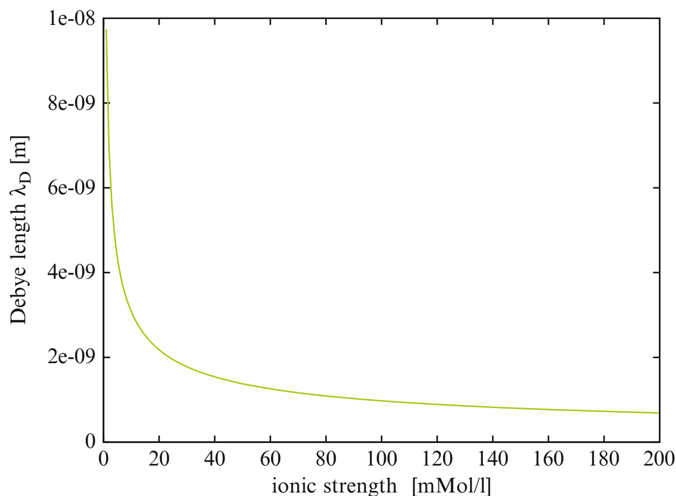

Fig. 1.4 Depicting the relation between the ion concentration for a 1 : 1 electrolytic solution and the Debye length λ_D. Increasing the salt concentration reduces the repulsion between complementary DNA strands and accelerates the hybridization events, but also decreases the Debye length λ_D and thus the device signal

containing dissolved ions and influences many important properties like the dissociation or solubility of different salts, and the double layer thickness (q.v. Sect. 8.2). The strong deviations from ideality which are typically experienced for ionic solutions described via the Debye–Hückel model are handled by the ionic strength. Furthermore, it is related to electrokinetic phenomena, electroacoustic phenomena in colloids and other heterogeneous systems and linked to the electric double layer. The Debye length λ_D is inversely proportional to the square root of the ionic strength (Fig. 1.4). Media with high ionic strength are employed to minimize the changes in the activity quotient of solutes during titration, which are more pronounced at lower concentrations. Natural waters such as seawater have a non-zero ionic strength due to the presence of dissolved salts, which significantly affects their properties.

Buffers and Ionic Strength

Commonly, an experiment is carried out in a so-called *buffer* solution. There are several reasons for this. Enzyme reactions are very sensitive to the local temperature, the local substrate concentration, and also to their *chemical* environment (e.g. pH). Here, the buffer fulfills the function of stabilizing the pH of the solution at a certain point and thus keeping the enzyme activity at its maximum. In the case of DNA hybridization, the ions in the buffer gather around the single DNA strands and screen partially the DNA charge. Therefore, the repulsion between two complementary negatively charged single DNA strands is reduced and they can approach each other close enough to enable the hybridization reaction.

In summary, the use of buffer solutes is a way to control the chemical properties of the environment in which the chemical reaction is conducted. Therefore, buffers are significant ingredients in the description of BioFETs and knowing the ion concentrations and the ionic strength for a buffer is of general importance [26].

7.2 Parameters for the Energy Transport Model and the Six-Moment Transport Model

A big advantage of the Drift–Diffusion Transport model is that, it only contains the carrier mobilities $\mu_{n,p}$. These parameter depend on various quantities such as the applied electric field, temperature, and doping concentration. The mobility can be measured as a function of these quantities and subsequently translated to fit parameters for analytical expressions. Unfortunately, this is not as easy for the higher order transport models. In the following we use μ_0 as abbreviation for $\mu_{n,p}$ and treat electrons and holes with structurally the same formulas. In the case of the Energy Transport model [132], two additional parameters are needed, the energy flux mobility μ_1 and the energy relaxation time τ_1. They can not be directly measured and therefore have either to be modeled [16, 83] or extracted from Monte Carlo simulations [111, 132, 213, 216]. The analytical models require parameters which are adjusted to fit the experimental data of a particular application. The problem is that there is no unique parameter set which fits all requirements.

For the sake of completeness we will start with the analytical description of the parameters. Due to the analog description of electrons and holes, we will restrict ourself to the modeling of electron parameters in the following.

Analytical Models for the Mobility

Two models are frequently used to describe the energy dependence of the mobility. There is the model after Baccarani [15, 16]:

$$\frac{\mu(T_n)}{\mu^{\mathrm{LIS}}} = \frac{T_L}{T_n} \tag{1.156}$$

and the model after Hänsch [83, 84]:

$$\frac{\mu(T_n)}{\mu^{\mathrm{LIS}}} = \left(1 - \frac{3}{2}\frac{\mu^{\mathrm{LIS}}}{\tau_1 v_s^2}\left(\frac{k_{\mathrm{B}} T_{\mathrm{L}}}{q} + \frac{2}{5}\frac{n\mathbf{s}}{\mathbf{j}}\right)\right)^{-1}. \tag{1.157}$$

Assuming homogeneous conditions the energy flux $\mathbf{s}$ is proportional to the particle current [72]:

$$\frac{\mathbf{s}}{\mathbf{j}} = -\frac{5\,k_{\mathrm{B}} T_{\mathrm{n}}}{2q}. \tag{1.158}$$

Substituting (1.158) into (1.157) yields a simplified formulation:

$$\frac{\mu(T_n)}{\mu^{\mathrm{LIS}}} = \left(1 + \frac{3}{2}\frac{\mu^{\mathrm{LIS}} k_B}{q\tau_1 v_s^2}(T_n - T_L)\right)^{-1}. \tag{1.159}$$

As demonstrated in [130, 132], (1.158) reproduces the mobility quite reasonably in regions with increasing electric field, while for decreasing electric field, however, it is better to employ (1.157) cf. [132, 212].

Another approach to model the mobility has been introduced in [213] and is based on the separation of homogeneous and inhomogeneous parts of the mobility. It is proposed to describe the collision term C_p as:

$$n\mathsf{C}_p = \frac{\mathbf{j}}{\mu} = \frac{\mathbf{j}}{\mu^*} + \lambda_p n \nabla \cdot \hat{\mathsf{U}}, \tag{1.160}$$

with μ^* denoting the homogeneous mobility.

The ratio between the energy flux mobility μ_1 and the mobility μ_0 is usually expressed via constant values in the range $0.79 - 1.0\,\mathrm{ps}$ [132, 213]. Tang et al. [213] suggested to model the collision operator $\mathsf{C}_{p\mathscr{E}}$ as:

$$\mathsf{C}_{p\mathscr{E}} = -\frac{q\mathbf{s}}{\mu_1^*} + \lambda_{p\mathscr{E}} \nabla \cdot \hat{\mathsf{R}}, \tag{1.161}$$

which is analogous to (1.160). μ_1^* denotes the homogeneous energy flux mobility. The corresponding expressions for μ_1^* and $\lambda_{p\mathscr{E}}$ are given in [213].

Analytical Models for Relaxation Times

Commonly used values of the energy relaxation time τ_1 for silicon are in the range $0.3 - 0.4\,\mathrm{ps}$, while in general values in the range $0.08 - 0.68\,\mathrm{ps}$ have been employed [98]. The Monte Carlo simulations demonstrate that the constant relaxation time assumption is quite reasonable [213]. However, there have been different energy expressions used. Baccarani et al. [15, 16] proposed for electrons:

$$\tau_1(T_n) = \frac{3}{2}\frac{k_B \mu_0}{q v_s^2}\frac{T_n T_L}{T_n + T_L} + \frac{m^* \mu_0}{2q}\frac{T_n}{T_L}. \tag{1.162}$$

Employing (1.156) and (1.161) together yields the correct homogeneous limit.

Hänsch's approach demands only an energy relaxation time τ_1 independent of the carrier temperature for (1.157) to reproduce the correct homogeneous limit. Defining:

$$\tau_{\mathscr{E}} = \frac{3 k_B \mu_0 T_L}{2 q v_s^2} \tag{1.163}$$

and employing this to (1.157) and (1.159) results in a description equivalent to Baccarani's mobility model in the homogeneous case. A more detailed discussion about the inconsistencies arising, when combining an energy-dependent mobility and energy relaxation time models is found in [170]. On the basis of data from Fischetti [50], Agostinelli proposed a model for the energy relaxation time for silicon [4]:

$$\frac{\tau_1(W)}{1\,\mathrm{ps}} = \begin{cases} 0.172 + 2.656W - 3.448W^2, & \text{for } W \leq 0.4 \\ 0.68 & \text{, for } W > 0.4 \end{cases}, \tag{1.164}$$

with $W = w/(1\,\mathrm{eV})$. Another fit to newer data from Fischetti has been shown by Hasnat et al. [87] and is expressed via:

$$\frac{\tau_1(W)}{1\,\mathrm{ps}} = 0.27 + 0.62W - 0.63W^2 + 0.13W^3 + 0.01W^4, \tag{1.165}$$

exhibiting a maximum of approximately 0.42 ps. The effects of relaxation time and transport models on the performance of silicon bipolar transistors has been studied in [177] in more detail.

Parameter Extraction from Monte Carlo Simulations

For the Six-Moments Transport model the parameter set extends and includes μ_0, μ_1 and μ_2 for the mobilities, H_1, H_2 and H_3 as non-parabolicity factors in the flux equations (1.90), (1.92) and (1.94), and τ_1 and τ_2 relaxation times employed in the balance equations (1.89), (1.91) and (1.93). The parameters are difficult to model due to their dependence on the shape of the distribution function, on the band structure, and on hot carrier effects. Furthermore, the mobilities and relaxation times are scattering controlled. Simple empirical models are often non-satisfactory [71] and in particular hard to compare against Monte Carlo simulations, due to the non-matching results of the transport model with Monte Carlo data in the homogenous case and the questionable extension of these models into the inhomogeneous case.

In order to avoid these problems Grasser et al. [69] extracted all physical parameters as a function of the doping concentration and the average energy from homogenous Monte Carlo simulations. Due to the derivation of all model parameters from bulk Monte Carlo simulations, the resulting transport models are free of fit-parameters and yield a *no knobs to turn* description. Facing far too many parameters is an intrinsic property in many higher order transport models based on analytical models for the mobilities and relaxation times [72].

Figure 1.5 illustrates the non-parabolicity factor dependence on the energy at an electric field of $950\,\mathrm{kV\,cm^{-1}}$. As can be seen the non-parabolicity factors, gained from subband Monte Carlo simulations, head to unity for low energies and thus are consistent with the parabolic band case, where the non-parabolicity factors are equal to one [220].

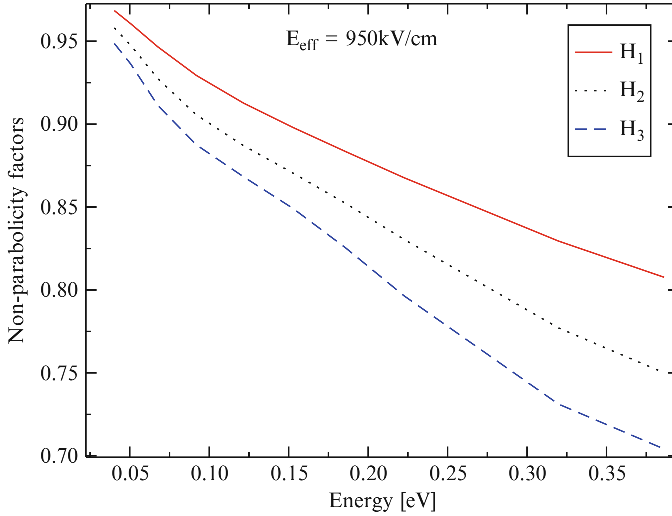

Fig. 1.5 H_1, H_2 and H_3 in relation to the energy at an electric field strength of $950\,\mathrm{kV\,cm^{-1}}$. At low energies, the non-parabolicity factors head to unity. The presented non-parabolicity factors have been extracted from subband Monte Carlo simulations [220]

Parameters for higher-order macroscopic transport models are displayed in Figs. 1.6 and 1.7. The carrier mobility μ_0 and the higher-order mobilities μ_1 and μ_2 are depicted as a function of the electric field $|\mathbf{E}|$ for different doping concentrations N_d (Fig. 1.6, [220]). For electric fields above $100\,\mathrm{kV\,cm^{-1}}$ the values of the mobilities exhibit no dependence on the doping concentration, while for low fields and low doping concentrations, the carrier mobility is very high compared to low fields and high doping concentrations. The energy flux mobility μ_1 and the second-order energy flux mobility μ_2 are smaller than the carrier mobility μ_0 at low doping concentrations and low fields, whereas at low fields and high doping concentrations the values of all mobilities are comparable.

Figure 1.7 depicts the relation between the relaxation times τ_1 and τ_2 for different doping concentrations and as a function of the kinetic carrier energy. Here, at high energies the relaxation times do not depend on the doping concentration and their decrease is caused by the increase of optical phonon scattering. At high doping concentrations N_d, the Monte Carlo simulations predict lower relaxation times in comparison to low N_d.

Avoiding fit-parameters is a crucial point for higher-order models, since their mutual influence is quite complex and the numerical stability of the whole transport model relies on an appropriate choice of these parameters. It has been demonstrated that the model based on the Monte Carlo data outperforms its counterparts based on analytical mobility models [71] substantially, in the quantitative agreement of the simulation results with Monte Carlo device simulations as well as in the numerical stability of the simulation.

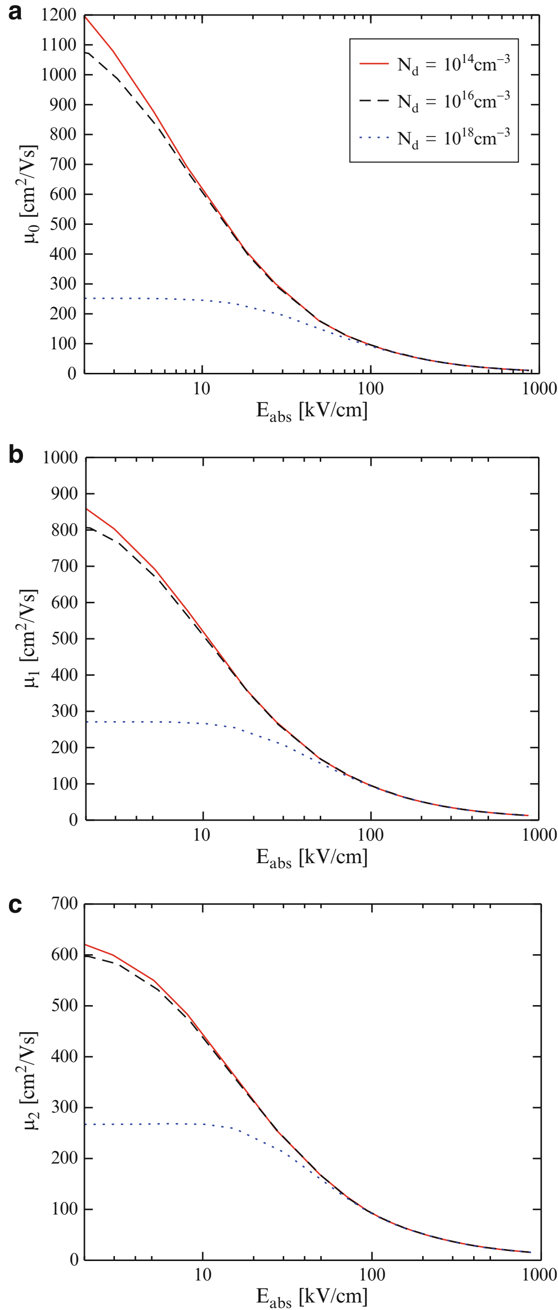

Fig. 1.6 Carrier mobility μ_0, energy flux mobility μ_1, and second-order energy flux mobility μ_2 as a function of driving field for different doping concentrations. While for low fields the values of the mobilities for the low doping case are high in comparison to the high doping case, for fields higher than $100\,\text{kV}\,\text{cm}^{-1}$, the mobilities are independent of the doping concentration

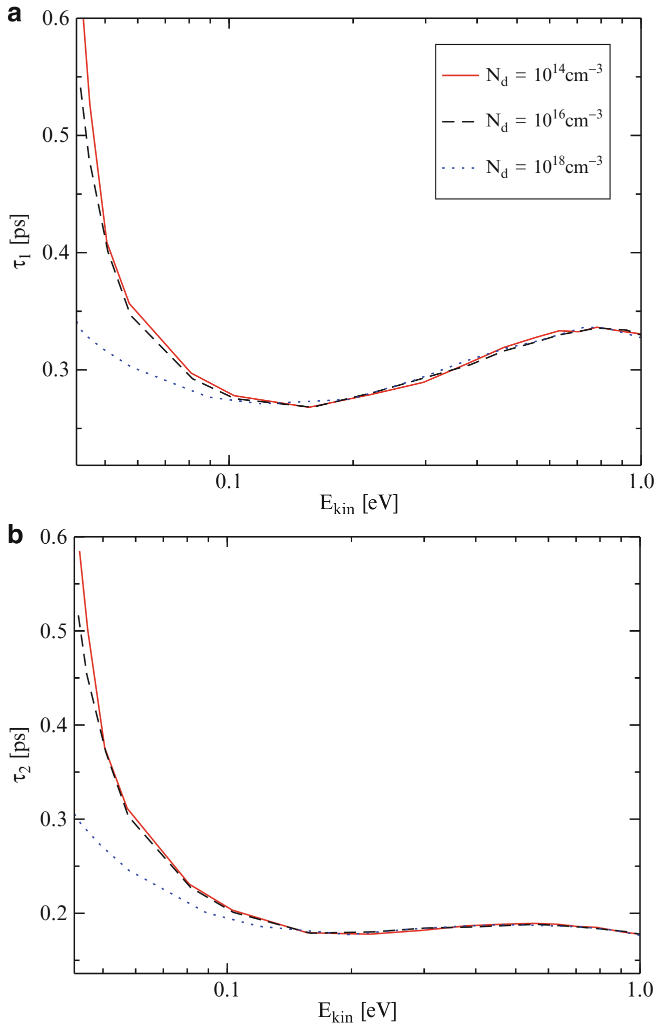

Fig. 1.7 Illustrating the energy-relaxation time τ_1 and the second-order energy relaxation time τ_2 as a function of the kinetic energy for different bulk dopings, extracted from bulk Monte Carlo simulations. At very high energies, the relaxation times decrease due to the increase in optical phonon scattering

7.2.1 Thermoelectric Phenomena

The advent of thermoelectric devices dates back to 1821, when Seebeck found the deviation of a compass needle due to two junctions of different metals at different temperatures [183]. This now called Seebeck effect was caused by the formation of a potential difference due to the temperature gradient. Thirteen years later Peltier

discovered that an electrical current through a junction of two different metals alters the temperature at the junction [162]. Some years later, Lenz found that material combination and current direction determine uniquely, if a junction is cooled or heated [175]. Thomson explained the connection between the Seebeck and the Peltier effect within the framework of thermodynamics [217]. He was also able to predict a third thermoelectric effect, today known as Thomson effect. Altenkirch contributed significantly to the theory of thermoelectric materials by deducing that high quality thermoelectric materials exhibit high Seebeck coefficients and electrical conductivities but show low thermal conductivities [7,8]. Taking these attributes into account one is able to express the figure of merit for thermoelectric materials, which became an important part of the systematic search for novel thermoelectric materials. In the mid of the last century, Ioffe concentrated the research on semiconductor based thermoelectric devices due to the availability of the first artificially manufactured semiconductors and established the basis of modern thermoelectric theory [101, 102]. Due to the improved material properties of semiconductors compared to metals, the efficiency of thermoelectric generators could be raised to about 5%. Intense research efforts lead to the discovery of materials with increased thermoelectric figures of merit appropriate for various temperature ranges. Today the basic structure of thermoelectric generators is a combination of n-type and p-type semiconductor rods, arranged thermally parallel and electrically serial, regardless of the employed materials.

In the sequel the three thermoelectric phenomena are briefly explained in the order of their discovery. These effects are the phenomenological foundations for the description of thermoelectric materials and the functioning of several thermoelectric devices and applications.

Seebeck Effect

The Seebeck effect relates the rise of an electrical voltage due to a temperature gradient. Seebeck not only gave the theoretical interpretation in his pioneering paper [183], but also an overview of several material combinations applicable in thermocouples (cf. Fig. 1.8).

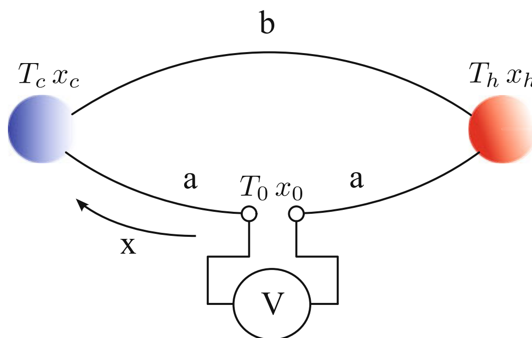

Fig. 1.8 Thermocouple scheme built with two metal rods

A thermocouple consists of two rods of different materials which are soldered together. The soldered points are held at the temperatures T_c and T_h, experiencing a temperature difference ΔT and thus exhibiting a temperature gradient along the rods. From the view point of a device, the given temperature step generates a certain voltage measured at the device contacts:

$$U_{\text{Seebeck}} \propto \Delta T. \tag{1.166}$$

On a microscopic level the Seebeck coefficient is defined via the limit at infinitesimal temperature differences:

$$\alpha(T) = \lim_{\Delta T \to 0} \frac{\Delta U}{\Delta T}. \tag{1.167}$$

The total voltage obtained on a rod is expressed by the path integral along the rod as:

$$U_{\text{Seebeck}} = \varphi_2 - \varphi_1 = \int_{x_1}^{x_2} \partial_x \varphi \, \mathrm{d}x = \int_{x_1}^{x_2} \alpha(T) \, \partial_x T \mathrm{d}x = \int_{T_1}^{T_2} \alpha(T) \, \mathrm{d}T. \tag{1.168}$$

In order to obtain the potential for the entire device one has to evaluate the path integral around both rods. Additionally to the contributions of the two rods, the contact potentials at the soldered points has to be added. However, due to the cancellation of the contact potentials the voltage is given by:

$$U_{\text{Seebeck}} = \int_{T_0}^{T_c} \alpha_a(T) \, \mathrm{d}T + \int_{T_c}^{T_h} \alpha_b(T) \, \mathrm{d}T + \int_{T_h}^{T_0} \alpha_a(T) \, \mathrm{d}T. \tag{1.169}$$

Averaging the temperature dependent Seebeck coefficient along the rods allows to express a combined coefficient for the material couple under given thermal conditions expressed as the difference of the single contribution of each rod:

$$U_{\text{Seebeck}} = (\bar{\alpha}_b - \bar{\alpha}_a) \int_{T_c}^{T_h} \mathrm{d}T = (\bar{\alpha}_b - \bar{\alpha}_a) \, \Delta T. \tag{1.170}$$

Two materials with opposite signs for their Seebeck coefficients must be chosen in order to maximize the gained output voltage. While most metals exhibit Seebeck coefficients in the range of $1-10\,\mu\mathrm{V\,K^{-1}}$, semiconductors offer values of mV and more. There are metals with positive and negative Seebeck coefficients. Depending on the intended application one has to choose an appropriate material combination. For instance, measurement applications do not necessarily need high total Seebeck coefficients, but a linear behavior in the desired temperature range is required. In semiconductors, the Seebeck coefficient is adjusted by appropriately varying the doping. While p-type materials posses positive Seebeck coefficients, n-type materials offer negative ones.

Peltier Effect

The Peltier effect states the phenomenological effect reverse to the Seebeck effect. Driving an electrical current through two connected rods generates a temperature difference between the two soldered points. Therefore, heat is absorbed at one end, while it is released at the other end. In conjunction, a heat flux through the rods is induced. The heat flux at the junctions can be interpreted as energy conservation within the junction and a change of total energy of the carriers when passing the junction.

The heat flux through the rods is governed by the charge current, and the Peltier coefficient and given by:

$$\mathbf{j}^q_{Peltier} = \pi_{ab}\,\mathbf{j}, \tag{1.171}$$

where π_{ab} denotes the Peltier coefficient of a junction, defined by the difference of the contributing materials $\pi_{ab} = \pi_a - \pi_b$. Thus, the direction of the heat flow at a junction is controlled by the choice of materials and the direction of the current flow. Furthermore, the Peltier coefficients are also temperature dependent like the Seebeck coefficients.

The Peltier coefficient and the Seebeck coefficient are not independent of each other. From phenomenological thermodynamics (first Kelvin relation [32]) as well as a systematic approach via the method of moments [224] the following relation is derived:

$$\pi_{ab} = \alpha_{ab}\,T. \tag{1.172}$$

Thomson Effect

Thomson (later Lord Kelvin) predicted and observed the third thermoelectric effect. For a homogeneous conductor exerted to a temperature gradient, the carriers crossing the temperature gradient will experience an energy gain or release depending on their relative direction to the temperature gradient. The energy change of the transiting carriers is absorbed or released as heat, respectively. The total Thomson heat absorbed or released along on rod is defined by:

$$\mathbf{j}^q_{\mathrm{Thomson}} = \int_{T_c}^{T_h} \chi(T)\,\mathbf{j}\,\mathrm{d}T, \tag{1.173}$$

where $\chi(T)$ denotes the temperature dependent Thomson coefficient. The Thomson and Seebeck coefficient are related by the second Kelvin law:

$$\chi = T\,\frac{\mathrm{d}\alpha}{\mathrm{d}T}. \tag{1.174}$$

Thermodynamic Relations

As already mentioned before the three thermoelectric coefficients are related to each other. In the following section, these relations will be discussed within the framework of fundamental thermodynamics [32, 166, 231].

Additionally to the three presented reversible phenomena, two irreversible processes occur in the structure. Firstly, each electrical current causes the dissipation of Joule heat, when passing a material with electrical resistance, and secondly heat is conducted in the device (Fourier's law).

In the following derivations the device illustrated in Fig. 1.8 is regarded as electrically short circuited. Therefore, no electric power is dissipated and no external voltage induced. Furthermore, the cold and the hot contact are connected to thermal reservoirs and energy losses by Joule heating are very small and negligible. The law of total energy conservation in the entire device including the reservoirs for a closed loop and all three thermoelectric effects is given by:

$$\underbrace{\mathbf{j}\,\alpha_{ab}\,\Delta T}_{\text{Seebeck}} = \underbrace{\mathbf{j}\,\pi_{ap}\,(T_h) - \mathbf{j}\,\pi_{ap}\,(T_c)}_{\text{Peltier}} + \underbrace{\mathbf{j}\left(\int_{T_c}^{T_h} \chi_b\,\mathrm{d}T - \int_{T_c}^{T_h} \chi_a\,\mathrm{d}T\right)}_{\text{Thomson}}. \tag{1.175}$$

The Seebeck effect generates the driving force for a current throughout the device. The current induces the Peltier and the Thomson effect. Substituting $T_h - T_c$ by ΔT and dividing (1.175) by $\mathbf{j}$ yields the following expression:

$$\alpha_{ab} = \frac{\pi_{ab}\,(T_c + \Delta T) - \pi_{ab}\,(T_c)}{\Delta T} + \frac{1}{\Delta T}\left(\int_{T_c}^{T_c+\Delta T} \chi_b\,\mathrm{d}T - \int_{T_c}^{T_c+\Delta T} \chi_a\,\mathrm{d}T\right). \tag{1.176}$$

Now, letting ΔT approach zero, the energy relation between the three effects is gained:

$$\alpha_{ab} = \frac{\mathrm{d}\pi_{ab}}{\mathrm{d}T} + \chi_b - \chi_a. \tag{1.177}$$

Neglecting irreversible processes allows to equate the net change of entropy of the entire structure including the reservoirs to zero. Hence, the contributions from all three effects anull:

$$\Delta S = -\mathbf{j}\frac{\pi_{ab}\,(T_c + \Delta T)}{T_c + \Delta T} + \mathbf{j}\frac{\pi_{ab}}{T_c} - \mathbf{j}\int_{T_c}^{T_h} \frac{\chi_b}{T}\,\mathrm{d}T + \mathbf{j}\int_{T_c}^{T_h} \frac{\chi_a}{T}\,\mathrm{d}T = 0. \tag{1.178}$$

Dividing (1.178) by $\mathbf{j}$ and extending the Peltier term by $\Delta t/\Delta T$ gives:

$$\left(-\frac{\pi_{ab}\,(T_c + \Delta T)}{T_c + \Delta T} + \frac{\pi_{ab}\,(T_c)}{T_c}\right)\frac{\Delta T}{\Delta T} = \int_{T_c}^{T_h} \frac{\chi_b}{T}\,\mathrm{d}T - \int_{T_c}^{T_h} \frac{\chi_a}{T}\,\mathrm{d}T. \tag{1.179}$$

In the limit of $\Delta T \rightarrow 0$, the relation between the Peltier and the Seebeck coefficient is gained:

$$-\frac{\mathrm{d}}{\mathrm{d}T}\left(\frac{\pi_{ab}}{T}\right) = \frac{\chi_b - \chi_a}{T}. \tag{1.180}$$

Expanding the derivative in (1.180) results in a more convenient form:

$$\frac{\pi_{ab}}{T} = \frac{\mathrm{d}\pi_{ab}}{\mathrm{d}T} + \chi_b - \chi_a. \tag{1.181}$$

Substituting the right hand side of (1.181) by (1.177) relates the Seebeck and the Peltier effect as observed by Thomson also known as the first Kelvin relation:

$$\frac{\pi_{ab}}{T} = \alpha_{ab}. \tag{1.182}$$

The second Kelvin relation, connecting the Seebeck and the Thomson coefficient, is derived by exchanging the Peltier term in (1.181) with (1.182):

$$T\frac{\mathrm{d}\alpha_{ab}}{\mathrm{d}T} = \chi_a - \chi_b. \tag{1.183}$$

The same results can be derived from Onsager's reciprocal relations [155].

7.2.2 Electrothermal Transport Model

It is important to correctly describe the energy relations in order to gain good results from thermoelectric device simulations. The contributions of the carrier subsystem and the lattice are combined to one heat-flux equation, incorporating rigorous treatment of the coupling mechanisms between the thermal and the electrical description.

Due to the rather low driving forces in electrothermal devices, it is safe to assume that the carrier gas is in local thermal equilibrium with the lattice, and the Electrothermal Transport model can be deduced from the Energy Transport model.

Besides the mandatory Poisson equation, the Electrothermal Transport model requires carrier balance equations and current equations for both carrier types. The energy relations are handled by the heat flow equation which can be deduced via systematic (method of moments) or phenomenological approaches (heuristic inclusion of heat transport).

In the following the Electrothermal Transport model is derived from the moment equations via the Bløtekjær approach (cf. Sect. 5.4). The according energy flux equation (1.81) expressed in terms of the particle flux is given in local thermal equilibrium by:

$$\mathbf{j}_{\nu,u} = \frac{5}{2}\frac{\mu_{\nu,1}}{\mu_{\nu,0}} k_{\mathrm{B}} T \mathbf{j}_{\nu} - \kappa_{\nu} \nabla_{\mathbf{r}} T, \tag{1.184}$$

with κ_ν denoting the thermal conductivity of the carrier subsystem in obedience to Wiedemann–Franz's laws:

$$\kappa_\nu = \frac{5}{2}\frac{k_\mathrm{B}^2}{q}\mu_{\nu,1}\nu T, \tag{1.185}$$

and ν as a placeholder for electrons n or holes p. Equation (1.184) shows the two distinct contributions to the energy flux, heat conduction, and the thermal energy of the moving carrier gas. For non-degenerate semiconductors, the thermal conductivities of the carrier subsystem can be neglected against the lattice contribution [142]. Substituting (1.184) into the energy balance equation (1.80) leads to:

$$\partial_t w + \frac{5}{2}\frac{\mu_{\nu,1}}{\mu_{\nu,0}}k_\mathrm{B}T\nabla\cdot\mathbf{j}_\nu + \frac{5}{2}\frac{\mu_{\nu,1}}{\mu_{\nu,0}}k_\mathrm{B}\mathbf{j}_\nu\cdot\nabla T - \nabla\cdot(\kappa_\nu\nabla T) + \mathrm{s}_\alpha q\mathbf{j}_\nu\cdot\nabla\tilde{\varphi} - G_\nu^{\mathscr{E}} = 0. \tag{1.186}$$

Here, $G_\nu^{\mathscr{E}}$ denotes the net generation rate. After a few rearrangements of (1.186), one is able to gain expressions for physical interpretation. In the first step the gradient of the electrochemical potential Φ_ν is substituted by the current relation [184, 224]:

$$\nabla\Phi_\nu = -\mathrm{s}_\alpha\frac{\mathbf{j}_\nu}{\mu_{\nu,0}\nu} - \mathrm{s}_\alpha\frac{k_\mathrm{B}}{q}\left(\frac{5}{2} - \ln\frac{\nu}{N_{c,\nu}}\right)\nabla T, \tag{1.187}$$

and the Seebeck coefficient is defined by:

$$\alpha_\nu = \mathrm{s}_\alpha\frac{k_\mathrm{B}}{q}\left(\frac{5}{2} - \ln\frac{\nu}{N_{c,\nu}}\right). \tag{1.188}$$

Rewriting (1.186) by insertion of (1.187) and (1.188) the following expression is obtained:

$$\begin{aligned}\partial_t\frac{3}{2}k_\mathrm{B}T - \nabla\cdot(\kappa_\nu\nabla T) + \mathrm{s}_\alpha q\frac{\mu_{\nu,1}}{\mu_{\nu,0}}\nabla\cdot\mathbf{j}_\nu(\alpha_\nu T + \Phi_\nu - \tilde{\varphi}) + \frac{\mu_{\nu,1}}{\mu_{\nu,0}}q\mathrm{s}_\alpha T\mathbf{j}_\nu\cdot\nabla\alpha_\nu \\ - \frac{\mu_{\nu,1}}{\mu_{\nu,0}}q\frac{|\mathbf{j}_\nu|^2}{\mu_{\nu,0}\nu} + \mathrm{s}_\alpha\left(1 - \frac{\mu_{\nu,1}}{\mu_{\nu,0}}\right)q\mathbf{j}_\nu\cdot\nabla\tilde{\varphi} - G_\nu^{\mathscr{E}} = 0.\end{aligned} \tag{1.189}$$

The energy balance equation (1.189) describes the electron and hole subsystem. The lattice contributes via an additional heat-flux term which represents the dominant contribution to heat conduction for most moderately doped semiconductors. This contribution is covered by Fourier's law with a corresponding lattice heat conductivity κ_L. Therefore, the energy balance equations for the three subsystems are given by:

$$\begin{aligned}\frac{3}{2}k_\mathrm{B}\partial_t T = \nabla\cdot(\kappa_n\nabla T) + \frac{\mu_{n,1}}{\mu_{n,0}}q\frac{|\mathbf{j}_n|^2}{\mu_{n,0}n} + \frac{\mu_{n,1}}{\mu_{n,0}}q(\alpha_n T + \Phi_n - \tilde{\varphi})\nabla\cdot\mathbf{j}_n \\ + \frac{\mu_{n,1}}{\mu_{n,0}}qT\mathbf{j}_n\cdot\nabla\alpha_n + \left(1 - \frac{\mu_{n,1}}{\mu_{n,0}}\right)q\mathbf{j}_n\cdot\nabla\tilde{\varphi} + G_n^{\mathscr{E}},\end{aligned} \tag{1.190}$$

$$\frac{3}{2}k_{\mathrm{B}}\partial_t T = \nabla\cdot(\kappa_p\nabla T) + \frac{\mu_{p,1}}{\mu_{p,0}}q\frac{\left|\mathbf{j}_p\right|^2}{\mu_{p,0}p} - \frac{\mu_{p,1}}{\mu_{p,0}}q\left(\alpha_p T + \Phi_n - \tilde{\varphi}\right)\nabla\cdot\mathbf{j}_p$$
$$-\frac{\mu_{p,1}}{\mu_{p,0}}qT\,\mathbf{j}_p\cdot\nabla\alpha_p - \left(1-\frac{\mu_{p,1}}{\mu_{p,0}}\right)q\,\mathbf{j}_p\cdot\nabla\tilde{\varphi} + G_n^{\mathscr{E}}, \tag{1.191}$$

$$c_{\mathrm{L}}\partial_t T = \nabla\cdot(\kappa_{\mathrm{L}}\nabla T). \tag{1.192}$$

The cumulative heat-flow is defined by the sum of the contributions of all three subsystems. Specific heat as well as thermal conductivity are handled as parameters for the entire semiconductor. Thus, the heat-flow equation is given by:

$$c_{\mathrm{tot}}\partial_t T = \nabla\cdot(\kappa_{\mathrm{tot}}\nabla T) + H, \tag{1.193}$$

where the heat source term is expressed as:

$$H = \frac{\mu_{n,1}}{\mu_{n,0}}q\frac{|\mathbf{j}_n|^2}{\mu_{n,0}n} + \frac{\mu_{p,1}}{\mu_{p,0}}q\frac{\left|\mathbf{j}_p\right|^2}{\mu_{p,0}p} + \mathscr{E}_g R + \frac{\mu_{n,1}}{\mu_{n,0}}q\left(\alpha_n T + \Phi_n - \tilde{\varphi}\right)\nabla\cdot\mathbf{j}_n$$
$$-\frac{\mu_{p,1}}{\mu_{p,0}}q\left(\alpha_p T + \Phi_p - \tilde{\varphi}\right)\nabla\cdot\mathbf{j}_p + qT\left(\frac{\mu_{n,1}}{\mu_{n,0}}\mathbf{j}_n\cdot\nabla\alpha_n - \frac{\mu_{p,1}}{\mu_{p,0}}\mathbf{j}_p\cdot\nabla\alpha_p\right)$$
$$+q\left(\left(1-\frac{\mu_{n,1}}{\mu_{n,0}}\right)\mathbf{j}_n - \left(1-\frac{\mu_{p,1}}{\mu_{p,0}}\right)\mathbf{j}_p\right)\nabla\tilde{\varphi}. \tag{1.194}$$

The divergence terms of the electron and hole currents can be substituted by the net recombination rate, for vanishing $\partial_t \nu$ terms in the carrier balance equation in stationary cases. The resulting source term is given by:

$$H = \frac{\mu_{n,1}}{\mu_{n,0}}q\frac{|\mathbf{j}_n|^2}{\mu_{n,0}n} + \frac{\mu_{p,1}}{\mu_{p,0}}q\frac{\left|\mathbf{j}_p\right|^2}{\mu_{p,0}p}$$
$$+q\left(\frac{\mu_{n,1}}{\mu_{n,0}}\left(\alpha_n T + \Phi_n - \tilde{\varphi}\right) - \frac{\mu_{p,1}}{\mu_{p,0}}\left(\alpha_p T + \Phi_p - \tilde{\varphi}\right) - \mathscr{E}_g\right)G$$
$$+qT\left(\frac{\mu_{n,1}}{\mu_{n,0}}\mathbf{j}_n\cdot\nabla\alpha_n - \frac{\mu_{p,1}}{\mu_{p,0}}\mathbf{j}_p\cdot\nabla\alpha_p\right) + q\left(\left(1-\frac{\mu_{n,1}}{\mu_{n,0}}\right)\mathbf{j}_n - \left(1-\frac{\mu_{p,1}}{\mu_{p,0}}\right)\mathbf{j}_p\right)\nabla\tilde{\varphi}. \tag{1.195}$$

A not fully justifiable but frequently used assumption is to set the mobility ratios to unity for electrons and holes [72]. The heat source term simplifies then to:

$$H = q\frac{|\mathbf{j}_n|^2}{\mu_n n} + q\frac{\left|\mathbf{j}_p\right|^2}{\mu_p p} + q\left(T\left(\alpha_n - \alpha_p\right) + \Phi_n - \Phi_p - \mathscr{E}_g\right)G + qT\left(\mathbf{j}_n\cdot\nabla\alpha_n - \mathbf{j}_p\cdot\nabla\alpha_p\right). \tag{1.196}$$

Equation (1.196) contains a contribution from Joule heat losses due to the current flow through the structure, heat transferred to the lattice by the carrier recombination, and Thomson heat.

7.2.3 Seebeck Coefficient

While up to now the Seebeck coefficient has been treated on a phenomenological basis, its inclusion in the semiconductor current equations will be studied in the sequel.

For a non-zero temperature gradient between the two ends of a homogeneous and solid material, a thermoelectric voltage can be measured. The Seebeck coefficient is defined by the ratio of the resulting voltage and the temperature difference. The temperature gradient times the Seebeck coefficient is equal to the negative gradient of the electrochemical potential:

$$-\nabla \Phi_\nu = \alpha_\nu \nabla T. \tag{1.197}$$

This equation is only valid for zero current at open circuit conditions. The current equation (1.187) deduced via the Bløtekjær approach is:

$$\mathbf{j}_\nu = -s_\alpha \mu_{\nu,0} \nu \nabla \Phi_\nu - \mu_{\nu,0} \nu \frac{k_\mathrm{B}}{q} \left(\frac{5}{2} - \ln \frac{\nu}{N_{c,\nu}} \right) \nabla T = 0. \tag{1.198}$$

Since an assumption that the carrier gas is in local equilibrium with the lattice was used, the carrier temperature is equal to the lattice temperature and can be expressed by a single temperature in the current relations:

$$T_\nu = T_\mathrm{L} = T. \tag{1.199}$$

The Seebeck coefficient in (1.197) is identified as:

$$\alpha_\nu = s_\alpha \frac{k_\mathrm{B}}{q} \left(\frac{5}{2} - \ln \frac{\nu}{N_{c,\nu}} \right). \tag{1.200}$$

The resulting current relations for electrons and holes are expressed by:

$$\begin{aligned} \mathbf{j}_n &= \mu_{n,0} n \nabla \Phi_n - \mu_{n,0} n \frac{k_\mathrm{B}}{q} \left(\frac{5}{2} - \ln \frac{n}{N_c} \right) \nabla T \\ &= \mu_{n,0} n \left(\nabla \Phi_n + \alpha_n \nabla T \right), \end{aligned} \tag{1.201}$$

$$\begin{aligned} \mathbf{j}_p &= -\mu_{p,0} p \nabla \Phi_p - \mu_{p,0} p \frac{k_\mathrm{B}}{q} \left(\frac{5}{2} - \ln \frac{p}{N_v} \right) \nabla T \\ &= -\mu_{p,0} p \left(\nabla \Phi_p + \alpha_p \nabla T \right), \end{aligned} \tag{1.202}$$

and the corresponding Seebeck coefficients are defined as:

$$\alpha_n = -\frac{k_{\mathrm{B}}}{q}\left(\frac{5}{2} - \ln\frac{n}{N_c}\right), \tag{1.203}$$

$$\alpha_p = \frac{k_{\mathrm{B}}}{q}\left(\frac{5}{2} - \ln\frac{p}{N_v}\right). \tag{1.204}$$

The opposing signs of the Seebeck coefficients in (1.203) and (1.204) are the reason for the basic thermoelectric device behavior, exhibiting two legs with p and n doping, respectively. These devices are commonly built electrically in serial but thermally in parallel, thus yielding a constructive interference of the contributions from both legs (see Fig. 1.20).

Several physical mechanisms causing an additional driving force for carriers by a temperature gradient are incorporated in the Seebeck coefficient model. In the following the expressions (1.203) and (1.204) are reformulated to depend on energy levels in the semiconductor. The carrier concentrations are expressed assuming Boltzmann statistics:

$$n = N_c \exp\left(\frac{\mathscr{E}_f - \mathscr{E}_c}{k_{\mathrm{B}}T}\right), \tag{1.205}$$

$$p = N_v \exp\left(\frac{\mathscr{E}_v - \mathscr{E}_f}{k_{\mathrm{B}}T}\right). \tag{1.206}$$

and substituted into (1.203) and (1.204):

$$\alpha_n = -\frac{k_{\mathrm{B}}}{q}\left(\frac{5}{2} - \frac{\mathscr{E}_f - \mathscr{E}_c}{k_{\mathrm{B}}T}\right), \tag{1.207}$$

$$\alpha_p = \frac{k_{\mathrm{B}}}{q}\left(\frac{5}{2} - \frac{\mathscr{E}_v - \mathscr{E}_f}{k_{\mathrm{B}}T}\right). \tag{1.208}$$

The temperature dependence of the Fermi level itself raises a gradient along the thermoelectric device and thus a carriers driving force. Additionally the positions of the band edges are temperature dependent and they therefore contribute to the driving force in the semiconductor. The previously assumed Boltzmann statistics is only valid for low doping concentrations, while at high doping concentrations the Fermi–Dirac statistics has to be taken into account. The phonon system, which acts as scattering centers for the carriers, has been assumed in local thermal equilibrium. This is not valid in electrothermal devices, due to the strong temperature gradients and the phonon movement through the structure. Caused by the phonons transiting from the hot side to the cold side of the device, the carriers gain additional momentum, which is also known as *phonon-drag* effect [57, 58, 144, 226] and can be modeled by adding an extra driving force for the carriers in the expression for the Seebeck coefficients [90–92]. A theoretical approach incorporating the phonon-drag effect has been presented in [233]. For silicon the phonon-drag effect is significant in the temperature range from 10 to 500 K [92].

The correction terms ζ_n and ζ_p are introduced into (1.209) and (1.210) in order to account for the deviation from Boltzmann statistics in the degenerate case and the phonon-drag effect:

$$\alpha_n = -\frac{k_\mathrm{B}}{q}\left(\frac{5}{2} - \ln\frac{n}{N_c} + \zeta_n\right), \tag{1.209}$$

$$\alpha_p = \frac{k_\mathrm{B}}{q}\left(\frac{5}{2} - \ln\frac{p}{N_v} + \zeta_p\right). \tag{1.210}$$

7.3 Comparing the Six-Moments Transport Model with Spherical Harmonics Expansion

Spherical Harmonics Expansion (SHE) is a numerical method for the solution of the Boltzmann Transport equation. By expanding the distribution function $f(\mathbf{r},\mathbf{k},t)$ in the $\mathbf{k}$-space into spherical harmonics functions $Y_{lm}(\theta,\Phi)$ one can obtain an approximate solution of the Boltzmann Transport equation [212]. The SHE procedure is able to reproduce the results calculated by Monte Carlo methods quite well while at the same time exhibiting less computational costs. Spherical harmonics functions are defined via [2, 129]:

$$Y_{lm}(\theta,\Phi) = \sqrt{\frac{2l+1}{4\pi}\,\frac{(l-m)!}{(l+m)!}}\,P_l^m(\cos(\theta))\,e^{\mathrm{i}m\Phi}, \tag{1.211}$$

with $P_l^m(\cos(\theta))$ commonly known as Legendre polynomials and the indices l and m defined in the ranges $l \in [0,\infty)$ and $m \in [-l,l]$, respectively. The spherical harmonics functions are orthogonal [113]:

$$\int_0^{\pi}\int_0^{2\pi} \mathrm{d}\Omega\, Y_{lm}(\theta,\Phi)\, Y^*_{l'm'}(\theta,\Phi) = \delta_{ll'}\,\delta_{mm'}. \tag{1.212}$$

The asterisk in the term $Y^*_{l'm'}$ in (1.212) represents the complex conjugate of $Y_{l'm'}$, while $\mathrm{d}\Omega$ is defined by $\mathrm{d}\Omega = \sin(\theta)\,\mathrm{d}\theta\,\mathrm{d}\Phi$. In order to give an impression of the structure of theses functions Y_{00}, Y_{10}, Y_{11} and Y_{20} are given below:

$$Y_{00} = \sqrt{\frac{1}{4\pi}}, \qquad Y_{10} = -\sqrt{\tfrac{3}{8\pi}}\,\sin(\theta)e^{\mathrm{i}m\Phi}, \qquad Y_{11} = \sqrt{\frac{3}{4\pi}}\,\cos(\theta)$$

$$\text{and} \quad Y_{20} = \sqrt{\tfrac{5}{16\pi}}\left(3\cos^2(\theta) - 1\right). \tag{1.213}$$

Under the prerequisite of rotational symmetry along the Φ direction, the spherical harmonics functions reduce to the associated Legendre polynomials.

The distribution function can be expanded into spherical harmonics functions:

$$f(r,k) = \sum_{l=0}^{\infty} \sum_{m=-l}^{l} f_{lm}(r,k) Y_{lm}(\theta, \Phi). \tag{1.214}$$

The coefficients $f_{lm}(r,k)$ are defined as:

$$f_{lm}(r,k) = \int_0^{\pi} \int_0^{2\pi} \mathrm{d}\Omega f(\theta,\Phi) Y^{*}_{l'm'}(\theta,\Phi). \tag{1.215}$$

Thus, the fluxes in the three-dimensional case (q.v. (1.55)) are given by:

$$n\mathbf{V}_i = \sum_{l=0}^{\infty} \sum_{m=-l}^{l} \int_0^{\pi} \int_0^{2\pi} \mathrm{d}\Omega \mathbf{v}\mathscr{E}^i f_{lm}(\theta,\Phi) Y_{lm}(\theta,\Phi). \tag{1.216}$$

In the next step the SHE method is applied to the stationary Boltzmann transport equation. In order to simplify the following derivation, we will restrict to the transport direction of the carriers and assume it to be along the z-axis in conjunction with parabolic bands. Thus, (1.214) reduces to:

$$f(z,k) = \sum_{l=0}^{N} f_l(z,k) P_l(\cos(\theta)), \tag{1.217}$$

where θ denotes the direction of the electric field and $P_l(\cos(\theta))$ describe the Legendre polynomials. Before substituting the distribution function via spherical harmonics functions, the **k**-space is transformed into the $\mathscr{E}$-space, offering advantages such as an isotropic distribution function on energy surfaces in equilibrium [113]. By expanding the Boltzmann transport equation via (1.217), one yields the SHE [169, 221]. The two lowest order expansions are defined as:

$$l = 0 \longrightarrow \quad \partial_z f_1 - qE\left(\partial_{\mathscr{E}} f_1 + \Gamma_B f_1\right) = \frac{1}{v}\left(\partial_t f_0\right)_{\mathrm{coll}}, \tag{1.218}$$

$$l = 1 \longrightarrow \quad \partial_z f_0 - 2\partial_z f_2 - qE\left(\partial_{\mathscr{E}} f_0 + 2\partial_{\mathscr{E}} f_2 + 3\Gamma_B f_2\right) = \frac{1}{v}\left(\partial_t f_1\right)_{\mathrm{coll}}. \tag{1.219}$$

In the limit $N \to \infty$ the resulting description is an exact solution of the Boltzmann transport equation. Vasicek [220] demonstrated for a velocity profile of an n^+nn^+ structure, that already for considering the first nine Legendre polynomials there is a good agreement between the SHE results and data from Monte Carlo simulations.

In the next step, the relation between the SHE and the macroscopic transport models is derived (e.g. Drift–Diffusion Transport model). Presuming a homogeneous, stationary system under an externally applied electric field **E**, parabolic

bands, and the validity of the diffusion approximation, leads to a description of the Boltzmann transport equation with a macroscopic relaxation time approximation as follows:

$$-q\mathbf{E}\nabla_{\mathbf{p}}f = -\frac{f - f_0}{\tau_0}. \tag{1.220}$$

The distribution function f can be split into a symmetric part f_s and an anti-symmetric part f_a, which incorporates the non-equilibrium conditions. The diffusion assumption [67] states that:

$$f_s \gg f_a, \tag{1.221}$$

which demands that the system is not far from equilibrium and hence (1.220) can be exploited to deduce an expression for the anti-symmetric part f_a [138]:

$$f_a = q\tau_0\mathbf{E}\nabla_{\mathbf{p}}f_0 = \frac{q\tau_0 f_0}{k_{\mathrm{B}}T_{\mathrm{L}}}\mathbf{E}\,\mathbf{v} = \frac{q\tau_0\hbar}{k_{\mathrm{B}}T_{\mathrm{L}}m^*}f_0\,|\mathbf{E}|\,|\mathbf{k}|\,P_1\left(\cos(\theta)\right). \tag{1.222}$$

By inserting (1.222) into (1.216) one obtains the drift term of the Drift–Diffusion Transport model. Hence, just considering the first Legendre polynomial of the SHE for low-fields yields the same results as the Drift–Diffusion Transport model.

Therefore, the SHE is an appealing alternative to the solution of the Boltzmann transport equation via the Monte Carlo method and can be used as a reference solution for the previously derived three-dimensional higher-order macroscopic transport models.

As an example, Figs. 1.9 and 1.10 compare the Drift–Diffusion Transport model, the Energy Transport model and the Six-Moments Transport model for different channel lengths against results obtained by SHE as a reference and the corresponding relative error of the applied transport model [220]. As expected at a channel length of 1,000 nm all transport models yield the same results in conjunction with a small relative error of ∼1% (Fig. 1.10). For a channel length of 250 nm the errors of the Energy Transport model and the Six-Moments Transport model stay within reasonable 2.5%, while the Drift–Diffusion Transport model starts with ever increasing errors and reaches a relative error of ∼16% at a channel length of 100 nm. Below 250 nm the error of the Energy Transport model continuously increases, while the Six-Moments Transport model stays close to the SHE reference.

Simulating short channel devices with the Drift–Diffusion Transport model gives only poor results, as expected. However, for devices exhibiting a channel length of 1 μm, the Drift–Diffusion Transport model, the Energy Transport model, the Six-Moments Transport model, and the SHE model yield the same current value with a relative accuracy of 1%. The reason for the failure of the Drift–Diffusion Transport model lies in its closure assumption. By setting the charge carriers' temperature equal to the lattice temperature, the corresponding distribution function constantly underestimates the amount of available charge carriers and thus yields too small currents. On the other hand, the Energy Transport model assumes a heated Maxwellian distribution function, which is not valid in devices with channel lengths below ∼250 nm.

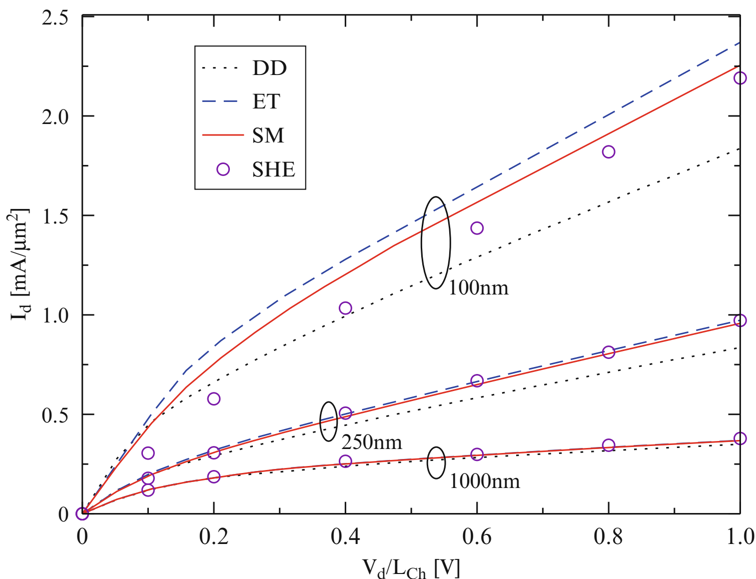

Fig. 1.9 Output currents for different $n^+ - n - n^+$ structures calculated with Drift–Diffusion Transport model, the Energy Transport model, and the Six-Moments Transport model. The SHE results are employed as a reference. For 1,000 nm, all models predict the same current, while the Drift–Diffusion Transport model underestimates the current for a channel length of 100 nm

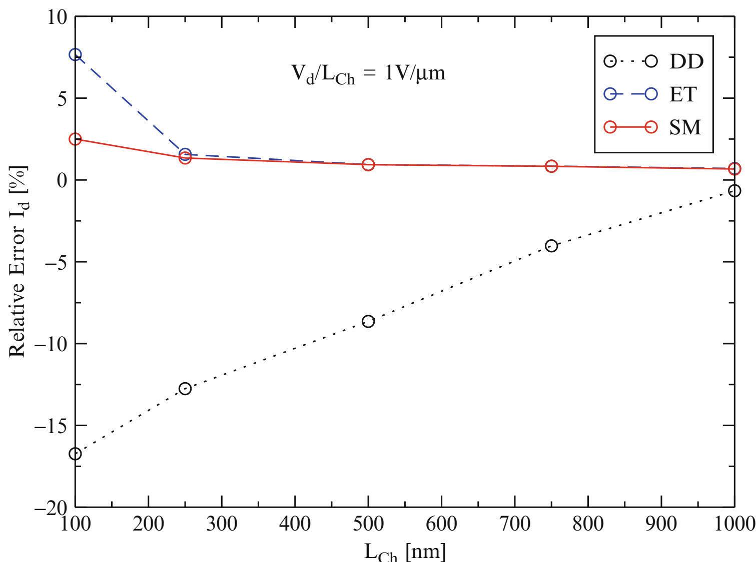

Fig. 1.10 Illustrating the relative error of the current calculated with the Drift–Diffusion Transport model, Energy Transport model, and the Six-Moments Transport model as a function of the channel length at a voltage of 1 V. While the Energy Transport model and the Six-Moments Transport model is below 7.5%, the Drift–Diffusion Transport model heads to 16% at a channel length of 100 nm

8 Applications

Despite the nowadays readily available nanometer technology (the semiconductor industry is entering the 22 nm node [103]), there is still plenty of room for the application of classical transport models. In the subsequent section three examples of up to date devices covered by classical device simulation will be given. These examples treat solar cells, BioFETs, and thermovoltaic elements.

8.1 Solar Cells

The French physicist Becquerel was the first to recognize the photovoltaic effect in 1839, but it took until 1883 to build the first solar cell, which was realized by semiconducting selenium coated with an extremely thin layer of gold to create the junction. This device possessed a poor conversion efficiency of about 1%. After Stoletow [205–207], who built the first solar cell based on the outer photoelectric effect, and Einstein explaining the photoelectric effect in 1905, Ohl patented the modern junction semiconductor solar cell in 1946 [154].

The present research in the field of photovoltaics can be divided into three main topics: reducing the cost of state of the art solar cells and/or increase their efficiency, so that they can compete with other energy sources; developing new solar cells with new technologies and new solar cell architectural designs; and advancing materials serving as light absorbers and charge carriers.

8.1.1 Working Principle of Solar Cells

Solar cells are similar to photo diodes [63] (Fig. 1.11). The distinction between both applications is that solar cells are designed to convert photons into electric power and not just detect photons like the photo diode. Therefore, in order to increase the amount of photons penetrating the solar cell and generating electron–hole pairs, the area accessible to light must be as large as possible and the coupling of the photons in the cell efficient. Under optimum conditions a photon is able to enter the solar cell and to generate an electron–hole pair. The electron and the hole start to diffuse and reach the space charge region of the pn-diode. There, the electron is pushed into the n-doped region and the hole moves to the p-doped zone and later on into the p+-doped zone, due to the built-in electric field created by the space charges. Furthermore photons generate electron–hole pairs and the electrons accumulate at the front, while the holes aggregate at the back contacts, thus generating an electric potential difference.

Consequently, different demands arise in order to optimize the conversion efficiency of solar cell. One way to enhance the yield from the generated electron–hole pairs is to design the depletion zone as large as possible and keep at the same time the average diffusion length of electrons and holes at a high level. Thus the electrons

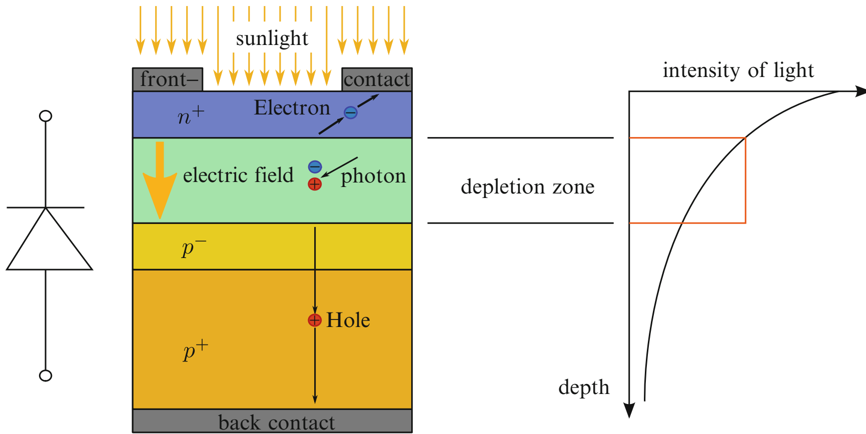

Fig. 1.11 Illustration of the working principle of a solar cell

and holes, which do not originate in the depletion region, increase their chance to reach the junction region and become swept to the corresponding side of the pn-diode. Furthermore, the number of photons exponentially decreases with increasing depth and thus it is beneficial to situate the depletion layer close to the surface. This is commonly achieved by a thin highly n-doped layer at the surface and a thick low p-doped substrate. If electrons are generated in the p-doped layer they are able to get to the back contact and recombine there. This effect is suppressed by an additional highly doped p-layer (also called p+-layer) at the back contact. The p+-layer induces a so-called *back surface field* between the p- and the p+-region and reflects electrons on their way to the back contact giving the electrons a second chance to reach the depletion layer. On the other hand also holes arriving at the surface of the front side are able to recombine with surface trap states, reducing the number of holes on the back side of the cell. This is the reason for an extra antireflection coating which decreases the reflectivity of the surface and also saturates surface traps, but may require an extra passivation step [1]. Another way of coupling light more efficiently into the solar cell is to texture the surface [63,73]. The front contacts represent a trade off between minimizing the energy losses in the fingers and busbars of the contact and maximizing the accessible area for the incoming photons. Commonly, this is realized by two thick busbars connected to many thin fingers perpendicular (see Fig. 1.12).

Despite many efforts to introduce alternative solar cell designs, the results can not compete with established solar cells either in efficiency or over all costs [78]. For instance, nanostructures exhibit lower thermal conductivities than their bulk materials, due to increased acoustic phonon scattering, which causes issues related to heat removal and reliability [118,135,192] (unlike in thermovoltaic applications where it is actually beneficial. cf. Sect. 8.3). Therefore, wafer based silicon (e.g. single crystal, polycrystalline and multicrystalline) solar cells and thin film solar cells manufactured with amorphous silicon, $CdTe$, $CuInGaSe_2$, and $III–V$ semiconductors rule the photovoltaic manufacturing [193]. Shockley and Queisser estimated the thermodynamic limit of maximum efficiency for a pn-junction silicon solar cell at 300 K

Fig. 1.12 Example for a monocrystalline solar cell exhibiting the commonly employed contact pattern

and *AM* 1.5 illumination around 30% [188]. Photon energies higher than the energy band gap are converted into heat. Heat loss is the major effect for efficiency degradation in silicon solar cells. Therefore, major efforts are being put on exploiting hot carriers created by absorbing photons with an energy higher than the energy band gap and generating higher output currents or voltages, and introducing energy states within the band gap to trap carriers originating from photons smaller than the band gap energy [78].

The class of high-efficiency solar cells is characterized by the ability to generate more electric power per incident solar power unit. The industry is interested in the most cost efficient technologies in the sense of cost per generated Watt. The two major solutions to reduce costs of photovoltaic electricity are enhancement of cell efficiency and reduction of the costs per unit area. Thus, it is highly desirable that the efficiency of the solar cell is increased and the total cost per kilowatt-hour is reduced at the same time.

8.1.2 Multiple Junction Solar Cells

Multiple junction photovoltaic cells consist of many layers of epitaxially deposited films. The band gap of each layer is adjusted by a different alloy composition of *III–V* semiconductors, enabling every layer to absorb a specific band of the solar spectrum. The optimization of the respective band gaps of the various junctions is aggravated by the constraint of matching lattice constants for all layers. Beginning with the highest band gap material on top, all layers are optically in series. The first junction receives all of the incoming spectrum and photons with energies higher than the first band gap are absorbed in the first layer. Photons with energies below the first band gap travel to the next layer and are subsequently absorbed.

Currently available commercial cells are electrically connected in series. Due to the series connection, the generated current through each junction must be equal. Therefore, current match for each junction is an important design criterion for these devices.

For multiple junction solar cells the highest reported efficiencies are claimed to be 42.8, 41.1, and 40.8% from the university of Delaware [96], the Fraunhofer institute for solar energy systems [52], and the US national renewable energy research facility (NREL) [152], respectively.

Various multiple junction solar cells and their properties have been studied by simulations [6, 114, 218, 222].

8.1.3 Thin-Film Solar Cells

There are several thin-film technologies currently in development. The goal is to reduce the amount of light absorbing material required for producing a solar cell. This decreases the processing cost compared to using bulk materials, but at the same time also reduces the energy conversion efficiency to about 7–10% [75]. However, many multi-layer thin-film cells exhibit efficiencies above those fabricated on bulk silicon wafers. Their advantage, in addition to bulk silicon, lies in lower costs, flexibility, lighter weights, and ease of integration.

An efficiency of 19.9% for solar cells based on copper indium gallium selenide thin films (CIGS) was achieved by the NREL [153]. The CIGS films were grown by physical vapor deposition via a three-stage co-evaporation process. During this process indium, gallium and selenium are evaporated and afterwards copper and *Se* co-evaporated followed by *In*, *Ga* and *Se* evaporation at the end.

Thin film solar products have about 14% marketshare, while the other 86% are held by crystalline silicon [107]. The biggest amount of commercially produced thin-film solar cells is based on *CdTe* with a typical efficiency of 11%.

Pieters et al. introduced a new version of their simulation tool, suitable for thin-film solar cells [163], Song et al. numerically studied CIGS tandem solar cells [201], Malm et al. studied CIGS thin-film solar cells with the aid of the finite element method [139], and Iwata et al. studied the influence of solar cell thickness and surface roughness on the conversion efficiency [104].

8.1.4 Crystalline Silicon

Crystalline silicon is currently the material of choice for solar cells, also known as *solar grade silicon*. Bulk silicon can be further distinguished into multiple categories according to crystallinity and crystal size in the resulting ingot, ribbon, or wafer. Monocrystalline silicon is frequently produced by the Czochralski process which tends to be expensive. Poly- or multicrystalline silicon, which is cheaper in production, but also exhibits smaller efficiency, and ribbon silicon [120], which is a subtype of multicrystalline silicon formed by drawing flat thin films from molten silicon, which further reduces production costs and silicon waste, but at the same time causes efficiencies smaller than polysilicon.

Monocrystalline silicon cells yield the highest efficiencies in silicon. The highest commercially available efficiency (22%) is manufactured by SunPower by utilizing

expensive, high quality silicon wafers. An efficiency of 25% has been reported on monocrystalline silicon under laboratory conditions [219]. Crystalline silicon devices achieve an energy payback period of 1–6 years depending on cell type and environmental conditions [54, 168], and they are heading to the theoretical limiting efficiency of 30% [74, 188].

Klusak et al. [123] presented a modeling and optimization study of industrial n-type high-efficiency back-contact back-junction silicon solar cells. Ghargi et al. [59] numerically studied spherical silicon solar cells as a cost effective alternative to planar silicon solar cells. Campa et al. [33] found an increase up to 45% in current density for an optimized structure with periodic sinusoidal textured interfaces in comparison to that of the cell with flat interfaces. Tasaki et al. [215] investigated the influence of interface states on high performance amorphous silicon solar cells.

From the simulation point of view, feasible photovoltaic devices posses areas from several cm^2 to several hundred cm^2 and thicknesses around $\sim 100-400\,\mu m$ for standard cells and several μm for thin film cells. Therefore, the simulation of these devices is well covered by the Drift–Diffusion Transport model and, if necessary (e.g. inhomogeneous illumination of the surface and other effects causing inhomogeneous heating of the cell) by the Energy Transport model.

8.2 Biologically Sensitive Field-Effect Transistors

Today's technology for detecting pathogens, antigen-antibody complexes, and tumor markers is a timeconsuming, complex and expensive task [164, 186]. For instance, a typically workflow to detect, e.g., a certain deoxyribonucleic acid (DNA) molecule involves several process steps. First, one has to increase the number of DNA samples either by polymerase chain reaction (PCR) or reverse transcription (RT), followed by a subsequent process step which marks the DNA with a so-called label. The label enables the sensing of the DNA via radiation or light. This sample is afterwards applied to a microarray. Which consists of an array of spots. Each of the spots is prepared differently and thus offers the detection of a defined molecule. When the reaction took place, the array is read by a costly microarray reader.

At this point the introduction of a field-effect transistor which replaces the optical sensing mechanism by an electrical signal detection, offers several advantages. First, there is no need for the expensive readout device anymore. Furthermore, utilization of field-effect transistors allows the integration of analyzing and amplifying circuits on the same chip and, hence, enables a further cost reduction due to cheaper equipment. The outstanding development of semiconductor process technology allows mass production for this kind of devices in combination with a reduction of the price per piece.

Various reaction pairs are accessible and extensively studied for detecting DNA [53, 56, 80], cancer markers [238], proteins like biotin-streptavidin [42, 79, 99, 203], albumin [160], and transferrin [62], representing only a small sample to

illustrate the diversity of the investigated device types and materials. It also shows, that there are many high-potential researches on BioFETs, which is still in its initial phase.

The concept of a BioFET is extremely versatile. Nearly all molecules posses a charge, when they are dissolved in a solute. This charge can be exploited by binding it on the surface of a BioFET, thus enabling its detection.

Among the possibility of exploiting BioFETs for DNA sequencing in a lab, these devices could enable a family doctor to screen for diseases on his own and decide faster and with less effort, which treatment is best for a patient, supported by the integrated analyzing and amplifying circuits in conjunction with the shrinking device size and easier handling. Furthermore, the amount of multi-resistance germs could be reduced by the consideration of a patients genetic profile, and a choice at deciding for a certain treatment or medication could be optimized, yielding the best possible results.

The integration of a BioFET into a chip environment is a manageable task. Either by putting a microfluidic channel above the functionalized gate of the BioFET or by isolating the surrounding areas by a thick oxide or polymere, the chip can be transformed into a mini-laboratory also known as lab on chip. This kind of systems improve the control over environmental parameters like local pH or detects the amount of a special protein, and facilitates local measurements (e.g. how a cell reacts to certain stimuli), thus offering a complete lab on chip. However, even though great advances have been made, far more research is needed to overcome the many obstacles.

The Working Principle of a BioFET

A BioFET consists of several parts: a reference electrode (analog to the gate contact for a MOSFET), the analyte, a biofunctionalized surface layer, a dielectric layer, and a semiconductor transducer (as depicted in Fig. 1.13). The semiconductor transducer is implemented as a conventional field-effect transistor. The dielectric is commonly an oxide (e.g. SiO_2) and serves two purposes: the first is to electrically isolate the channel of the field-effect transistor from the liquid and the second is to couple the surface layer charge to the channel electrostatically. The biofunctionalized surface layer exhibits immobilized biomolecule receptors able to bind a certain molecule. The sample molecules are dissolved in a solution which is also known as analyte. The sensitivity of the device is adjusted by the reference electrode (the optimum sensitivity lies around moderate inversion [44]).

If the desired molecules bind to the receptors, the surface charge density changes. This modifies the potential in the semiconductor and thus the conductivity in the channel of the field-effect transducer. The scale of the chemical reaction between sample and receptor molecules lies in the Angstrom regime, while the BioFET size is in the micrometer regime. Hence, it is significant to employ a proper multiscale mathematical description of the solution/semiconductor interface.

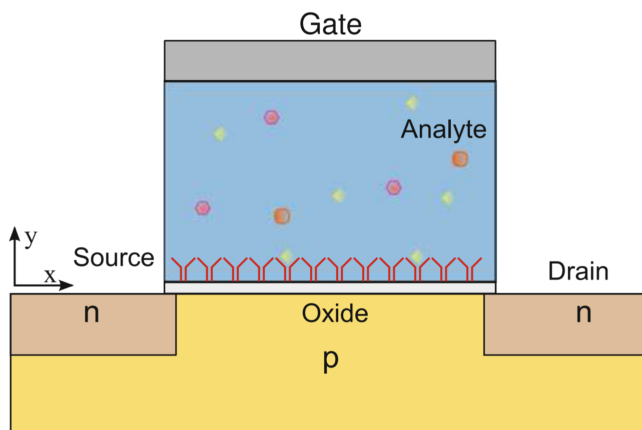

Fig. 1.13 When a charged sample molecule reaches a matching receptor at the biofunctionalized surface, it binds to it. This event alters the surface potential and also the potential distribution in the semiconductor, which results in a resistance change of the field-effect transistor's channel

Modeling Electrolytic Interfaces

Chemical and biological experiments are commonly carried out in ionic solutions [227]. The non-vanishing dipole moment of polar solution molecules (e.g. water) enables the reduction of the electric field between bound ions and, hence, to break up initially strong ionic bonds leading to more chemically active reactants. *NaCl* and *KCl* are common salts for buffer solutions and exhibit valences for their anions and cations equal in absolute value (so-called 1 : 1 solution/salt). Without external forces the charges are homogeneously distributed across the electrolyte and each ion is surrounded by an aggregate of water molecules. The water shell around an ion influences the relative dielectric constant around the ion and reduces the effect of electric fields stemming from other ions. Therefore, ions can freely move in the solvent and facilitate the conduction of an electrical current.

Insulator Surface Charge (Double Layer)

Charges gather at the electrode and in the surface area of the electrolyte, either due to an externally applied field or a difference of the chemical potentials between the electrode and the electrolyte. In the electrode (assuming a metal) the majority of charge carriers resides on the electrodes surface due to their mutual repulsion. In the electrolyte, the dissolved ions of opposing charge will be attracted by the electrodes surface charge. Unlike the electrons in the electrode, the ions exhibit a water shell and therefore a larger radius. Thus, a single layer of ions is not able to compensate the surface charge of the electrode and a diffusive layer of ions at the

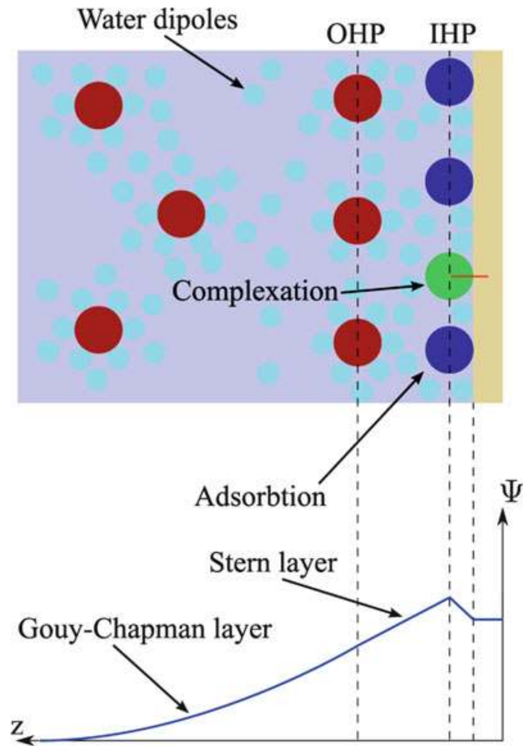

Fig. 1.14 The different contributions to the potential profile are: the inner Helmholtz plane (IHP) due to (non-) specific adsorption (caused by partial release of the solvation shell and therefore closer distance to the interface, *blue circles*), surface complexation, caused by the high affinity of attracting counter ions (*green circle*), the outer Helmholtz plane (OHP), and end of the Stern layer (zone without counter ions possessing their whole water shell, *red circles* with small *blue circles*) and the Gouy–Chapman layer [186]

electrodes surface will rise. In this *double layer* a potential drop will occur which has to obey the Poisson equation. Combining the Poisson equation and assuming thermal equilibrium of the ions with their environment the Poisson–Boltzmann equation is deduced. The diffusive layer is also known as Gouy–Chapman layer or electric double layer (depicted in Fig. 1.14).

Stern Modification

The potential distribution in the vicinity of the electrode–electrolyte interface is calculated by the Poisson–Boltzmann equation. Nevertheless, experimental data exhibit deviations from the predicted values for the double layer charge and capacitance [45]. It was shown that the Gouy–Chapman model overestimates the interface charge and the capacitance for high-concentration electrolytes. Stern was the first to recognize that the ions in the electrolyte posses a certain dimension and can not approach the electrode surface closer than their ionic radius. This led to the introduction of the outer Helmholtz plane (OHP) [61], taking care of the closest possible distance. The water molecules aggregated around the ion are included in

this distance. The release of the aqueous shell of the ion would require an extensive amount of energy and thus a zone close to the electrode surface exists, which is depleted of ionic charges giving rise to an additional contribution to the total capacitance. This Stern capacitance has a typical value of $\sim 20\,\mu\mathrm{F\,cm^{-2}}$. However, there are further contributions to the potential profile. Usually these effects are small and therefore negligible. Some of the effects are summarized in Fig. 1.14:

- Specific adsorption of ions on the surface: If ions (partially) release their solvation shell, they are able to move closer to the interface than the OHP. The new emerging radius of closest approach is called inner Helmholtz plane (IHP). The resulting model treating IHP and OHP, is called Gouy–Chapman–Stern–Graham model [186].
- Non-specific adsorption: Instead of releasing water molecules from the solvation shell, they are adsorbed on the surface due to distant coulombic attraction.
- Polarization of solvent: Commonly, the effects caused by the electric field weakening through the dipole moment of water is covered via adjustment of the relative permittivity. In the case of bulk applications this works well, while in the neighborhood of a surface many water molecules are not able to polarize with the electric field and the effective relative permittivity will not be the same as for the bulk.
- Surface complexation: Several charged surfaces posses an increased attraction and support the formation of complex compounds at the surface, influencing the potential in their vicinity.

Insulator Surface Charge: Site-Binding Model

The Gouy–Chapmen–Stern model expresses the main contributions to the electric double layer. It relates the accumulated charge at the surface of the electrochemical interface to the applied potential. Up to now, only electrostatic interactions were considered and chemical reactions at the interface were neglected. However, there are potentially significant chemical reactions at the interface leading to a net charge aggregation at the insulators interface [237]. The site-binding model allows to include chemical reactions at the insulator's interface into the simulation. Chemical reactions, unlike electrostatic forces which interact over long ranges, are restricted to molecular distances. This encourages the assumption for the site-binding model, that chemical reactions are limited to the region between the surface and the OHP. Ionic species assigned to the dissolved salt exhibit a water shell and thus are restricted to stay outside the OHP. Hence, no ions can contribute to the chemical reactions at the insulator interface (neglecting the possibility of specific adsorption of salt ions). On the other hand, the much smaller hydrogen ions are not blocked by the OHP due to their smaller ionic radius and can approach the interface close enough to allow chemical reactions.

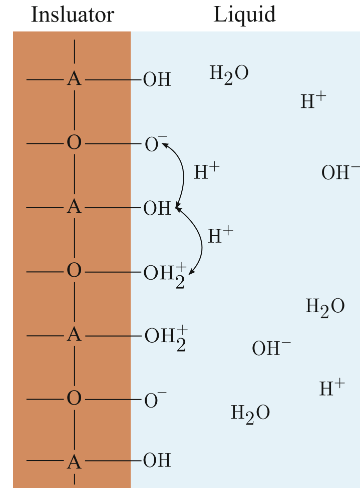

Fig. 1.15 Due to the lack of further bonding partners at the insulator surface there are open binding sites left. These binding sites may be either positively/negatively charged or neutral, depending on the properties of the liquid covering the surface. The surface charge density is related to the surface potential Ψ_0, material properties, and the local hydrogen concentration $[\mathrm{H}]_b^+$

Table 1.1 Parameters needed for the site-binding model commonly ($pK_i = -\log_{10}(K_i)$ analog to the definition of $pH = -\log_{10}([\mathrm{H}^+])$)

Oxide	pK_a	pK_b	N_s (cm^{-2})	Reference
SiO_2	−2	6	5×10^{14}	[29]
Si_3N_4	−8.1	6.2	5×10^{14}	[85]
Al_2O_3	6	10	8×10^{14}	[29]
Ta_2O_5	2	4	1×10^{15}	[30]
Gold surface	4.5	4.5	1×10^{18}	[60]

Figure 1.15 illustrates the open bonds of an insulator surface. Without unspecific adsorption, the only ions capable of binding to these sites are the hydrogen and hydroxyl ions [29, 128, 237]. The relation between the surface charge density, local potential and hydrogen concentration is given by [237]:

$$\sigma_{\mathrm{Ox}} = qN_s \frac{\frac{[\mathrm{H}^+]_b}{K_a} e^{-\frac{q\Psi_0}{qk_\mathrm{B}T}} - \frac{K_b}{[\mathrm{H}^+]_b} e^{\frac{q\Psi_0}{qk_\mathrm{B}T}}}{1 + \frac{[\mathrm{H}^+]_b}{K_a} e^{-\frac{q\Psi_0}{qk_\mathrm{B}T}} + \frac{K_b}{[\mathrm{H}^+]_b} e^{\frac{q\Psi_0}{qk_\mathrm{B}T}}}. \tag{1.223}$$

As an example some parameter sets for common materials are given in Table 1.1. The maximum amount of surface charge is directly proportional to the number of surface sites per unit area N_s, while the steepness and width of the two appearing steps is related to the difference between the reaction rates pK_a and pK_b. This additional effect influences the charge distribution in the double layer and in the semiconductor. Adding the site-binding model to the system of equations, the description of the ion-sensitive field-effect transistor (ISFET) is able to cover chemical reactions at the insulators surface. The charge aggregation at the oxide surface raises problems for the design of biosensors, while at the same time, it can be exploited to build highly efficient pH sensors [234].

The hydrogen concentration is properly taken into account at the oxide interface but outside of the OHP only the salt ions concentration is included and the

hydrogen concentration is ignored. This contradiction can be resolved as follows: At the oxide surface the hydrogen concentration strongly influences the equilibrium constants, while outside the OHP, the hydrogen diffusive layer is much smaller than the ion diffusive layer. For instance, in a dilute solution containing 1 mM of $NaCl$, the salt is fully dissolved into 1 mM Na^+ and 1 mM Cl^-. Assuming at the same time a pH of 7, the hydrogen concentration in the electrolyte will be about 100 nM. This states a concentration discrepancy of four orders of magnitude between the hydrogen and the sodium concentration. Thus, the hydrogen diffusive layer will only have negligible influence on the potential in the Gouy–Chapman layer in comparison to the site-binding region of the electrolyte.

BioFET Examples

There are two principle operation modes for detecting molecules: the first one exploits the change in surface charge density due to the pH sensitivity caused by the open binding sites at the oxide surface (also known as ISFET [23–25]). The second one utilizes the field-effect [165] discussed in this section. For the field-effect the intrinsic charge of the desired molecule is sensed directly without the intermediate step of generating H^+ or OH^- molecules. Due to the specific binding of the macromolecules via the *lock-key* principle, information about the macromolecules structure is contained.

At first an example for the modeling of a DNA-FET will be given. Several models have been investigated in order to find the best suited for a suspend gate FET (SGFET) at low salt concentrations [228]. The second example studies the detection of a streptavidin-biotin reaction depending on the molecules orientation and the employed dielectrics [229].

The ability of ISFET structures to detect the charge in deoxyribonucleic acid (DNA) can be utilized to build biosensors capable of detecting specific DNA sequences [128, 181, 227]. This application offers huge opportunities for many areas like food and environmental monitoring, development of patient specific drugs, and gene expression experiments. Hence, the simulation of so-called DNA-FETs is currently a topic of great interest. DNA and proteins are commonly considered as the main active components in all living organisms [210]. The DNA stores all the genetic information via molecular sequences within its polymere structure. Watson and Crick were the first to find that DNA consists of a double helix structure and each helix is build from a repeating structure, containing a sugar polymer, a nitrogen base, and a phosphate ion. The nitrogen base can be distinguished between four select bases. Namely, adenine (A), thymin (T), cytosine (C), and guanine (G). The repeating structure, also known as DNA strand, often consists of several millions of these base pairs and the specific order of bases in the DNA strand encodes the specific genetic information concerning an organism. A unique genetic sequence can be generated from particular subsequences of an organisms DNA, allowing a genetic finger print [210, 227]. The two helical strands are bound by weak hydrogen bonds. The thermodynamically favorable and therefore stable bonds are found between adenine and thymin, and between cytosine and guanine. Only helical DNA

strands with complementary bases are thermodynamically stable and form stable complexes. The process of double helix formation is called hybridization.

In [228], the experimental data of a SGFET have been studied via three different modeling approaches. The SGFET design is the same as for a standard MOSFET with one exception: it exhibits an elevated gate with an empty space under it. The bare gate-oxide layer is biofunctionalized with single stranded DNA and able to hybridize with a complementary strand. The intrinsic charge of DNA stems from its phosphate groups, with minus one elementary charge per group. The phosphate groups are fundamental building blocks of the DNAs nucleotides. Every base contained in the DNA is charged by minus one elementary charge. Therefore DNA possesses a high intrinsic charge, and big shifts in the transfer characteristics of BioFETs are induced. Thus, label-free, time-resolved, and in-situ detection of DNA is possible.

Harnois et al. [86] prepared a SGFET with 60 oligo-deoxynucleotides (ODN), also known as single stranded DNA, which were embedded onto a glutaraldehyd coated nitride layer. Test runs proved the specificity of the device. Their experimental data demonstrates two interesting properties. One is the fairly high threshold voltage shift of $\sim$800 mV and the other is that the probe transfer curve lies centered between the target and the reference curve. Typical threshold voltage shifts are in a range from several mV to $\sim$100 mV [165] and depend on the applied buffer concentration. Furthermore, the data display a big shift between the reference curve and the probe/target curve ($\sim$100 mV), but a much smaller shift between the probe and the target curve ($\sim 10-20$ mV) [186].

Three models were employed, trying to reproduce the device behavior: the Poisson–Boltzmann model in combination with a space charge equivalent to the charged DNA (60 base pairs probe and 120 base pairs target), the Poisson–Boltzmann model with a sheet charge describing the DNAs, and the Debye–Hückel model with a corresponding space charge. Figure 1.16a–c show the transfer characteristics for the unprepared SGFET (reference), the prepared but unbound (probe), and after the DNA has bound to functionalized surface (target), respectively. The experimental data are displayed in discrete grey tones to enable better comparison to the simulated curves. Even at a very low salt concentration of 0.6 mV, Fig. 1.16b, c exhibit a bigger shift between the reference curve and the probe/target curve than between probe and target curve. This behavior complies with observations in [186] and is caused by the nonlinear screening of the Poisson–Boltzmann model. Figure 1.17b, c show that doubling the charge does not lead to twice the curve shift. Even though there is a bigger shift for the sheet charge model due to the less screening in comparison to the model with the space charge, the overall trend is a bigger shift between the reference curve and the probe/target curve and a much smaller shift between the probe and the target curve.

On the other hand the employed Debye–Hückel model offers good agreement for the same parameter set as for the Poisson–Boltzmann models given in Fig. 1.16a. Figure 1.17a illustrates that for the Debye–Hückel model, doubling the charge is connected to twice the potential shift, due to the linear screening characteristics of the model.

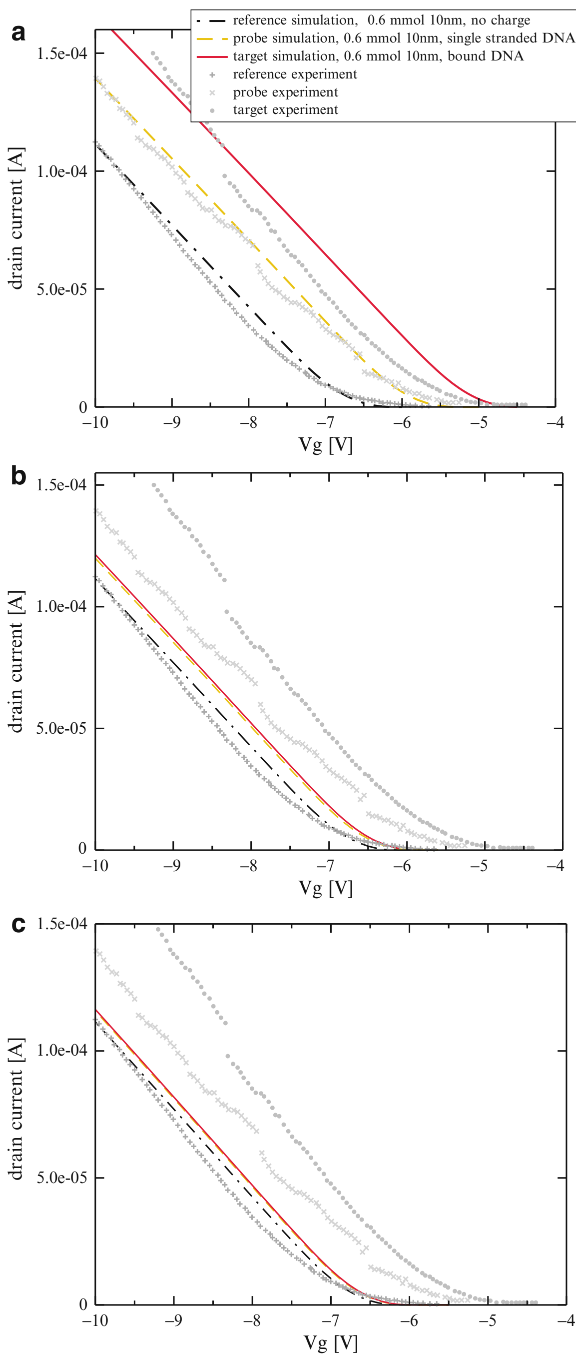

Fig. 1.16 The transfer characteristics for the Debye–Hückel model and DNA charge modeled via space charge density is given by (**a**), (**b**) shows the transfer characteristics for the same SGFET for the Poisson–Boltzmann model and DNA charge described via sheet charge density, and (**c**) illustrates the transfer characteristics of a SGFET for the Poisson–Boltzmann model and DNA charge modeled via space charge density

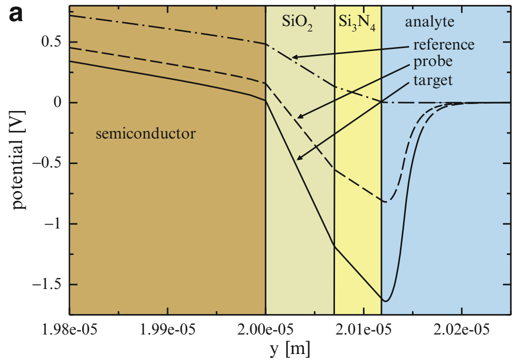

Potential for the Debye-Hückel model with space charge, showing that doubling the charge leads to twice the potential shift due to the weaker linear screening.

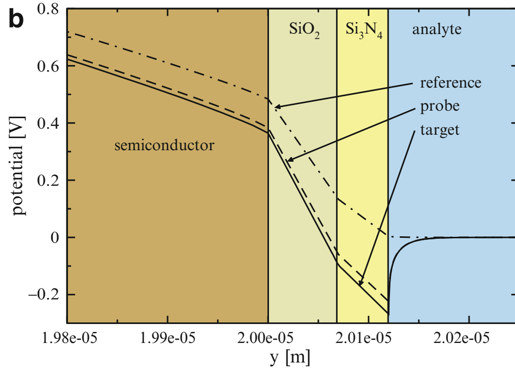

Potential for the Poisson-Boltzmann model with sheet charge, illustrating a bit increased shift but far away from the values from the measurement. However, doubling the charge does not lead to twice the potential shift due to nonlinear screening.

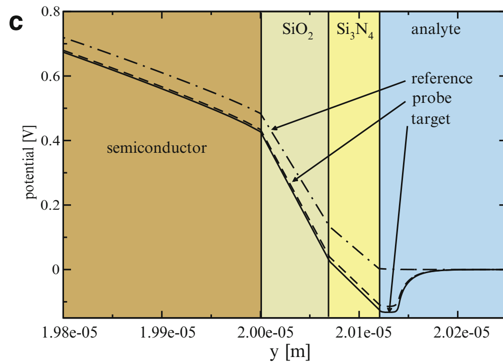

Potential for the Poisson-Boltzmann model with space charge, demonstrating doubling the charge also here does not lead to twice the potential shift due to nonlinear screening.

Fig. 1.17 The potential profile for the different modeling approaches, starting from the semiconductor (*left*) and ending in the analyte (*right*)

Assuming a single 60 bases DNA strand, it will occupy a volume of about $V_0 = 10 \times 10 \times 20\,\mathrm{nm}^3$. Taking this volume and multiplying it with 1 mM sodium-chloride bulk concentration results into approximately one sodium/chloride ion on average per V_0. Therefore, strong nonlinear screening at low salt concentrations is extremely unlikely. Furthermore, the Poisson–Boltzmann model is a continuum model and thus describes the salt concentration as a continuous quantity. This causes the Poisson–Boltzmann model to overestimate the screening and, therefore, to fail at small salt concentrations. The Debye–Hückel model is derived from the Poisson–Boltzmann model by expanding the exponential terms into a Taylor series and neglecting all terms higher than second-order [43]. Due to the laws of series expansion $q\Psi/k_\mathrm{B}T \ll 1$ the potential has to be much smaller than the thermal energy. However, even though this constraint is not fulfilled, the Debye–Hückel model is able to reproduce the data. One reasonable explanation might be that in this case the extended Poisson–Boltzmann model and the Debye–Hückel model coincide as shown in [228] and thus the screening depends on the average closest possible distance between the ions.

The second example studies a BioFET equipped with a biotin-streptavidin reaction for different dielectric materials and different molecule orientations at the surface.

Streptavidin is a tetrameric protein purified from the bacterium streptomyces avidini. Each subunit is able to bind biotin with equal affinity (Fig. 1.18). It is frequently used in molecular biology due to its very strong affinity for biotin which represents one of the strongest non-covalent interactions known in nature. It is commonly used for purification or detection of various biomolecules. With the aid of the strong streptavidin-biotin bond various biomolecules can be attached to one another or onto a solid support.

Here, the biotin-streptavidin reaction pair is modeled with the Poisson–Boltzmann model with homogenized interface conditions (1.149) and (1.150). The charge and dipole moment for a single molecule (biotin/streptavidin) is ob-

Fig. 1.18 The tetrameric protein streptavidin (*black*) and its four binding sites for biotin (*white*)

tained from a protein data bank [167] and extrapolated to the mean charge density and the mean dipole moment density of the boundary layer.

Three different oxide types were used as dielectric. SiO_2 served as a reference, Al_2O_3, and Ta_2O_5 were studied as possible high-k materials, with relative permittivities of 3.9, 10, and 25, respectively. The solute was sodium chloride at $pH = 7$. Several simulation runs were performed for each dielectric, such as the unprepared state (only water and salt), the prepared but unbound state (water, salt and biotin) and the bound state, when the chemical reaction took place (water, salt, and biotinstreptavidin), for two different molecule orientations (0°... perpendicular to the surface and 90°... parallel to the surface). The output characteristics were gained for several parameter combinations, under the prerequisite of 100% binding efficiency. The reference electrode was set to 0.4 V in order to shift the FET into moderate inversion as proposed in [44].

Figure 1.19 compares the output characteristics for the different employed dielectrics and molecule orientations. The following trends are recognizable: the lowest output characteristics are found for 0°, followed by 90°, and finally without dipole moment, for each group. This is caused by the inhomogeneously charged biomolecules and the related dipole moment entering the boundary conditions (1.150), hence, resulting in different output characteristics of the BioFET for different orientation angles in relation to the surface. Furthermore, higher ε_r leads to higher output currents, due to the better coupling of the surface charge to the channel.

There are several conclusions which can be deduced by considering the molecules electrostatic properties. The signal-to-noise ratio can be improved by exploiting a only minimally charged or better a neutral linker. Therefore, in the

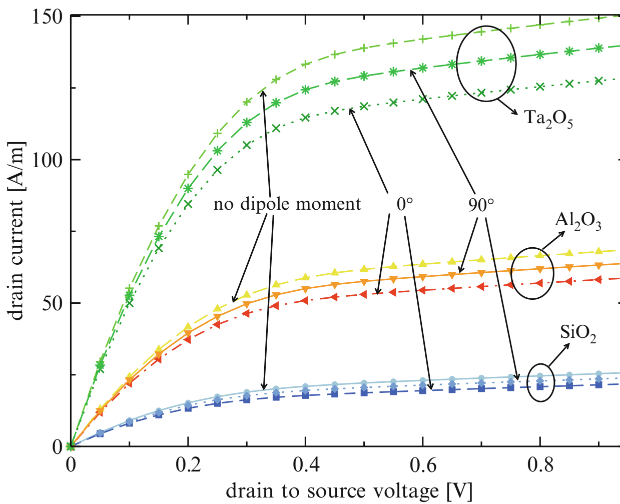

Fig. 1.19 Output characteristics for SiO_2, Al_2O_3, and Ta_2O_5 for calculation without dipole moment, 0° (perpendicular to surface), and 90° (parallel to surface)

case of detecting strepatividin via biotin, biotin should be attached to the surface by a neutral linker. Streptavidin is negatively charged with minus four elementary charges and biotin with minus one elementary charge. By attaching streptavidin after biotin to the surface the relative change in surface charge will be quite big, even when partial screening of the intrinsic charges is taken into account. Due to the tetrameric nature of streptavidin (four binding sites for biotin, Fig. 1.18), the linker utilized should be short enough to prevent binding several biotin molecules to a single streptavidin protein. Furthermore, if there is freedom of choice in deciding, wether biotin or streptavidin is initially attached to the surface, biotin is a better choice. In this case the relative change in charge will be bigger (from minus one elementary charge to minus five elementary charges) yielding a more pronounced change in the output signal.

Summarizing the results gained by the Poisson–Boltzmann model with homogenized interface conditions show a strong dependence on surface charges and indicate a detectable shift in the threshold voltage depending on the molecule orientation relative to the surface.

8.3 Thermovoltaic Elements

In the last decades enormous efforts in engineering and science were taken to increase the fuel efficiency, but unfortunately it has not been possible to keep up with the economical growth. Thermoelectric energy conversion is one among several technologies with the potential to break through in future energy technology. The underlying physical effect has been well known for about 200 years and is based on the direct energy conversion from temperature gradients into electrical energy. Despite extensive research efforts, the usage of the thermoelectric energy is still restricted to few highly specialized fields, due to a low conversion efficiency. The enormous efforts on material research over the last years introduced novel materials for thermoelectric devices as well as a better understanding of the prerequisites for higher conversion efficiencies.

8.3.1 Materials for Thermoelectric Devices

The goal of research and engineering of materials for thermoelectric devices is to maximize their efficiency. A potentially promising thermoelectric material is characterized by a high Seebeck coefficient, good electric transport properties, and an impeded thermal transport [150]. Commonly, these material properties are accompanied with a pronounced temperature dependence yielding ideal thermal operation conditions for a certain material.

In this section, thermoelectric materials with technological importance and their operational range are introduced. Silicon-germanium alloys are appealing due to their low thermal conductivity compared to pure materials. Furthermore, *SiGe* is attractive due to its importance in mainstream electronics and the availability of an elaborate physical description.

Lead telluride (*PbTe*) is used in the intermediate temperature range with a maximum operation temperature of approximately 900 K. Apart from its application in thermoelectric devices, lead telluride is employed for optical devices in the infrared wavelength regime. Additionally to doping, the material properties can be altered by deviating its stoichiometric composition. Ternary alloys are also part of ongoing research efforts. In principle, lead telluride is avaliable as p-type as well as n-type material but, contrary to the n-type material, the p-type material suffers from degradation of stability at high temperatures and devices are difficult to bond and exhibit poorer mechanical properties [199]. Therefore, the p-doped leg is frequently exchanged by alloys containing silver antimony and germanium telluride, also known as *TAGS*.

Bismuth telluride stands at the lower end of the temperature scale. Because of its good thermoelectric properties at room temperature, it is frequently utilized for cooling applications. By analogy to lead telluride, the material type and number of excess carriers can be controlled by adjusting the stoichiometry of the alloy.

Apart from these classical thermoelectric materials frequently employed in generation and cooling applications, there are ongoing research efforts on novel materials [21, 22, 149] and specially designed nanostructures for thermoelectric applications [37, 38, 119, 121, 145, 232, 235, 236, 240].

Material Characterization

The performance of thermoelectric generators is judged by their characteristic numbers as efficiency, total power output, and power density. The efficiency is limited by several parameters. Apart from the geometrical construction, several material properties as the Seebeck coefficient, the thermal conductivity, and the electrical conductivity, influence the transport of charge carriers and phonons and thus the overall device characteristics. Here the figure of merit for thermoelectric materials comes into play. It embraces the material parameters influencing the device behavior as well as the device efficiency.

Ioffe [101] showed that the maximum conversion efficiency $\eta_{\max}$ of a thermoelectric generator at matched load conditions is obtained via the product of the ideal reversible thermodynamic process efficiency and a factor describing the energy losses in the device due to Joule heating and non-ideal thermal conductivity [231]

$$\eta_{\max} = \frac{T_h - T_c}{T_h} \frac{M - 1}{M + \frac{T_c}{T_h}}, \tag{1.224}$$

where T_h and T_c describe the temperature of the heated and the cooled side of the device, respectively and M is given by:

$$M = \sqrt{1 + \frac{1}{2} Z \left(T_c + T_h\right)}. \tag{1.225}$$

The averaged thermoelectric figure of merit for each leg (different subscripts for each leg) and matched geometry is defined by:

$$Z = \frac{(\alpha_1 - \alpha_2)^2}{\left(\sqrt{\frac{\kappa_1}{\sigma_1}} + \sqrt{\frac{\kappa_2}{\sigma_2}}\right)^2}. \tag{1.226}$$

Equation (1.226) incorporates all significant material parameters like the Seebeck coefficient α, thermal conductivity κ, and the electric conductivity σ. Since the figure of merit exhibits a strong dependence on temperature as well as on the concentration of free carriers, inherited from its input quantities, every material possesses an optimum range of operation. However, common devices have legs with similar material properties and the so-called bulk figure of merit for a given material can be used:

$$Z = \frac{\alpha^2 \sigma}{\kappa}. \tag{1.227}$$

From a microscopic viewpoint, the figure of merit is affected by charge and heat transport as well as their interaction in the semiconductor. Thus, the figure of merit depends on band structure, lattice dynamics, and charge carriers scattering mechanisms.

While higher doping levels commonly have an adverse effect on the Seebeck coefficient, the electric conductivity increases due to the increased number of carriers. The electric part of the thermal conductivity κ_ν becomes significant at high carrier concentrations and even the dominant thermal conductivity mechanism on the transition to metals. Insulators and metals exhibit superior conditions for single parameters, but at the same time poor conditions for others. For instance, metals are known for their low Seebeck coefficients and relatively high thermal conductivities, which can not be counterbalanced by their high electric conductivities. Semiconductors lie approximately in the middle of the competing parameter ranges and, thus, are able to yield a maximal thermoelectric figure of merit. This maximum is reinforced by still moderate Seebeck coefficients and low electrical resistance but restricted electron thermal conductivity in the regions of high carrier concentrations. Furthermore the optimum carrier concentration can be adjusted by an appropriate doping.

Silicon-Germanium

SiGe thermogenerators have been effectively employed in several applications. Among these, the utilization as thermogenerators powered by radioisotopes (RTG), as reliable power source on space missions and in remote weather stations is probably the most impressive one [166]. Due to its high reliability and high operating temperatures, *SiGe* is also a good candidate to meet the conditions in nuclear reactors.

SiGe also constitutes an important material system due to it's use in mainstream microelectronics. Initiated by the introduction of strain techniques to commercially avaliable devices, the research efforts on the properties and processability of *Si*/*SiGe* were intensified [10, 39, 176]. A detailed analysis and material characterization of *SiGe* alloys with emphasis on physical modeling for device simulation has been presented in [157], and a review on the mobility modeling at high temperatures can be found in [179]. *SiGe* alloys are attractive due to their differing influence on thermal conductivity and mobility for varying composition, in comparison to their pure constitutes. Vining [223] and Slack et al. [200] studied the theoretical maximal figure of merit. While in [223] a two-band model has been employed, in [200] the second conduction band has been considered, yielding a broader temperature range of the validity of the model.

With increasing germanium content (up to 50%) the lattice thermal conductivity of *SiGe* reduces significantly. For increasing germanium content this trend first halts, than begins to reverse, and finally reaches the value of pure germanium content. The reason for this characteristic is alloy disorder scattering of phonons, created by the random distribution of silicon and germanium in the alloy [17]. A further reduction in thermal conductivity has been reported for sintered samples, due to extra phonon scattering at the grain boundaries [143].

Sintered composites exhibit a low sensitivity of the thermal conductivity on the material composition over a wide range of germanium content and, therefore, posses a good figure of merit. This proves beneficial for inhomogeneous samples, where clustering causes relatively large localized deviations in the material parameters. Compared to the thermal conductivity, the mobility decreases more slowly with rising germanium content yielding a range with favorable figures of merit. The Seebeck coefficient for pure silicon, germanium, and several of their alloys have been determined and documented in the literature [9, 55, 57, 58, 174].

Despite the excellent reliability performance of *SiGe* alloys, there are degradation effects for *SiGe* thermoelectric generators, reducing the figure of merit over the device lifetime [223]. High temperature conditions may cause sublimation and result in thermal and/or electrical shortcuts. Furthermore, erosion can appear under extreme conditions and induce device failure by open circuits or mechanical damage. Additionally, high doping concentrations, intentionally introduced to raise the figure of merit, are prone to build up local accumulations. These accumulations reduce the free carrier concentration, decrease the electric conductivity, and degrade the figure of merit. Due to the lower diffusion rate of boron doped p-type samples compared to n-type samples doped with phosphorus, the p-samples are less sensitive to this phenomenon.

Lead Telluride and Its Alloys

Lead telluride (*PbTe*) and lead tin telluride ($Pb_{1-x}Sn_xTe$) devices operate with regard to temperature between those of bismuth telluride and silicon-germanium. Despite the slightly smaller maximum figure of merit compared to bismuth telluride,

lead telluride exhibits an equivalently good efficiency over a large temperature window. By changing the stoichiometry of the material composition the electrical properties of the alloy can be adjusted. Utilizing an excess of tellurium results in a p-type semiconductor, while a raised plumbum content has the adverse effect and gives a n-type semiconductor. However, this processing path restricts a maximum carrier concentration to about $10^{18}\,cm^{-3}$, which is lower than the ideal doping for thermoelectric applications [166]. Therefore, higher carrier concentrations are realized by doping with PbI_2, $PbBr_2$, or Ge_2Te_3 for an increased donor concentration and Na_2Te or K_2Te for elevated acceptor concentrations.

Lead telluride and lead tin telluride are available as sintered materials as well as single crystals. Sintered samples exhibit a lower thermal and electrical conductivity compared to single crystals due to the additional scattering at the grain boundaries [49].

Bismuth Telluride and Its Alloys

Bismuth telluride (Bi_2Te_3) and some related alloys are frequently used for cooling applications in commercial Peltier elements due to a good thermoelectric figure of merit at room temperature. Common ternary alloys are bismuth telluride either with bismuth selenide (Bi_2Se_3) or antimony telluride (Sb_2Te_3) [46]. Their crystal structure is characterized as hexagonal [126], but also has been described as rhombohedral [35]. The temperature range for thermoelectric applications of Bi_2Te_3 is limited by its melting point at 858 K [48].

By analogy to lead telluride the free carrier concentration can be controlled, either by changing the material composition or by extra dopants. Contrary to lead telluride, stoichiometric bismuth telluride is of p-type with a free carrier concentration of about $10^{19}\,cm^{-3}$. Raising the tellurium concentration converts the material to n-type.

Bismuth telluride belongs to the group of narrow gap semiconductors and possesses an indirect band gap of 160 mV at 300 K. The population of higher energy levels is relatively high due to a low DOS. Therefore, the large non-parabolicity of the bandstructure is of significance [27]. Founding on the theoretical work of [131,178] experimental work has been accomplished, serving as a basis for future performance optimizations, e.g. introduction of low-dimensional structures [191].

Reducing the thermal conductivity is also a possible solution in order to increase the figure of merit. Ternary alloys show a dependence of the lattice thermal conductivity on the additional phonon scattering by alloy disordering. Bismuth antimony telluride, in the form of $(Bi_{0.5}Sb_{0.5})_2\,Te_3$, features the highest lattice disorder and therefore the lowest thermal conductivity [180]. However, related to the adverse effect on the evolution of the electrical conductivity and the carrier contribution to the total thermal conductivity, the maximum figure of merit is gained at higher antimony content [64, 65]. In analogy to the previous materials, sintered samples show a reduced lattice thermal conductivity due to extra grain boundary scattering [211]. The influence of dopants on the thermal conductivity has been studied in [239].

The overall device performance of a thermoelectric generator is lower than the theoretical maximum, due to the narrow temperature range of about 50 K for the maximum figure of merit. A possible solution to circumvent this limitation is to incorporate graded or segmented materials along the temperature gradient in order to meet the optimum material properties [127].

Optical, transport, and several mechanical parameters exhibit a strong anisotropy. Despite the relatively isotropic Seebeck coefficient with deviations of about 10% between the opposing extrema, the electrical resistivity and the thermal conductivity show anisotropy ratios of 4–6 and 2–2.5, respectively [66, 93, 180]. p-type as well as n-type samples show Seebeck coefficients between 100 and 250 μV K^{-1} depending on the material composition [5,51]. The maximum observed figure of merit is in direction parallel to the cleavage plain and is superior to the normal direction by a factor of 2.

8.3.2 Examples

The first introduced thermoelectric generator type is commonly used in commercial energy conversion applications and is based on the classical design of thermocouples and temperature sensors. It is built from two semiconducting legs, one consisting of n-type semiconductor and the other of p-type semiconductor (Fig. 1.20). The p-type leg features a larger cross section than the n-type leg in order to compensate the lower hole mobility. The two legs are arranged thermally in parallel and electrically in series, exhibiting an electrical contact at the heated side of the device. Since the signs of the Seebeck coefficients of the two legs are opposing, their voltage contributions add up to the total voltage of the device.

The second example represents an alternative thermoelectric device and is built from a large area pn-junction [202]. The principle of its design is illustrated in Fig. 1.21. The contacts are situated at the cooled end of the device structure

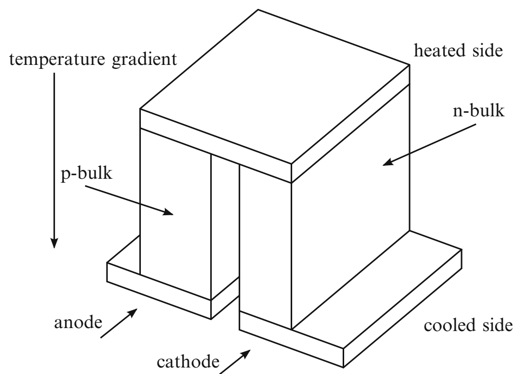

Fig. 1.20 Scheme of a thermoelectric device

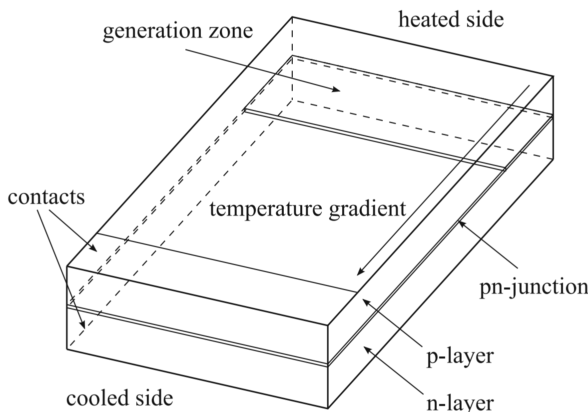

Fig. 1.21 Scheme of a large pn-junction thermoelectric generator

and the temperature gradient is brought into play along the pn-junction. Contrary to conventional thermoelectric devices, the thermal electron–hole pair generation is exploited in a large area pn-junction. Applying a temperature gradient within the structure, induces the generation of an electric current which is related to the temperature effect on the electrostatic potential of the pn-junction. Higher temperatures lead to a smaller energy step from the potential of the n-layer to the p-layer compared to the step at lower temperatures. Due to the temperature gradient in the large area pn-junction both conditions exist in the same device and thus carriers at the higher potential experience a driving force into the colder region. Both carrier types move into the same direction (ambipolar drift and diffusion). They leave the pn-junction at the high temperature, which therefore becomes depleted and induces a disturbance in the local thermal equilibrium. This shifts the local generation-recombination balance to a raised generation of carriers in order to compensate the off-drifting carriers, while at the end of the device with the lower temperature the opposite effect takes place. Therefore, a circular current is driven from the hot region with increased generation to the cold region with enhanced recombination. Using selective contacts for the n- and the p-layer, the circular current can be exploited for an external load, and a power source in the form of a thermoelectric element is established.

Depending on the environmental conditions, the devices can either be connected in series for a higher output voltage or in parallel for higher output currents. Similar reasoning is valid for the thermal circuit. Multiple single elements on the same temperature level increase the heat flux through the entire module in order to exhaust relatively strong temperature reservoirs at temperature differences suitable for a single stage. For an ambience with a higher temperature difference it is beneficial to apply modules with multiple stages, where each stage is optimized for a certain temperature.

Reduced Thermal Conductivity by Alloys

The enhanced phonon scattering rates for *SiGe* alloys lead to a strongly pronounced reduction in phonon thermal conductivity in comparison to pure silicon, but also influence several other parameters. Therefore, a trade-off has to be found between the beneficial lower thermal conductivity and the decrease of carrier mobility to achieve the optimum improvement of conversion efficiency.

Wagner [224] carried out simulations for a thermoelectric generator exhibiting a leg length of 20 mm and a cross section of $5 \times 1\,\mathrm{mm}^2$. The dopings for both legs were set constant to $10^{19}\,\mathrm{cm}^{-3}$ and the temperature difference was considered to be situated 600 K above room temperature.

With increasing germanium content, the Seebeck voltages as well as the mobility decrease over a wide range and lead to a drop in output current. Figure 1.22 demonstrates that the highest electric output is obtained in pure silicon. Low mobility in *SiGe* causes a reduction in the absolute maximum of the power output and shifts it to higher resistances.

However, the influence of the material composition on the thermal conductivity and thus the heat flux through the device outweighs the negative impact on the electrical properties [224]. The heat flux decreases to a minimum at approximately 50% germanium concentration which is an order of magnitude lower than for pure silicon. The resulting maximum of conversion efficiency is expected at about 30% germanium content, where the optimum between thermal and electrical properties

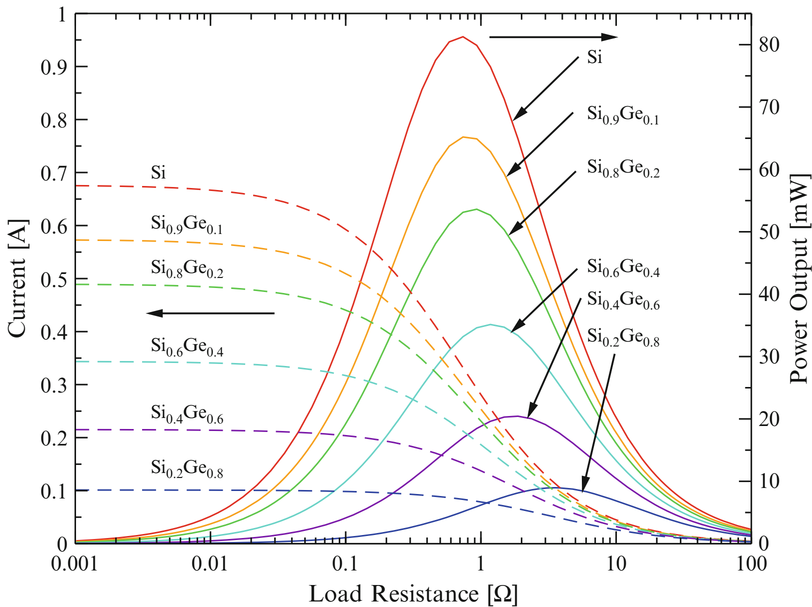

Fig. 1.22 Electric current and power output as a function of load resistance for several *SiGe* alloys

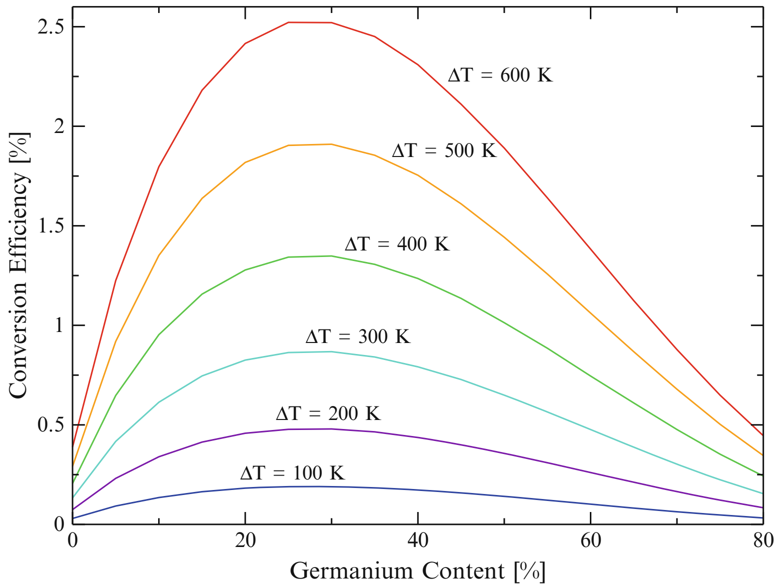

Fig. 1.23 Illustrating the conversion efficiency in relation to the material composition and temperatures

is situated. At higher germanium content, the thermal conductivity still decreases, but can not compensate the degrading mobility and Seebeck voltages any longer. Figure 1.23 depicts the conversion efficiency in relation to the material composition at match load conditions. While the power output continuingly decreases with increasing germanium content, the conversion efficiency reaches its maximum at approximately 30% germanium.

pn-Junctions as Thermoelectric Devices

The device characteristics of a pn-junction thermoelectric generator are mainly controlled by carrier generation. Due to the strong influence of the lattice temperature on the carrier generation, the zone of high generation rates is restricted to the hottest parts of the structure.

Therefore it is advantageous to keep large parts of the device at high temperatures. In the case of a pure material, the temperature distribution along the pn-junction is concave because of the decreasing thermal conductivity with increasing temperature. This yields a steep temperature gradient at the heated end and a relatively short zone at high temperature, restricting the carrier generation.

By engineering the spatial distribution of the thermal conductivity it is possible to increase the dimension of the zone at high temperatures. The implementation of graded material alloys is a pathway to achieve this. *SiGe* alloys decrease their

thermal conductivity up to 50% germanium content. A device profile with higher germanium content at the cooled side of the device leads to a shift of the temperature drop to the cooled side of the device, in analogy to a potential divider in the electric counterpart of the model.

However, in addition to high total carrier generation rates, the carriers have to be efficiently transferred to the contacts. Doping as well as the geometrical dimensions of the transport layers have to be chosen accordingly in order to keep recombination as small as possible. Geometrically oversized transport layers increase the heat flux but do not change the electric properties, which leads to a decrease in efficiency. Thus, the goal of efficient device optimization is the careful analysis of the interrelation of several effects in the device.

Figure 1.24 [224] illustrates the relation between the transport layer thickness, available temperature difference, and power output. The dashed line denotes the maximum power output curve for an initially chosen device geometry, while the solid line shows the corresponding optimized device with thicker layers. Caused by the lower internal resistance, the optimum power output shifts to a lower load resistance too. Additionally, the temperature scale along the maximum power output curve shifts to higher values and thus the same thermal environment results in a significantly enhanced power output.

Due to the dependence of the device on the carrier generation rate, one can further improve the device performance by introducing trap states in the forbidden energy gap. In accordance with the Shockley–Read–Hall formalism [189] the carrier generation rate is controlled by the local temperature, the amount of traps, and the energy levels of the traps. Trap energy levels situated in the middle of the band

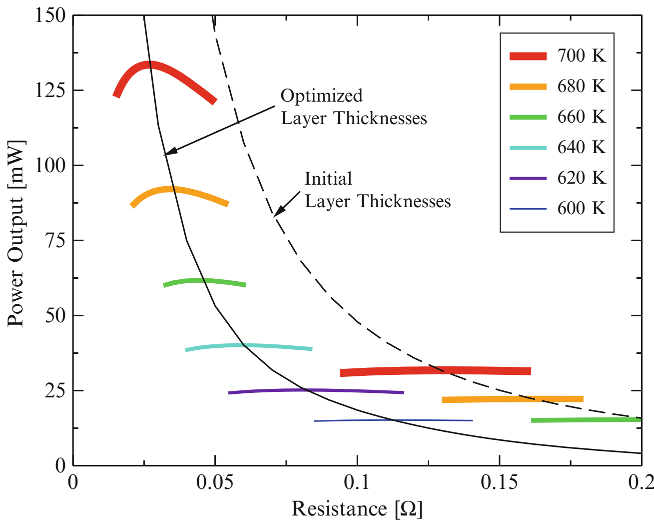

Fig. 1.24 Power output for a pn-junction thermoelectric generator in relation to load resistance, for several temperatures and two layer thicknesses

gap yield the highest thermal generation rates. For instance, for silicon, gold can be exploited as an additional dopant in the generation region of the device to add deep levels close to the mid band gap [171]. Due to the ability of the impurity state to absorb differences in momentum between the carriers, this carrier generation process is dominant in silicon and other indirect semiconductors. Hence, in a certain regime, the device performance of a pn-junction thermoelectric generator at a specific temperature can be shifted to lower temperatures by adjusting the extra trap concentration and distribution.

Acknowledgements Special thanks go to Prof. Tibor Grasser, Prof. Hans Kosina, and Neophytos Neophytou for their support in questions related to higher order transport models and modeling transport in thermovoltaic elements. Also the various discussions about higher order transport models and nice pictures regarding higher order transport models and SHE from Martin Vasicek, and the examples related to thermovoltaic elements from Martin Wagner are highly appreciated. This work was partly funded by the Austrian Science Fund project P18316-N13 and partly by the "Klima- und Energiefonds" Austria, project No. 825467.

References

1. Aberle, A.: Crystalline Silicon Solar Cells: Advanced Surface Passivation and Analysis. Centre for Photovoltaic Engineering, University of New South Wales, Sydney (1999)
2. Abramowitz, M., Stegun, I.: Handbook of Mathematical Functions. Dover Publications Inc. (1965)
3. Adler, M.: Accurate Calculations of the Forward Drop and Power Dissipation in Thyristors. IEEE Trans.Electron Devices **25**(1), 16–22 (1978)
4. Agostinelli, V.J., Bordelon, T., Wang, X., Yeap, C., Maziar, C., Tasch, A.: An Energy-Dependent Two-Dimensional Substrate Current Model for the Simulation of Submicrometer MOSFET's. IEEE Electron Device Lett. **13**(11), 554–556 (1992). DOI 10.1109/55.192837
5. Ainsworth, L.: Single Crystal Bismuth Telluride. Proc.Phys.Soc.B **69**(6), 606–612 (1956)
6. Allen, C., Jeon, J.H., Woodall, J.: Simulation Assisted Design of a Gallium Phosphide n-p Photovoltaic Junction. Solar Energy Materials and Solar Cells **94**(5), 865–868 (2010). DOI 10.1016/j.solmat.2010.01.009
7. Altenkirch, E.: Über den Nutzeffekt der Thermosäule. Physikalische Zeitschrift **10**, 560–580 (1909)
8. Altenkirch, E.: Elektrothermische Kälteerzeugung und reversible elektrische Heizung. Physikalische Zeitschrift **12**, 920–924 (1911)
9. Amith, A.: Seebeck Coefficient in n-Type Germanium-Silicon Alloys: "Competition" Region. Physical Review **139**(5A), A1624–A1627 (1965). DOI 10.1103/PhysRev.139.A1624
10. Andrieu, F., Ernst, T., Faynot, O., Rozeau, O., Bogumilowicz, Y., Hartmann, J., Brévard, L., Toffoli, A., Lafond, D., Ghyselen, B., Fournel, F., Ghibaudo, G., Deleonibus, S.: Performance and Physics of sub-50 nm Strained Si on $Si_{1-x}Ge_x$-On-Insulator (SGOI) nMOSFETs. Solid-State Electron. **50**(4), 566–572 (2006). DOI 10.1016/j.sse.2006.03.029
11. Anile, A., Pennisi, S.: Extended Thermodynamics of the Blotekjaer Hydrodynamical Model for Semiconductors. Continuum Mechanics and Thermodynamics **4**(3), 187–197 (1992). DOI 10.1007/BF01130290
12. Anile, A.M., Muscato, O.: Improved Hydrodynamical Model for Carrier Transport in Semiconductors. Physical Review B **51**(23), 16,728–16,740 (1995). DOI 10.1103/PhysRevB.51.16728

13. Apel, P., Korchev, Y., Siwy, Z., Spohr, R., Yoshida, M.: Diode-Like Single-Ion Track Membrane Prepared by Electro-Stopping. Nucl. Instrum. and Meth. in Phys. Res. Sect. B: Beam Interactions with Materials and Atoms **184**(3), 337–346 (2001). DOI 10.1016/S0168-583X(01)00722-4
14. Ashcroft, N., Mermin, N.: Solid State Physics. Cengage Learning Services (1976)
15. Baccarani, G., Rudan, M., Guerrieri, R., Ciampolini, P.: Physical Models for Numerical Device Simulation, vol. 1. North-Holland Publishing Co., Amsterdam, The Netherlands (1986)
16. Baccarani, G., Wordeman, M.: An Investigation of Steady-State Velocity Overshoot in Silicon. Solid-State Electron. **28**(4), 407–416 (1985). DOI 10.1016/0038-1101(85)90100-5
17. Bahandari, C.: CRC Handbook of Thermoelectrics, Chapter: Minimizing the Thermal Conductivity. CRC Press LLC (1994)
18. Baker, N.A., Sept, D., J., S., Holst, M.J., McCammon, J.A.: Electrostatics of Nanosystems: Application to Microtubules and the Ribosome. Proc. of the National Academy of Sciences of the United States of America **98**(18), 10,037–10,041 (2001). DOI 10.1073/pnas.181342398
19. Bandyopadhyay, S., Klausmeier-Brown, M., Maziar, C., Datta, S., Lundstrom, M.: A Rigorous Technique to Couple Monte Carlo and Drift-Diffusion Models for Computationally Efficient Device Simulation. IEEE Trans.Electron Devices **34**(2), 392–399 (1987)
20. Barcilon, V., Chen, D.P., Eisenberg, R.S., Jerome, J.W.: Qualitative Properties of Steady-State Poisson-Nernst-Planck Systems: Perturbation and Simulation Study. SIAM J. Appl. Math. **57**(3), 631–648 (1997). DOI 10.1137/S0036139995312149
21. Bentien, A., Christensen, M., Bryan, J., Sanchez, A., Paschen, S., Steglich, F., Stucky, G., Iversen, B.: Thermal Conductivity of Thermoelectric Clathrates. Physical Review B **69**(4) (2004). DOI 10.1103/PhysRevB.69.045107
22. Bentien, A., Johnsen, S., Madsen, G., Iversen, B., Steglich, F.: Colossal Seebeck Coefficient in Strongly Correlated Semiconductor $FeSb_2$. EPL (Europhysics Letters) **80**(1), 17,008 (2007). stacks.iop.org/0295-5075/80/17008
23. Bergveld, P.: Development of an Ion-Sensitive Solid-State Device for Neurophysiological Measurements. IEEE Trans. Biomed. Eng. **17**(1), 70–71 (1970). DOI 10.1109/TBME.1970.4502688
24. Bergveld, P.: The Development and Application of FET-Based Biosensors. Biosensors **2**(1), 15–34 (1986)
25. Bergveld, P.: Thirty Years of ISFETOLOGY: What Happened in the Past 30 Years and What May Happen in the Next 30 Years. Sensors and Actuators B: Chemical **88**(1), 1–20 (2003). DOI 10.1016/S0925-4005(02)00301-5
26. Beynon, R., Easterby, J.: Buffer Solutions the Basiscs. Oxford University Press, Oxford New York Tokyo (1996)
27. Bhandari, C., Agrawal, V.: Thermal and Electrical Transport in Bismuth Telluride. Indian Journal of Pure and Applied Physics **28**, 448–451 (1990)
28. Bløtekjær, K.: Transport Equations for Electrons in Two-Valley Semiconductors. IEEE Intl. Electron Devices Meeting **17**, 38–47 (1969)
29. Bousse, L.: Single Electrode Potentials Related to Flat-Band Voltage Measurements on EOS and MOS Structures. J.Chem.Phys. **76**(10), 5128–5133 (1982). DOI 10.1063/1.442812
30. Bousse, L., Mostarshed, S., Van Der Shoot, B., De Rooij, N.F., Gimmel, P., Gopel, W.: Zeta Potential Measurements of Ta_2O_5 and SiO_2 Thin Films. Journal of Colloid and Interface Science **147**(1), 22–32 (1991)
31. Brugger, S., Schenk, A., Fichtner, W.: Moments of the Inverse Scattering Operator of the Boltzmann Equation: Theory and Applications. SIAM Journal on Applied Mathematics **66**(4), 1209–1226 (2006). DOI 10.1.1.72.3270
32. Callen, H.: Thermodynamics. John Wiley & Sons Inc. (1966)
33. Campa, A., Krc, J., Topic, M.: Analysis and Optimisation of Microcrystalline Silicon Solar Cells with Periodic Sinusoidal Textured Interfaces by Two-Dimensional Optical Simulations. J.Appl.Phys. **105**(8), 083,107–083,107–5 (2009). DOI 10.1063/1.3115408
34. Caughey, D., Thomas, R.: Carrier Mobilities in Silicon Empirically Related to Doping and Field. Proc.IEEE **55**(12), 2192–2193 (1967)

35. Caywood, L.P., Miller, G.R.: Anistropy of the Constant-Energy Surfaces in *n*-type Bi_2Te_3 and Bi_2Se_3 from Galvanomagnetic Coefficients. Physical Review B **2**(8), 3209–3220 (1970). DOI 10.1103/PhysRevB.2.3209
36. Cervera, J., Schiedt, B., Ramírez, P.: A Poisson/Nernst-Planck Model for Ionic Transport Through Synthetic Conical Nanopores. Europhys. Lett. **71**(1), 35–41 (2005). DOI 10.1209/epl/i2005-10054-x
37. Chen, G., Narayanaswamy, A., Dames, C.: Engineering Nanoscale Phonon and Photon Transport for Direct Energy Conversion. Superlattices and Microstructures **35**(3-6), 161–172 (2004). DOI 10.1016/j.spmi.2003.08.001. Eurotherm 75 'Microscale Heat Transfer 2'
38. Chen, G., Zeng, T., Borca-Tasciuc, T., Song, D.: Phonon Engineering in Nanostructures for Solid-State Energy Conversion. Mat.Sci.Eng.A **292**(2), 155–161 (2000). DOI 10.1016/S0921-5093(00)00999-0
39. Cheng, Z., , Currie, M., Leitz, C., Taraschi, G., Fitzgerald, E., Hoyt, J., Antoniadas, D.: Electron Mobility Enhancement in Strained-*Si* n-MOSFETs Fabricated on *SiGe*-On-Insulator (SGOI) Substrates. IEEE Electron Device Lett. **22**, 321–323 (2001). DOI 10.1109/55.930678
40. Chynoweth, A.: Ionization Rates for Electrons and Holes in Silicon. Physical Review **109**(5), 1537–1540 (1958). DOI 10.1103/PhysRev.109.1537
41. Coalson, R., Kurnikova, M.: Poisson-Nernst-Planck Theory Approach to the Calculation of Current Through Biological Ion Channels. IEEE Trans. NanoBioscience **4**(1), 81–93 (2005). DOI 10.1109/TNB.2004.842495
42. Cui, Y., Wei, Q., Park, H., Lieber, C.M.: Nanowire Nanosensors for Highly Sensitive and Selective Detection of Biological and Chemical Species. Science **293**(5533), 1289–1292 (2001)
43. Debye, P., Hückel, E.: Zur Theorie der Elektrolyte: I. Gefrierpunktserniedrigung und verwandte Erscheinungen. Physikalische Zeitschrift **24**(9), 185–206 (1923)
44. Deen, M.J., Shinwari, M.W., Ranuárez, J.C., Landheer, D.: Noise Considerations in Field-Effect Biosensors. J.Appl.Phys. **100**(7), 074,703–1 –074,703–8 (2006)
45. Delahay, P.: Double Layer and Electrode Kinetics. New York: Interscience Publishers (1965)
46. Ding, Z., Huang, S., Marcus, D., Kaner, R.: Modification of Bismuth Telluride for Improving Thermoelectric Properties. In: Intl. Conf. on Thermoelectrics, pp. 721–724 (1999). DOI 10.1109/ICT.1999.843487
47. van Dort, M., Woerlee, P., Walker, A.: A Simple Model for Quantisation Effects in Heavily-Doped Silicon MOSFETs at Inversion Conditions. Solid-State Electron. **37**(3), 411–414 (1994). DOI 10.1016/0038-1101(94)90005-1
48. Drabble, J.: Progress in Semiconductors, vol. 7. John Wiley & Sons Inc., New York (1963)
49. Fano, V.: CRC Handbook of Thermoelectrics, Chapter: Lead Telluride and Its Alloys. CRC Press LLC (1994)
50. Fischetti, M.: Monte Carlo Simulation of Transport in Technologically Significant Semiconductors of the Diamond and Zinc-Blende Structures. I. Homogeneous Transport. IEEE Trans.Electron Devices **38**(3), 634–649 (1991). DOI 10.1109/16.75176
51. Fleurial, J., Gailliard, L., Triboulet, R., Scherrer, H., Scherrer, S.: Thermal Properties of High Quality Single Crystals of Bismuth Telluride Part I: Experimental Characterization. J.Phys.Chem.Solids **49**(10), 1237–1247 (1988). DOI 10.1016/0022-3697(88)90182-5
52. World Record: 41.1% Efficiency Reached for Multi-Junction Solar Cells at Fraunhofer ISE. Press Release (2009). www.ise.fraunhofer.de
53. Fritz, J., Cooper, E., Gaudet, S., Soger, P., Manalis, S.: Electronic Detection of DNA by its Intrinsic Molecular Charge. PNAS **99**(22), 1412–1416 (2002). DOI 10.1073/pnas.232276699
54. Fthenakis, V., Kim, H., Alsema, E.: Emissions from Photovoltaic Life Cycles. Environmental Science & Technology **42**(6), 2168–2174 (2008). DOI 10.1021/es071763q
55. Fulkerson, W., Moore, J.P., Williams, R.K., Graves, R.S., McElroy, D.L.: Thermal Conductivity, Electrical Resistivity, and Seebeck Coefficient of Silicon from 100 to 1300° K. Physical Review **167**(3), 765–782 (1968). DOI 10.1103/PhysRev.167.765
56. Gao, Z., Agarwal, A., Trigg, A., Singh, N., Fang, C., Tung, C.H., Fan, Y., Buddharaju K.D., and Kong, J.: Silicon Nanowire Arrays for Label-Free Detection of DNA. Analytical Chemistry **79**(9), 3291–3297 (2007). DOI 10.1021/ac061808q

57. Geballe, T.H., Hull, G.W.: Seebeck Effect in Germanium. Physical Review **94**(5), 1134–1140 (1954). DOI 10.1103/PhysRev.94.1134
58. Geballe, T.H., Hull, G.W.: Seebeck Effect in Silicon. Physical Review **98**(4), 940–947 (1955). DOI 10.1103/PhysRev.98.940
59. Gharghi, M., Bai, H., Stevens, G., Sivoththaman, S.: Three-Dimensional Modeling and Simulation of $p-n$ Junction Spherical Silicon Solar Cells. IEEE Trans.Electron Devices **53**(6), 1355–1363 (2006). DOI 10.1109/TED.2006.873843
60. Giesbers, M., Kleijn, J., Stuart, M.: The Electrical Double Layer on Gold Probed by Electrokinetic andSurfaceForce Measurements. Journal of Colloid and Interface Science **248**(1), 88–95 (2002). DOI 10.1006/jcis.2001.8144
61. Gileadi, E., Kirowa Eisner, E., Penciner, J.: Interfacial Electrochemistry: An Experimental Approach. Addison-Wesley Publishing Company (1975)
62. Girard, A., Bendria, F., Sagazan, O.D., Harnois, M., Bihan, F.L., Salaün, A., Mohammed-Brahim, T., Brissot, P., Loréal, O.: Transferrin Electronic Detector for Iron Disease Diagnostics. In: IEEE Conf. on Sensors, pp. 474–477 (2006). DOI 10.1109/ICSENS.2007.355509
63. Goetzberger, A., Voß, B., Knobloch, J.: Sonnenenergie: Photovoltaik, vol. 2. Teubner Studienbücher (1997)
64. Goldsmid, H.: The Thermal Conductivity of Bismuth Telluride. Proc.Phys.Soc.B **69**(2), 203–209 (1956). stacks.iop.org/0370-1301/69/203
65. Goldsmid, H.: Heat Conduction in Bismuth Telluride. Proc.Phys.Soc. **72**(1), 17–26 (1958). stacks.iop.org/0370-1328/72/17
66. Goldsmid, H.: Recent Studies of Bismuth Telluride and Its Alloys. J.Appl.Phys. **32**(10), 2198–2202 (1961). DOI 10.1063/1.1777042
67. Grasser, T.: Non-Parabolic Macroscopic Transport Models for Semiconductor Device Simulation. Physica A: Statistical Mechanics and its Applications **349**(1-2), 221–258 (2005). DOI 10.1016/j.physa.2004.10.035
68. Grasser, T., Jungemann, C., Kosina, H., Meinerzhagen, B., Selberherr, S.: Advanced Transport Models for Sub-Micrometer Devices. In: Intl. Conf. on Simulation of Semiconductor Processes and Devices, pp. 1–8. Springer-Verlag (2004)
69. Grasser, T., Kosik, R., Jungemann, C., Kosina, H., Selberherr, S.: Nonparabolic Macroscopic Transport Models for Device Simulation Based on Bulk Monte Carlo Data. J.Appl.Phys. **97**(9), 093710 (2005). DOI 10.1063/1.1883311
70. Grasser, T., Kosik, R., Jungemann, C., Meinerzhagen, B., Kosina, H., Selberherr, S.: A Non-Parabolic Six Moments Model for the Simulation of Sub-100 nm Semiconductor Devices. J.Comp.Electronics **3**(3), 183–187 (2004). DOI 10.1007/s10825-004-7041-1
71. Grasser, T., Kosina, H., Gritsch, M., Selberherr, S.: Using Six Moments of Boltzmann's Transport Equation for Device Simulation. J.Appl.Phys. **90**(5), 2389–2396 (2001). DOI 10.1063/1.1389757
72. Grasser, T., Tang, T.W., Kosina, H., Selberherr, S.: A Review of Hydrodynamic and Energy-Transport Models for Semiconductor Device Simulation. Proc.IEEE **91**(2), 251–274 (2003). DOI 10.1109/JPROC.2002.808150
73. Green, M.: Solar Cells : Operating Principles, Technology, and System Applications. Prentice-Hall, Englewood Cliffs, NJ (1982)
74. Green, M.: Third Generation Photovoltaics: Solar Cells for 2020 and Beyond. Physica E: Low-Dimensional Systems and Nanostructures **14**(1-2), 65–70 (2002). DOI 10.1016/S1386-9477(02)00361-2
75. Green, M.: Consolidation of Thin-Film Photovoltaic Technology: The Coming Decade of Opportunity. Progress in Photovoltaics: Research and Applications **14**(5), 383–392 (2006). DOI 10.1002/pip.702
76. Gritsch, M., Kosina, H., Grasser, T., Selberherr, S.: Revision of the Standard Hydrodynamic Transport Model for SOI Simulation. IEEE Trans.Electron Devices **49**(10), 1814–1820 (2002). DOI 10.1109/TED.2002.803645
77. Grubmüller, H.: Force Probe Molecular Dynamics Simulations. Springer Protocols **305** (2005). DOI 10.1007/978-1-59259-912-7_23

78. Gupta, N., Alapatt, G., Podila, R., Singh, R., Poole, K.: Prospects of Nanostructure-Based Solar Cells for Manufacturing Future Generations of Photovoltaic Modules. Intl. Journal of Photoenergy p. 13 (2009). DOI 10.1155/2009/154059
79. Gupta, S., Elias, M., Wen, X., Shapiro, J., L.Brillson: Detection of Clinical Relevant Levels of Protein Analyte UnderPhysiologicBuffer Using Planar Field Effect Transistors. Biosensors and Bioelectronics **24**, 505–511 (2008). DOI 10.1016/j.bios.2008.05.011
80. Hahm, J., Lieber, C.: Direct Ultrasensitive Electrical Detection of DNA and DNA Sequence Variations Using Nanowire Nanosensors. Nano Letters **4**(1), 51–54 (2004)
81. Hall, R.: Electron-Hole Recombination in Germanium. Physical Review **87**(2), 387 (1952). DOI 10.1103/PhysRev.87.387
82. Hänsch, W.: Carrier Transport Near the Si/SiO_2 Interface of a MOSFET. Solid-State Electron. **32**, 839–849 (1989). DOI 10.1016/0038-1101(89)90060-9
83. Hänsch, W.: The Drift Diffusion Equation and its Application in MOSFET Modeling. XII. Springer-Verlag (1991)
84. Hänsch, W., Miura-Mattausch, M.: The Hot-Electron Problem in Small Semiconductor Devices. J.Appl.Phys. **60**(2), 650–656 (1986). DOI 10.1063/1.337408
85. Harame, D., Bousse, L., Shott, J., Meindl, J.: Ion-Sensing Devices with Silicon Nitride and Borosilicate Glass Insulators. IEEE Trans.Electron Devices **34**(8), 1700–1707 (1987)
86. Harnois, M., Sagazan, O., Girard, A., Salaün, A.C., Mohammed-Brahim, T.: Low Concentrated DNA Detection by SGFET. In: Transducers & Eurosensors, pp. 1983–1986. Lyon, France (2007)
87. Hasnat, K., Yeap, C.F., Jallepalli, S., Hareland, S., Shih, W.K., Agostinelli, V., Tasch, A., Maziar, C.: Thermionic Emission Model of Electron Gate Current in Submicron NMOSFETs. IEEE Trans.Electron Devices **44**(1), 129–138 (1997). DOI 10.1109/16.554802
88. Heitzinger, C., Kennell, R., Klimeck, G., Mauser, N., McLennan, M., Ringhofer, C.: Modeling and Simulation of Field-Effect Biosensors (BioFETs) and Their Deployment on the nanoHUB. J. Phys.: Conf. Ser. **107**, 012,004/1–12 (2008). DOI 10.1088/1742-6596/107/1/012004
89. Heitzinger, C., Klimeck, G.: Computational Aspects of the Three-Dimensional Feature-Scale Simulation of Silicon-Nanowire Field-Effect Sensors for DNA Detection. J.Comp.Electronics **6**(1-3), 387–390 (2007). DOI 10.1007/s10825-006-0139-x
90. van Herwaarden, A.: The Seebeck Effect in Silicon ICs. Sensors and Actuators **6**(4), 245–254 (1984). DOI 10.1016/0250-6874(84)85020-9
91. van Herwaarden, A., van Duyn, D., van Oudheusden, B., Sarro, P.: Integrated Thermopile Sensors. Sensors and Actuators A: Physical **22**(1-3), 621–630 (1989). DOI 10.1016/0924-4247(89)80046-9
92. van Herwaarden, A., Sarro, P.: Thermal Sensors Based on the Seebeck Effect. Sensors and Actuators **10**(3-4), 321–346 (1986). DOI 10.1016/0250-6874(86)80053-1
93. Hodgson, D.: Anisotropy of Thermoelectric Power in Bismuth Telluride. Tech. Rep. 377, Massachusetts Institute of Technology, Research Laboratory of Electronics (1961). hdl.handle.net/1721.1/4445
94. Holst, M., Saied, F.: Multigrid Solution of the Poisson-Boltzmann Equation. J. Comput. Chem. **14**, 105–113 (1993)
95. Holst, M., Saied, F.: Numerical Solution of the Nonlinear Poisson-Boltzmann Equation: Developing More Robust and Efficient Methods. J. Comput. Chem. **16**, 337–364 (1995)
96. Honsberg, C., Barnett, A.: UD-Led Team Sets Solar Cell Record, Joins DuPont on $100 Million Project. Press Release (2007). www.udel.edu/PR/UDaily/2008/jul/solar072307.html
97. Huang, C., Wang, T., Chen, C., Chang, M., Fu, J.: Modeling Hot-Electron Gate Current in Si MOSFET's Using a Coupled Drift-Diffusion and Monte Carlo Method. IEEE Trans.Electron Devices **39**(11), 2562–2568 (1992). DOI 10.1109/16.163464
98. Ieong, M.K.: A Multii-Valley Hydrodynamic Transport Model for *GaAs* Extracted from Self-Consistent Monte Carlo Data. M.S. Thesis, University of Massachusetts (1993)
99. Im, H., Huang, X.., Gu, B., Choi, Y..: A Dielectric-Modulated Field-Effect Transistor for Biosensing. Nature Nanotechnology **2**(7), 430–434 (2007)

100. Institute for Microelectronics, TU Wien, Gußhausstraße 2729, 1040 Wien, Austria/Europe: Minimos-NT Device and Circuit Simulator Release 2.1. www.iue.tuwien.ac.at/software/minimosnt
101. Ioffe, A.: Semiconductor Thermoelements and Thermoelectric Cooling. Infosearch London (1957). Originally published-U.S.S.R. Academy of Sciences, 1956.
102. Ioffe, A.: The Revival of Thermoelectricity. Scientific American (1958)
103. International Technology Roadmap for Semiconductors: 2009 Edition (2009). www.itrs.net/Links/2009ITRS/Home2009.htm
104. Iwata, H., Ohzone, T.: Numerical Solar Cell Simulation Including Multiple Diffused Reflection at the Rear Surface. Solar Energy Materials and Solar Cells **61**(4), 353 – 363 (2000). DOI 10.1016/S0927-0248(99)00119-1
105. Jacoboni, C., Lugli, P.: The Monte Carlo Method for Semiconductor Device Simulation. Springer-Verlag (1989)
106. Jacoboni, C., Reggiani, L.: The Monte Carlo Method for the Solution of Charge Transport in Semiconductors with Applications to Covalent Materials. Rev. Mod. Phys. **55**(3), 645–705 (1983). DOI 10.1103/RevModPhys.55.645
107. Jäger-Waldau, A.: Research, Solar cell Production and Market Implementation of Photovoltaics. Tech. rep., European Commission, DG Joint Research Centre, Institute for Energy, Renewable Energy Unit (2009). www.jrc.ec.europa.eu
108. Jaggi, R.: High-Field Drift Velocities in Silicon and Germanium. Helvetia Physica Acta **42**, 941–943 (1969)
109. Jaggi, R., Weibel, H.: High-Field Electron Drift Velocities and Current Densities in Silicon. Helvetia Physica Acta **42**, 631–632 (1969)
110. Jüngel, A.: Transport Equations for Semiconductors XVII, vol. 773. Springer-Verlag (2009)
111. Jungemann, C., Meinzerhagen, B.: Hierachical Device Simulation: The Monte Carlo Perspective. Springer-Verlag (2003)
112. Jungemann, C., Nguyen, C., Neinhüs, B., Decker, S., Meinerzhagen, B.: Improved Modified Local Density Approximation for Modeling of Size Quantization in NMOSFETs. In: Intl. Conf. on Modeling and Simulation of Microsystems, vol. 1, pp. 458–461 (2001)
113. Jungemann, C., Pham, A., Meinerzhagen, B., Ringhofer, C., Bollhöfer, M.: Stable Discretization of the Boltzmann Equation Based on Spherical Harmonics, Box Integration, and a Maximum Entropy Dissipation Principle. J.Appl.Phys. **100**(2), 024502 (2006). DOI 10.1063/1.2212207
114. Kabir, M., Ibrahim, Z., Sopian, K., Amin, N.: Effect of Structural Variations in Amorphous Silicon Based Single and Multi-Junction Solar Cells from Numerical Analysis. Solar Energy Materials and Solar Cells (2010). DOI 10.1016/j.solmat.2009.12.031
115. Kane, E.: Band Structure of Indium Antimonide. J.Phys.Chem.Solids **1**(4), 249–261 (1957). DOI 10.1016/0022-3697(57)90013-6
116. Karner, M., Gehring, A., Holzer, S., Pourfath, M., Wagner, M., Goes, W., Vasicek, M., Baumgartner, O., Kernstock, C., Schnass, K., Zeiler, G., Grasser, T., Kosina, H., Selberherr, S.: A Multi-Purpose Schrödinger-Poisson Solver for TCAD Applications. J.Comp.Electronics **6**(1), 179–182 (2007). DOI 10.1007/s10825-006-0077-7
117. Karner, M., Wagner, M., Grasser, T., Kosina, H.: A Physically Based Quantum Correction Model for DG MOSFETs. In: Materials Research Society Spring Meeting (MRS), pp. 104–105 (2006)
118. Khitun, A., Balandin, A., Liu, J., Wang, K.: In-Plane Lattice Thermal Conductivity of a Quantum-Dot Superlattice. J.Appl.Phys. **88**(2), 696–699 (2000). DOI 10.1063/1.373723
119. Khitun, A., Liu, J., Wang, K.: Thermal Conductivity of Si/Ge Quantum Dot Superlattices. In: Conf. on Nanotechnology, pp. 20–22 (2004). DOI 10.1109/NANO.2004.1392236
120. Kim, D., Gabor, A., Yelundur, V., Upadhyaya, A., Meemongkolkiat, V., Rohatgi, A.: String Ribbon Silicon Solar Cells with 17.8% Efficiency. In: 3rd World Conf. on Photovoltaic Energy Conversion. Georgia Institute of Technology (2003). hdl.handle.net/1853/26154
121. Kim, W., Singer, S., Majumdar, A., Zide, J., Gossard, A., Shakouri, A.: Role of Nanostructures in Reducing Thermal Conductivity Below Alloy Limit in Crystalline Solids. In: Intl. Conf. on Thermoelectrics, pp. 9–12 (2005). DOI 10.1109/ICT.2005.1519874

122. Kittel, C.: Einführung in die Festkörperphysik, vol. 14. Oldenburg Wissenschaftsverlag (2006)
123. Kluska, S., Granek, F., Rüdiger, M., Hermle, M., Glunz, S.: Modeling and Optimization Study of Industrial n-Type High-Efficiency Back-Contact Back-Junction Silicon Solar Cells. Solar Energy Materials and Solar Cells **94**(3), 568–577 (2010). DOI 10.1016/j.solmat.2009.11.025
124. Knaipp, M.: Modellierung von Temperatureinflüssen in Halbleiterbauelementen. Dissertation, Technische Universität Wien (1998). www.iue.tuwien.ac.at/phd/knaipp
125. Kosik, R., Grasser, T., Entner, R., Dragosits, K.: On The Highest Order Moment Closure Problem [Semiconductor Device Modelling Applications]. In: Electronics Technology: Meeting the Challenges of Electronics Technology Progress, 2004, vol. 1, pp. 118–121 (2004)
126. Kullmann, W., Geurts, J., Richter, W., Lehner, N., Rauh, H., Steigenberger, U., Eichhorn, G., Geick, R.: Effect of Hydrostatic and Uniaxial Pressure on Structural Properties and Raman Active Lattice Vibrations in Bi_2Te_3. Phys.Stat.Sol.(b) **125**(1), 131–138 (1984). DOI 10.1002/pssb.2221250114
127. Kuznetsov, V.L., Kuznetsova, L.A., Kaliazin, A.E., Rowe, D.M.: High Performance Functionally Graded and Segmented Bi_2Te_3-Based Materials for Thermoelectric Power Generation. Journal of Material Science **37**(14), 2893–2897 (2002). DOI 10.1023/A:1016092224833
128. Landheer, D., Aers, G., McKinnon, W., Deen, M., Ranuárez, J.: Model for the Field Effect from Layers of Biological Macromolecules on the Gates of Metal-Oxide-Semiconductor Transistors. J.Appl.Phys. **98**(4), 044,701–1 – 044,701–15 (2005)
129. Lang, C., Pucker, N.: Mathematische Methoden in der Physik, zweite erweiterte Auflage. Spektrum Akademischer Verlag (2005)
130. Lee, C.S., Tang, T.W., Navon, T.: Transport Models for MBTE. In: J. Miller (ed.) Numerical Analysis of Semiconductor Devices and Integrated Circuits, pp. 261–265. Dublin Ireland: Boole (1989)
131. Lee, S., von Allmen, P.: Tight-Binding Modeling of Thermoelectric Properties of Bismuth Telluride. Appl.Phys.Lett. **88**(2), 022107 (2006). DOI 10.1063/1.2162863
132. Lee, S.C., Tang, T.W.: Transport Coefficients for a Silicon Hydrodynamic Model Extracted from Inhomogeneous Monte-Carlo Calculations. Solid-State Electron. **35**(4), 561–569 (1992). DOI 10.1016/0038-1101(92)90121-R
133. Levermore, C.: Moment Closure Hierarchies for Kinetic Theories. Journal of Statistical Physics **83**(5), 1021–1065 (1996). DOI 10.1007/BF02179552
134. Liu, J.S.: Monte Carlo Strategies in Scientific Computing. Springer-Verlag, New York Berlin Heidelberg (2001)
135. Liu, W., nd G. Chen J.L. Liu, T.B.T., Wang, K.: Anisotropic Thermal Conductivity of Ge Quantum-Dot and Symmetrically Strained Si/Ge Superlattices. Journal of Nanoscience and Nanotechnology **1**, 39–42(4) (2001). DOI 10.1166/jnn.2001.013
136. Lombardi, C., Manzini, S., Saporito, A., Vanzi, M.: A Physically Based Mobility Model for Numerical Simulation of Nonplanar Devices. IEEE Trans.Computer-Aided Design of Integrated Circuits and Systems **7**(11), 1164–1171 (1988). DOI 10.1109/43.9186
137. Ludwig, W.: Festkörperphysik. Akademische Verlagsgesellschaft Wiesbaden (1978)
138. Lundstrom, M.: Fundamentals of Carrier Transport. Cambridge University Press (2000)
139. Malm, U., Edoff, M.: 2D Device Modelling and Finite Element Simulations for Thin-Film Solar Cells. Solar Energy Materials and Solar Cells **93**(6-7), 1066–1069 (2009). DOI 10.1016/j.solmat.2008.11.058
140. Markowich, P., Ringhofer, C., Schmeiser, C.: Semiconductor Equations. Springer-Verlag (1990)
141. Masetti, G., Severi, M., Solmi, S.: Modeling of Carrier Mobility Against Carrier Concentration in Arsenic-, Phosphorus-, and Boron-Doped Silicon. IEEE Trans.Electron Devices **30**, 764–769 (1983)
142. Maycock, P.: Thermal Conductivity of Silicon, Germanium, III-V Compounds and III-V Alloys. Solid-State Electron. **10**(3), 161–168 (1967). DOI 10.1016/0038-1101(67)90069-X
143. Meddins, H., Parrott, J.: The Thermal and Thermoelectric Properties of Sintered Germanium-Silicon Alloys. J.Phys.C:Solid State Phys. **9**(7), 1263–1276 (1976). stacks.iop.org/0022-3719/9/1263

144. Miele, A., Fletcher, R., Zaremba, E., Feng, Y., Foxon, C.T., Harris, J.J.: Phonon-Drag Thermopower and Weak Localization. Physical Review B **58**(19), 13,181–13,190 (1998). DOI 10.1103/PhysRevB.58.13181
145. Mingo, N.: Thermoelectric Figure of Merit and Maximum Power Factor in III–V Semiconductor Nanowires. Appl.Phys.Lett. **84**(14), 2652–2654 (2004). DOI 10.1063/1.1695629
146. Muscato, O., Romano, V.: Simulation of Submicron Silicon Diodes with a Non-Parabolic Hydrodynamical Model Based on the Maximum Entropy Principle. In: Intl. Workshop on Computational Electronics, pp. 94–95 (2000). DOI 10.1109/IWCE.2000.869941
147. Neinhüs, B.: Hierarchische Bauelementsimulationen von Si/SiGe Hochfrequenztransistoren. Dissertation, Universität Bremen (2002)
148. Nguyen, C., Jungemann, C., Meinerzhagen, B.: Modeling of Size Quantization in Strained Si-nMOSFETs with the Improved Modified Local Density Approximation. In: NSTI Nanotechnology Conference and Trade Show, vol. 3, pp. 33–36 (2005)
149. Nolas, G., Cohn, J., Slack, G., Schujman, S.: Semiconducting Ge Clathrates: Promising Candidates for Thermoelectric Applications. Appl.Phys.Lett. **73**(2), 178–180 (1998). DOI 10.1063/1.121747
150. Nolas, G., Sharp, J., Goldsmid, H.: Thermoelectrics: Basic Principles and New Materials Developments. Springer-Verlag (2001)
151. Nolting, W.: Grundkurs Theoretische Physik 6: Statistische Physik, vol. XII. Springer-Verlag (2007)
152. NREL Solar Cell Sets World Efficiency Record at 40.8 Percent. Press Release (2008). www.nrel.gov/news/press/2008/625.html
153. Golden, CO, USA: NREL Sets New CIGS Thin Film Efficiency Record. Press Release (2008). www.solarbuzz.com/news/NewsNATE50.htm
154. Ohl, R.: Light-Sensitive Electric Device (1946). www.freepatentsonline.com/2402662.html
155. Onsager, L.: Reciprocal Relations in Irreversible Processes. I. Physical Review **37**(4), 405–426 (1931). DOI 10.1103/PhysRev.37.405
156. Paasch, G., Übensee, H.: A Modified Local Density Approximation. Electron Density in Inversion Layers. Phys.Stat.Sol.(b) **113**(1), 165–178 (1982). DOI 10.1002/pssb.2221130116
157. Palankovski, V.: Simulation of Heterojunction Bipolar Transistors. Dissertation, Technische Universität Wien (2000). www.iue.tuwien.ac.at/phd/palankovski
158. Palankovski, V., Quay, R.: Analysis and Simulation of Heterostructure Devices. Springer-Verlag (2004)
159. Palestri, P., Mastrapasqua, M., Pacelli, A., King, C.: A Drift-Diffusion/Monte Carlo Simulation Methodology for $Si_{1-x}Ge_x$ HBT Design. IEEE Trans.Electron Devices **49**(7), 1242–1249 (2002). DOI 10.1109/TED.2002.1013282
160. Park, K., Lee, S., Sohn, Y., Choi, S.: BioFET Sensor for Detection of Albumin in Urine. Electronic Letters **44**(3) (2008)
161. Pejčinović, B., Tang, H., Egley, J., Logan, L., Srinivasan, G.: Two-Dimensional Tensor Temperature Extension of the Hydrodynamic Model and its Applications. IEEE Trans.Electron Devices **42**(12), 2147–2155 (1995). DOI 10.1109/16.477773
162. Peltier, J.: Nouvelles Experiences sur la Caloriecete des Courans Electrique. Ann. Chim. **LVI**, 371–387 (1834)
163. Pieters, B., Krc, J., Zeman, M.: Advanced Numerical Simulation Tool for Solar Cells - ASA5. In: Photovoltaic Energy Conversion, vol. 2, pp. 1513–1516 (2006). DOI 10.1109/WCPEC.2006.279758
164. Pirrung, M.: How to Make a DNA Chip. Angew. Chem. Intl. Ed. **41**, 1276–1289 (2002)
165. Poghossian, A., Cherstvy, A., Ingebrandt, S., Offenhäusser, A., Schöning, M.J.: Possibilities and Limitations of Label-Free Detection of DNA Hybridization with Field-Effect-Based Devices. Sensors and Actuators, B: Chemical **111-112**, 470–480 (2005)
166. Pollock, D.: CRC Handbook of Thermoelectrics, Chapter: Thermoelectric Phenomena. CRC Press LLC (1994)
167. protein data bank: www.pdb.org
168. PV FAQ's: What is the Energy Payback for PV? Press Release (2004). www.nrel.gov/docs/fy05osti/37322.pdf

169. Rahmat, K.: Simulation of Hot Carriers in Semiconductor Devices. Technical Report 591, Research Laboratory of Electronics, Massachusetts Institute of Technology (1995)
170. Rahmat, K., White, J., Antoniadis, D.: Computation of Drain and Substrate Currents in Ultra-Short-Channel nMOSFET's Using the Hydrodynamic Model. IEEE Trans.Computer-Aided Design of Integrated Circuits and Systems **12**(6), 817–824 (1993). DOI 10.1109/43.229756
171. Richou, F., Pelous, G., Lecrosnier, D.: Thermal Generation of Carriers in Gold-Doped Silicon. J.Appl.Phys. **51**(12), 6252–6257 (1980). DOI 10.1063/1.327611
172. Ringhofer, C., Heitzinger, C.: Multi-Scale Modeling and Simulation of Field-Effect Biosensors. ECS Transactions **14**(1), 11–19 (2008). DOI 10.1149/1.2956012
173. Roosbroeck, W.V.: Theory of Flow of Electrons and Holes in Germanium and Other Semiconductors. Bell Syst. Techn. J. **29**, 560–607 (1950)
174. Rowe, D.: Electrical Properties of Hot-Pressed Germanium-Silicon-Boron Alloys. J.Phys.D:Appl. Phys. **8**(9), 1092–1103 (1975). stacks.iop.org/0022-3727/8/1092
175. Rowe, D.: CRC Handbook of Thermoelectrics. CRC Press LLC (1994)
176. Sadaka, M., Thean, A., Barr, A., Tekleab, D., Kalpat, S., White, T., Nguyen, T., Mora, R., Beckage, P., Jawarani, D., Zollner, S., Kottke, M., Liu, R., Canonico, M., Xie, Q., Wang, X., Parsons, S., Eades, D., Zavala, M., Nguyen, B., Mazure, C., Mogab, J.: Fabrication and Operation of sub-50 nm Strained-Si on $Si_{1-x}Ge_x$ Insulator (SGOI) CMOSFETs. In: IEEE Intl. SOI Conf., pp. 209–211 (2004)
177. Sadovnikov, A., Roulston, D.: A Study of the Influence of Hydrodynamic Model Effects on Characteristics of Silicon Bipolar Transistors. COMPEL: The Intl. Journal for Computation and Mathematics in Electrical and Electronic Engineering **12**(4), 245–262 (1993). DOI 10.1108/eb051803
178. Scheidemantel, T.J., Ambrosch-Draxl, C., Thonhauser, T., Badding, J.V., Sofo, J.O.: Transport Coefficients from First-Principles Calculations. Physical Review B **68**(12), 125,210 (2003). DOI 10.1103/PhysRevB.68.125210
179. Schenk, A.: Re-Examination of Physical Models in the Temperature Range 300 K – 700 K. Tech. Rep. 99, German Bundesministerium für Bildung und Forschung (2001)
180. Scherrer, H., Scherrer, S.: CRC Handbook of Thermoelectrics, Chapter: Bismulth Telluride, Antimony Telluride, and Their Solid Solutions. CRC Press LLC (1994)
181. Schöning, M.J.: "Playing Around" with Field-Effect Sensors on the Basis of EIS Structures, LAPS and ISFETs. Sensors **5**(3), 126–138 (2005). DOI 10.3390/s5030126
182. Schuss, Z., Nadler, B., Eisenberg, R.: Derivation of Poisson and Nernst-Planck Equations in a Bath and Channel from a Molecular Model. Physical Review E **64**(3), 036,116 (2001). DOI 10.1103/PhysRevE.64.036116
183. Seebeck, T.J.: Über die magnetische Polarisation der Metalle und Erze durch Temperatur-Differenz. Annalen der Physik **82**(2), 133–160 (1826). DOI 10.1002/andp.18260820202
184. Selberherr, S.: Analysis and Simulation of Semiconductor Devices. Springer-Verlag (1984)
185. Selberherr, S., Hänsch, W., Seavey, M., Slotboom, J.: The Evolution of the MINIMOS Mobility Model. Solid-State Electron. **33**(11), 1425–1436 (1990). DOI 10.1016/0038-1101(90)90117-W
186. Shinwari, M., Deen, M., Landheer, D.: Study of the Electrolyte-Insulator-Semiconductor Field-Effect Transistor (EISFET) with Applications in Biosensor Design. Microelectronics Reliability **47**(12), 2025–2057 (2007). DOI 10.1016/j.microel.2006.10.003
187. Shockley, W.: Problems Related to p-n Junctions in Silicon. Solid-State Electron. **2**(1), 35–67 (1961). DOI 10.1016/0038-1101(61)90054-5
188. Shockley, W., Queisser, H.: Detailed Balance Limit of Efficiency of p-n Junction Solar Cells. J.Appl.Phys. **32**(3), 510–519 (1961). DOI 10.1063/1.1736034
189. Shockley, W., Read, W.T.: Statistics of the Recombinations of Holes and Electrons. Physical Review **87**(5), 835–842 (1952). DOI 10.1103/PhysRev.87.835
190. Singh, J.: Physics of Semiconductors and their Heterostructures. McGraw-Hill, Inc. (1993)
191. Singh, M., Bhandari, C.: Thermoelectric Properties of Bismuth Telluride Quantum Wires. Solid State Communications **127**(9-10), 649–654 (2003). DOI 10.1016/S0038-1098(03)00520-9

192. Singh, R., Chandran, P., Grujicic, M., Poole, K., Vingnani, U., Ganapathi, S., Swaminathan, A., Jagannathan, P., Iyer, H.: Dominance of Silicon CMOS Based Semiconductor Manufacturing Beyond International Technology Roadmap. Semiconductor Fabtech **30**, 104–113 (2006)
193. Singh, R., Gupta, N., Poole, K.: Global Green Energy Conversion Revolution in 21st Century Through Solid State Devices. In: Intl. Conf. on Microelectronics, pp. 45–54 (2008). DOI 10.1109/ICMEL.2008.4559221
194. Siwy, Z., Apel, P., Baur, D., Dobrev, D., Korchev, Y., Neumann, R., Spohr, R., Trautmann, C., Voss, K.O.: Preparation of Synthetic Nanopores with Transport Properties Analogous to Biological Channels. Surface Science **532-535**, 1061–1066 (2003). DOI 10.1016/S0039-6028(03)00448-5
195. Siwy, Z., Apel, P., Dobrev, D., Neumann, R., Spohr, R., Trautmann, C., Voss, K.: Ion Transport Through Asymmetric Nanopores Prepared by Ion Track Etching. Nucl. Instrum. and Meth. in Phys. Res. Sect. B: Beam Interactions with Materials and Atoms **208**, 143–148 (2003). DOI 10.1016/S0168-583X(03)00884-X. Ionizing Radiation and Polymers
196. Siwy, Z., Dobrev, D., Neumann, R., Trautmann, C., Voss, K.: Electro-Responsive Asymmetric Nanopores in Polyimide with Stable Ion-Current Signal. Appl.Phys.A **76**(5), 781–785 (2003). DOI 10.1007/s00339-002-1982-7
197. Siwy, Z., Gu, Y., Spohr, H.A., Baur, D., Wolf-Reber, A., Spohr, R., Apel, P., Korchev, Y.E.: Rectification and Voltage Gating of Ion Currents in a Nanofabricated Pore. EPL (Europhysics Letters) **60**(3), 349–355 (2002)
198. Siwy, Z., Fuliński, A.: Fabrication of a Synthetic Nanopore Ion Pump. Physical Review Letters **89**(19), 198,103 (2002). DOI 10.1103/PhysRevLett.89.198103
199. Skrabek, E., D.Trimmer: CRC Handbook of Thermoelectrics, Chapter: Properties of the General TAGS System. CRC Press LLC (1994)
200. Slack, G., Hussain, M.: The Maximum Possible Conversion Efficiency of Silicon-Germanium Thermoelectric Generators. J.Appl.Phys. **70**(5), 2694–2718 (1991). DOI 10.1063/1.349385
201. Song, J., Li, S., Huang, C., Anderson, T., Crisalle, O.: Modeling and Simulation of a $CuGaSe_2/Cu(In_{1-x},Ga_x)Se_2$ Tandem Solar Cell. In: Photovoltaic Energy Conversion, vol. 1, pp. 555–558 (2003). DOI 10.1109/WCPEC.2003.1305344
202. Span, G.: Thermoelectric Element (2008). Austrian Patent AT 410 492 B. Intl. Patent Application PCT/AT01/00123, Granted in USA, Russia, Europe
203. Stern, E., Klemic, J., Routenberg, D., Wyrembak, P., Turner Evans, D., Hamilton, A., LaVan, D., Fahmy, T., Reed, M.: Lable-free Immunodetection with CMOS-compatible Semiconducting Nanowires. Nature Letters **445**(1), 519–522 (2007). DOI 10.1038/nature05498
204. Stettler, M., Alam, M., Lundstrom, M.: A Critical Examination of the Assumptions Underlying Macroscopic Transport Equations for Silicon Devices. IEEE Trans.Electron Devices **40**(4), 733–740 (1993). DOI 10.1109/16.202785
205. Stoletow, A.: Suite des recherches actino-electriques. Comptes Rendus **CVII**, 91 (1888)
206. Stoletow, A.: Sur une sorte de courants electriques provoques par les rayons ultraviolets. Comptes Rendus **CVI** (1888)
207. Stoletow, A.: Sur les courants actino-électriques dans l'air raréfié. Journal de Physique **9**, 468 (1890)
208. Stratton, R.: Diffusion of Hot and Cold Electrons in Semiconductor Barriers. Physical Review **126**(6), 2002–2014 (1962). DOI 10.1103/PhysRev.126.2002
209. Stratton, R.: Semiconductor Current-Flow Equations (Diffusion and Degeneracy). IEEE Trans.Electron Devices **19**(12), 1288–1292 (1972)
210. Stryer, L.: Biochemistry 4th Edition. New York: W.H. Freeman and Company (1995)
211. Sugihara, S., Tomita, S., Asakawa, K., Suda, H.: High Performance Properties of Sintered Bi_2Te_3-Based Thermoelectric Material. In: Intl. Conf. on Thermoelectrics, pp. 46–51 (1996). DOI 10.1109/ICT.1996.553254
212. Tang, T., Gan, H.: Two Formulations of Semiconductor Transport Equations Based on Spherical Harmonic Expansion of the Boltzmann Transport Equation. IEEE Trans.Electron Devices **47**(9), 1726–1732 (2000). DOI 10.1109/16.861583

213. Tang, T., Ramaswamy, S., Nam, J.: An Improved Hydrodynamic Transport Model for Silicon. IEEE Trans.Electron Devices **40**(8), 1469–1477 (1993). DOI 10.1109/16.223707
214. Tang, T.W., Ieong, M.K.: Discretization of Flux Densities in Device Simulations Using Optimum Artificial Diffusivity. IEEE Trans.Computer-Aided Design of Integrated Circuits and Systems **14**(11), 1309–1315 (1995)
215. Tasaki, H., Kim, W.Y., Hallerdt, M., Konagai, M., Takahashi, K.: Computer Simulation Model of the Effects of Interface States on High-Performance Amorphous Silicon Solar Cells. J.Appl.Phys. **63**(2), 550–560 (1988). DOI 10.1063/1.340085
216. Thoma, R., Emunds, A., Meinerzhagen, B., Peifer, H.J., Engl, W.: Hydrodynamic Equations for Semiconductors with Nonparabolic Band Structure. IEEE Trans.Electron Devices **38**(6), 1343–1353 (1991). DOI 10.1109/16.81625
217. Thomson, W.: On a Mechanical Theory of Thermoelectric Currents. Proc. of the Royal Society of Edinburgh pp. 91–98 (1851)
218. Tsutagawa, M., Michael, S.: Triple Junction $InGaP/GaAS/Ge$ Solar Cell Optimization: The Design Parameters for a 36.2% Efficient Space Cell Using Silvaco ATLAS Modeling & Simulation. In: Photovoltaic Specialists Conf., pp. 001,954–001,957 (2009). DOI 10.1109/PVSC.2009.5411544
219. University of New South Wales: Highest Silicon Solar Cell Efficiency Ever Reached. Press Release (2008). www.sciencedaily.com/releases/2008/10/081023100536.htm
220. Vasicek, M.: Advanced Macroscopic Transport Models. Dissertation, Technische Universität Wien (2009). www.iue.tuwien.ac.at/phd/vasicek
221. Ventura, D., Gnudi, A., Baccarani, G.: A Deterministic Approach to the Solution of the BTE in Semiconductors. La Rivista del Nuovo Cimento (1978-1999) **18**(6), 1–33 (1995). DOI 10.1007/BF02743029
222. Villanueva, J., Diaz, V., Bolivar, S., Tejada, T., Rodriguez, E.: A Multijunction Solar Cell Simulation Program for the Development of Concentration Systems. IEEE Trans.Electron Devices pp. 262–265 (2007). DOI 10.1109/SCED.2007.384042
223. Vining, C.: A Model for the High-Temperature Transport Properties of Heavily Doped n-type Silicon-Germanium Alloys. J.Appl.Phys. **69**(1), 331–341 (1991). DOI 10.1063/1.347717
224. Wagner, M.: Simulation of Thermoelectric Devices. Dissertation, Technische Universität Wien (2007). www.iue.tuwien.ac.at/phd/wagner
225. Wagner, M., Karner, M., Cervenka, J., Vasicek, M., Kosina, H., Holzer, S., Grasser, T.: Quantum Correction for DG MOSFETs. J.Comp.Electronics **5**(4), 397–400 (2006). DOI 10.1007/s10825-006-0032-7
226. Weinberg, I.: Phonon-Drag Thermopower in Cu-Al and Cu-Si Alloys. Physical Review **139**(3A), A838–A843 (1965). DOI 10.1103/PhysRev.139.A838
227. Willner, I., Katz, E.: Bioelectronics: From Theory to Applications, 1 ed. Wiley-VCH (2005). www.worldcat.org/isbn/3527306900
228. Windbacher, T., Sverdlov, V., Selberherr, S.: Modeling of Low Concentrated Buffer DNA Detection with Suspend Gate Field-Effect Transistors (SGFET). In: Intl. Workshop on Computational Electronics, pp. 169–172 (2009)
229. Windbacher, T., Sverdlov, V., Selberherr, S., Heitzinger, C., Mausern, N., Ringhofer, C.: Study of the Properties of Biotin-Streptavidin Sensitive BioFETs. In: Intl. Conf. on Biomedical Electronics and Devices, pp. 24–30 (2009)
230. Wolff, P.: Theory of Electron Multiplication in Silicon and Germanium. Physical Review **95**(6), 1415–1420 (1954). DOI 10.1103/PhysRev.95.1415
231. Wood, C.: Materials for Thermoelectric Energy Conversion. Reports on Progress in Physics **51**(4), 459–539 (1988). stacks.iop.org/0034-4885/51/459
232. Wu, D.L., Fan, R., Yang, P., Majumdar, A.: Thermal Conductivity of $Si/SiGe$ Superlattice Nanowires. Appl.Phys.Lett. **83**(15), 3186–3188 (2003). DOI 10.1063/1.1619221
233. Wu, M.W., Horing, N.J.M., Cui, H.L.: Phonon-Drag Effects on Thermoelectric Power. Physical Review B **54**(8), 5438–5443 (1996). DOI 10.1103/PhysRevB.54.5438
234. Xu, J., Luo, X., Chen, H.: Analytical Aspects of FET-Based Biosensors. Frontiers in Bioscience **10**, 420–430 (2005)

235. Yang, R., Chen, G.: Thermal Conductivity Modeling of Periodic Two-Dimensional Nanocomposites. Physical Review B **69**(19), 195,316 (2004). DOI 10.1103/PhysRevB.69.195316
236. Yang, R., Chen, G.: Nanostructured Thermoelectric Materials: From Superlattices to Nanocomposites. Materials Integration **18**, 1–12 (2006)
237. Yates, D., Levine, S., Healy, T.: Site-Binding Model of the Electrical Double Layer at the Oxide/Water Interface. Journal of the Chemical Society **70**, 1807–1818 (1974). DOI 10.1039/F19747001807
238. Zheng, G., Patolsky, F., Cui, Y., Wang, W.U., Lieber, C.M.: Multiplexed Electrical Detection of Cancer Markers with Nanowire Sensor Arrays. Nature Biotechnology **23**(10), 1294–1301 (2005)
239. Zhitinskaya, M., Nemov, S., Svechnikova, T., Luk'yanova, L., Konstantinov, P., Kutasov, V.: Thermal Conductivity of $Bi_2Te_3 : Sn$ and the Effect of Codoping by Pb and I Atoms. Physics of the Solid State **45**(7), 1251–1253 (2003). DOI 10.1134/1.1594237
240. Zhou, J.: Thermal and Thermoelectric Transport Measurements of One-Dimensional Nanostructures. Ph.D. thesis, University of Texas at Austin (2005)
241. Zhou, J., Zhang, L., Leng, Y., Tsao, H.K., Sheng, Y.J., Jiang, S.: Unbinding of the Streptavidin-Biotin Complex by Atomic Force Microscopy: A Hybrid Simulation Study. J.Chem.Phys. **125**(10), 104905 (2006). DOI 10.1063/1.2337629